

C. Mier

CHARACTERIZATION OF A NEW METHOD FOR PARTIAL DISCHARGE MEASUREMENTS IN HVDC GIS

Characterization of a new method for partial discharges measurements in HVDC GIS

By

Christian Mier Escurra

in partial fulfilment of the requirements for the degree of

Master of Science

in Electrical Sustainable Energy

at the Delft University of Technology,
to be defended publicly on Friday July 6, 2018 at 10:00 AM.

Supervisor:	Dr. Armando Rodrigo Mor TU Delft
Thesis committee:	Prof. Ir. Peter Vaessen TU Delft
	Dr. Ir. Milos Cvetkovic TU Delft
	Dr. Armando Rodrigo Mor TU Delft

An electronic version of this thesis will be available at <http://repository.tudelft.nl/> after one years, meanwhile the thesis is under embargo for journal paper purposes.

Contents

Abstract	5
Acknowledgements.....	5
Glossary	6
1. Introduction.....	7
1.1. Background	7
1.2. Problem statement	9
1.3. Research goals.....	10
1.4. Thesis structure	10
2. Partial Discharge Phenomena	12
2.1. Breakdown mechanism	12
2.2. Types of discharges.....	12
2.3. Appearance of partial discharges.....	13
2.4. IEC 60270 Detection.....	15
2.5. Electro-Magnetic Waves propagation	16
2.6. Pulse Analysis	16
2.7. Chapter conclusions	18
3. Sensor Characteristic	19
3.1. Accuracy.....	19
3.2. Resolution	27
3.3. HFCT calibration.....	28
3.4. Reflected primary impedance	29
3.5. Chapter conclusions	30
4. GIS characteristic	31
4.1. Characteristic impedance and phase velocity	31
4.2. Chapter conclusions	36
5. Sensor and GIS interaction.....	37
5.1. Sensor and GIS electric circuit model.....	37
5.2. Current distribution	43
5.3. Interference signal	45
5.4. Calibration in the GIS.....	46
5.5. Discharge location	48
5.6. Chapter conclusions	50
6. Antenna measurement	51
6.1. Attenuation	51
6.2. Chapter conclusions	53
7. PD Measurements in GIS	55
7.1. PD measurement setup.....	55
7.2. Corona PD.....	57
7.3. Moving particle discharge	63

7.4. Internal Discharges.....	65
7.5. Chapter Conclusion	68
8. Results and Conclusions	69
9. Appendix	70
9.1. TUDelft GIS sketch.....	70
9.2. Devices Index.....	71
9.3. List of Figures.....	72
9.4. List of tables	73
Bibliography.....	75

Abstract

Detection of partial discharge (PD) in any high voltage equipment is of great importance to improve the reliability of the device and the power system. Characteristics of PDs, such as: rate of occurrence, magnitude, location and the type; gives information of the assets that must be considered. Nowadays, there are many different methods for sensing PDs in GIS (Gas Insulated Substation), however none of them can give fully information of the PD. The most important sensor is the antenna, with great advantages over other sensors, but still, with the limitation of not giving the magnitude of the discharge. The Delft University of Technology has patented a new method for measuring PDs in HVDC GIS. It is believed that this new method has great advantages over the current method, namely charge determination and improved sensibility.

The aim of this work is to find the measuring characteristics of this new method for sensing PDs in a GIS. These characteristics include resolution, attenuation and sensitivity. The most important feature of this new sensing method is the capacity of measuring the PDs magnitude. Therefore, a calibration method for charge calculation is provided. Finally, the new method and the antenna are compared with real measured PDs in a GIS.

To analyse the calibration of the new method; electrical characteristics of the sensor and GIS were simulated and compared with measurements. The results demonstrate that a PD can be calculated using the calibration method with low error values. This error value will depend in the measuring situation. The thesis also demonstrates some measuring advantages of this new method over the antenna.

Acknowledgements

First, I would like to thank my sponsors CONACyT and SENER, for trusting in my capacities and granting me with a full scholarship. Thanks for giving me the opportunity to develop my professional career in the prestigious Delft University of Technology.

Thanks to my thesis supervisor Dr. Armando Rodrigo, for his positive attitude and guidance throughout the research. I would like to include in the acknowledgements to Dr. Luis Carlos Castro for his help during the experiments. Also, I give my gratitude to the High Voltage Lab staff for its time dedication and advice for the experiments.

Finally, but not less important, special thanks to my family for their advice and encourage along my life. For shaping my life to become who I am now.

Glossary

AC	Alternating Current	TS	Triggering Sensor
AIS	Air Insulated System	UHFS	Ultra-High Frequency Sensor
BD	Band Width		
CT	Current Transformer		
DC	Direct Current		
EI	Electric Interference		
EM	Electromagnetic		
EMI	Electromagnetic Interference		
FED	Floating Electrode Discharge		
FEM	Finite Element Method		
GIS	Gas Insulated Substation		
HFCT	High Frequency Current Transformer		
HV	High Voltage		
HVDC	High Voltage Direct Current		
MI	Magnetic Interference		
MPD	Moving Particle Discharge		
PD	Partial Discharge		
PG	Pulse Generator		
PRPD	Phase-Resolved Partial Discharge		
SA	Surge Arrester		
SF ₆	Sulfur Hexafluoride		
SNR	Signal to Noise Ratio		
SU	Synchronization Unit		
TDoA	Time Difference of Arrival		
TE	Transverse Electric		
TEM	Transverse Electric and Magnetic		
TM	Transverse Magnetic		

1. Introduction

1.1. Background

1.1.1. Gas insulated substation

The two main applications of a gas insulated systems are for gas insulated substation (GIS) and gas insulated lines. Electric substations are nodes in the electric network and are used for the protection of the distribution of the electricity. The transmission line is a long-distance transportation path for the electric power. The purpose of using a GIS over an air insulated system (AIS) are reduced environmental and industrial conditions, reduced space and increased safety.

The GIS is a compacted substation, where the electric power equipment is enclosure in a high pressurized gas insulated coaxial structure. The coaxial structure has the inner conductor which carries the power current under high voltage (HV) and the enclosure which is grounded. The two different potential conductors are insulated by pressurized sulfur hexafluoride (SF_6) gas, giving approximately 2.3 times a higher breakdown voltage than air [1].

GIS are designed for HV applications ranging from 72.5 to 800 kV [2]. Typical GIS substations includes equipment such as: circuit breakers (CB), switches, bushings, buses, instrumentation and the gas-insulating system. To support the HV conductor and separate it from the grounded enclosure, a solid insulator is placed along the pipe, this insulator is called spacer. Figure 1 shows some of the equipment included in a GIS substation.

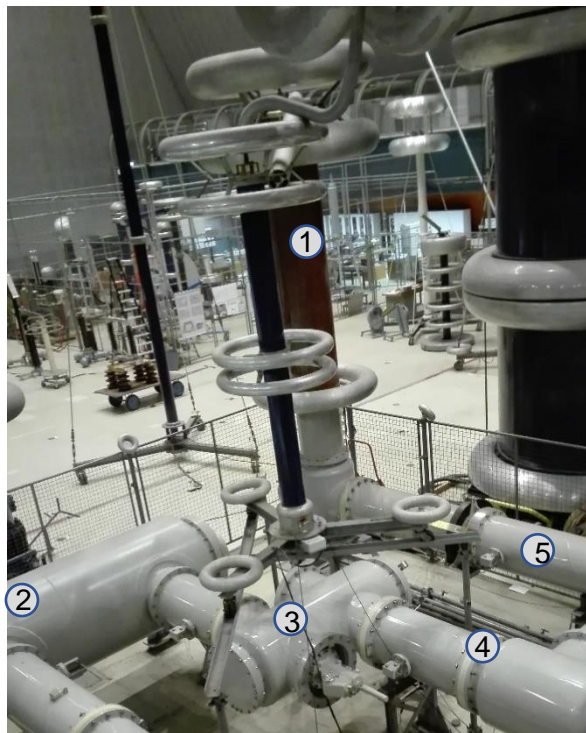


Figure 1. TUDelft GIS; 1: bushing, 2:CB, 3: switch, 4:spacer, 5:enclosure

The first GIS was introduced in 1960s, since then, their reliability has been improved. Some of the advantages using the GIS are the close location to the load center, with considerable savings in sub-transmission systems. GIS offers longer reliability, typically with 20 years or more of operation before the system is replaced [2]. The main advantage of the GIS over an air insulated system is the reduced space required due to its compact structure. The lack of sufficient land infrastructure for conventional substations has increase the demand of GIS technology. It is estimated that GIS will increase significantly in the coming years, with sales of almost 400M USD in 2017 to sales up to 1,400M USD in 2028 for Latin America, for instance [3].

A promising use of GIS substations is for offshore wind farm generation. The space needed compared to an AIS is of great advantage; one of the greatest cost challenges to developing an offshore substation is the size of the structure. Another problem of an offshore substation is the expensive maintenance, a way to reduce the maintenance is by means of a GIS substation. Now a days GIS have been used for AC short distances transmission (<80 km) in offshore substations. For long transmission distances high voltage direct current (HVDC) offers a better cost-effective option. The project Progress on Meshed HVDC Offshore Transmission Networks (PROMOTION) under the EU Horizon 2020, has the goal of deployment of a meshed off-shore HVDC grid [4]. To fulfill the objective, the use of an online monitoring of the offshore DC GIS is required, this includes a method for measuring partial discharges in the GIS insulation.



Figure 2. TenneT / HelWin alpha Offshore HVDC substation (picture taken from [4]).

1.1.2. PD detection in GIS

It is well known that condition monitoring is important to improve the reliability of any HV equipment and to save maintenance cost. Analysis of failures in GIS, shows that 60% of failures comes from an insulation failure. The most important indicators of insulation failure are the occurrence of partial discharges (PD) and partial over-thermal [5]. The rate of occurrence, discharge magnitude, discharge location and the type of discharge, gives information of the degradation of the insulation and the measures that must be taken.

When a PD occur, different physical phenomena take place, such as electromagnetic energy, emission of light, gas decomposition and pressure waves. All these phenomena can be used to detect the PD using different sensors. The most important measuring methods are: acoustic, chemical and electrical detection. Each of them have their own advantages and drawbacks. For instance, the acoustic detection is interfered by vibration noise. Chemical detection doesn't give information about the location of the PD. There are several ways to detect the PDs, but there is no method capable of giving all the information about the PD. A summary of the characteristic of each detection method is shown in Table 1 [6].

	Chemical	Acoustic	Electrical (antenna)
PD classification	Yes	Yes	Yes
Rate of occurrence	No	Yes	Yes
PD location	No	Yes	Yes
Attenuation	-	High	Low
Resolution	Low	Low	High
Intrusively installation	No	No	Yes
PD magnitude	No	No	No
Price	Low	Low	High

Table 1. Characteristic of each PD detection method.

1.2. Problem statement

The most common PD detection method with greater advantages is the electric detection, this method uses antennas as the sensing of the PDs, which are ultra-high frequency sensors (UHFS). These sensors have many advantages over the other methods, such as: high sensitivity and strong anti-interference. Nevertheless, the UHFS, as the name implies, it only works with very high frequency (300 to 3000 MHz) [6]; requiring larger band width (BD) signal conditioning devices with higher sampling data requirement. High frequencies give difficulties on the calibration and attenuation of the signal. The information of the magnitude of a PD is contained in the low frequencies, therefore, is no possible to acquire the PD magnitude by means of a UHFS. A great fraction of the existing GIS in the world doesn't have UHFS, and the installation of antennas requires the de-energization and dismantling of the substation.

The department of DC Systems, Energy Conversion & Storage of the Delft University of Technology (TUDelft) has patented a new method of sensing the PD signals in the GIS. The sensor consists of a high frequency current transformer (HFCT), which detects the current produced by the PD. The construction of a GIS is composed of pipe sections joined together with flanges. The flanges are also used to fix the spacer, so the junction is a sandwich of a flange, spacer and another flange joined with bolts (Figure 3). When a PD occurs, the current flows from the inner conductor to the outer conductor and travels all along the enclosure. When the traveling wave encounters a spacer, the current flows through the bolts, where the current transformer is installed (Figure 4). For new GIS models, the spacer is fixed inside the enclosure, so there is no access to it, in that case the HFCT is installed in a different way. In this thesis the old configuration of the spacer is used, although the same methodologies can be used for the new spacer configuration.



Figure 3. Spacer and flanges joined with bolts.

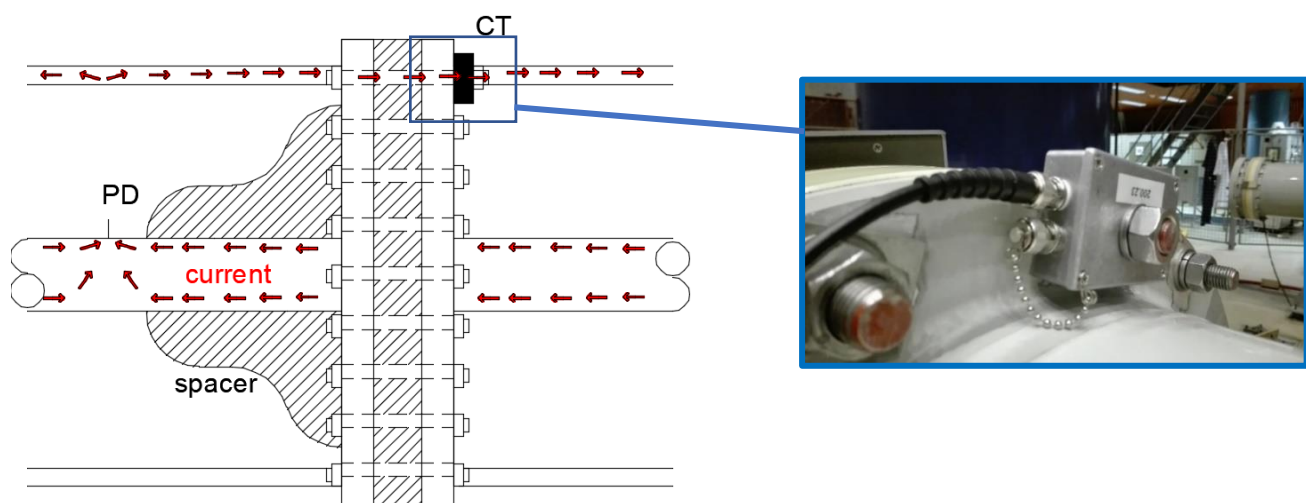


Figure 4. Photo of an installed HFCT in the GIS

Unlike the UHFS, which measures the radiation produced by the PD, the HFCT measures the current resulted from it. It is believed that the HFCT could have advantages over the antenna, such as:

- Less attenuation of the signal
- Higher sensitivity
- Higher resolution
- Lower sampling rate required
- PD magnitude measurement

1.3. Research goals

The use of a HFCT in online monitoring in GIS has not been used before, therefore, some questions must be answered to understand the behavior of PD measuring method. One of the greatest advantage of the HFCT over the UHFS, is the capacity of calculating the PD magnitude.

- How much current can be read by the sensor before it get saturated?
- What is the frequency dependency behavior of the HFCT?
- What is the accuracy of the sensor?
- How does the PD current propagates in the GIS?
- How does the HFCT interacts with the GIS?
- What is the accuracy of the sensor when is interacting with the GIS?
- What is the attenuation of the HFCT compared with UHFS (antennas)?
- What is the resolution and sensitivity of the HFCT compared with the UHFS when measuring real PDs in the GIS?

To approximate the charge with a sufficient level of accuracy, a calibration method is investigated and presented in this thesis. Different types of PDs in the GIS are measured to calculate the charge magnitude using the calibration method and to give the resolution of the sensor for different discharges. At the end of the thesis, a comparison between the new detection method and the antennas is made, giving the advantages and disadvantages of each sensor.

1.4. Thesis structure

The thesis is divided in seven chapters, covering the following topics in each chapter:

Chapter 2: Partial discharge phenomena. In this chapter the breakdown mechanism in gases, different types of discharges in GIS and the appearance of PD's is covered. Also, a brief introduction of electromagnetic waves and pulse analysis is discussed.

Chapter 3: Sensor characteristic: This section talks about the magnetic and frequency characteristic of the HFCT. Its transfer function is modeled and measured. The error and limitation of the sensor is discussed in the chapter.

Chapter 4: GIS characteristic. In this chapter the characteristic impedance and phase velocity for different sections in the GIS are investigated.

Chapter 5: HFCT and GIS interaction. The results from previous two chapters are used to determine the current distribution in the GIS due to the integration of the HFCT to the GIS. Also, the calibration and localization of a discharge are discussed.

Chapter 6: Antenna measurement. In this chapter a brief explanation of the actual method for measuring PDs is explained. At the end of the chapter, an attenuation comparison between the UHFS and the HFCT is shown.

Chapter 7: PD measurements in GIS. In the last chapter, different defects are generated in the GIS. These defects are measured and compared between the HFCT and UHFS.

Along the thesis, the set-ups for each experiment are explained. Detailed information of the used devices is included in the Appendix section 2. The diagram of the GIS used for the experiments is attached in Appendix section 1.

2. Partial Discharge Phenomena

The physics behind the phenomena that is being measured have to be understood before presenting the measuring methodology. This chapter explains the basic theory behind the PD propagation in GIS. First, the different breakdown mechanism in pressurized gas are presented. Then, the most common types of discharges in GIS are explained and the PD's appearance, using the IEC 60270 and the time resolved description. A brief explanation of the electromagnetic wave propagation due to PDs in the GIS is covered and finally the frequency analysis of a pulse.

2.1. Breakdown mechanism

The GIS, as the name implies, is insulated with pressurized gas. The most used gas is SF₆ due to its high electronegativity, giving excellent insulating properties. In some cases, the SF₆ is mixed with N₂, giving different characteristics. Three breakdown mechanisms exist in SF₆ [7].

- **Townsend Mechanism:** The gas is ionized by the collision between gas molecules and the free electrons emitted by the high electric field. If the collision form enough free electrons, an avalanche is formed and finally a breakdown. The formation of new free electrons is known as a feed-back process. For the feedback to occur, new electrons have to be released when the ions hit the cathode.
- **Streamer Mechanism:** For higher gas pressures or larger electrode-gaps (more common in GIS conditions), the streamer mechanism applies. The avalanche growth of free electrons creates a stream between electrodes creating a conducting path and finally a discharge.

2.2. Types of discharges

A PD is a breakdown of the insulator which do not completely bridge the distance between the electrodes [8]. The PDs are classified depending on the defect in which are generated. A description of the most common discharges in GIS are presented below.

- 1) **Internal discharges:** occur in a gas-filled cavity in a solid dielectric. The difference in permittivity between the solid and gas dielectric, creates a field enhancement in the dielectric with lower permittivity (usually the gas). When the electric field is high enough to create a breakdown, the accumulated electrons in the cavity are emitted and a breakdown occurs. The process is repeated until the electric field produced by the voltage source (sinusoidal 50/60 Hz or DC source) is equal to the electric field of the accumulated electrons in the cavity. In the case of the GIS, the internal discharge can occur when there are cavities in the solid insulation, e.g. bubbles introduced in the spacer or bushing in the production process.
- 2) **Surface discharge:** occurs along dielectric interfaces, where a considerable tangential field strength is present. The interface in the GIS case is gas-solid bounded. The field is enhanced if particles exist in the surface of the spacer. Surface discharge may occur if metal particles are left on the spacer.
- 3) **Corona discharge:** occurs in sharp points in one of the electrodes. The sharp point can occur in either high-voltage or ground electrode. Due to the electric field enhancement due to the charge accumulation in a sharp edge, a partial breakdown occurs. The inception of negative corona under alternate current (AC) and direct current (DC) voltage occur at a similar voltage level. The starting electron is originated by field emission from the cathode, this happens for any gas. In SF₆, the positive corona has a different behavior; the starting electron is generally originated away from the sharp point, by photo-ionization mechanism [9]. The corona defect can appear in the GIS when either the enclosure or inner conductor are scratched during the installation and a protution in the aluminium is created.

- 4) **Floating electrode discharge (FED):** An electrically floating electrode induces a voltage which depends on the capacitance with the ground and with the HV electrode. If the voltage induced in the floating electrode reaches the insulation strength of the dielectric, a discharge will occur. An example is when a field grading shield loses its contact with the HV conductor.
- 5) **Moving particle discharge (MPD):** In resting position, a free moving particle is in contact with the grounded electrode (enclosure). With the energization of the GIS it acquires an induced charge, which creates an interaction with the external electric field and exerts a Coulomb force on it. This particle is subjected to Coulomb force drag and gravity force, accelerating the particle in direction of the resultant force. The particle accelerates towards the electrode discharging itself and returning back to the grounded electrode. Sometimes during installation, some conductive particles can be left inside the GIS, such as metallic shavings.

Figure 5 shows the most common defects presented in a GIS.

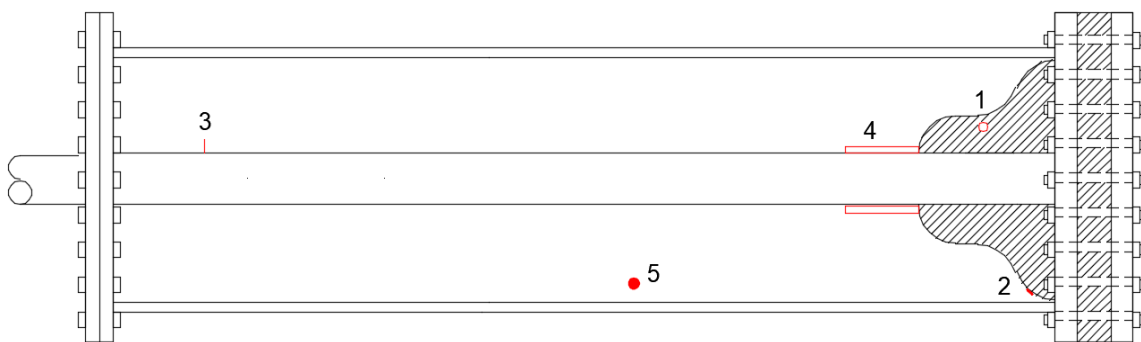


Figure 5. Defects in a GIS; 1) cavity, 2) surface particle, 3) protrusion in the HV electrode, 4) floating electrode.

2.3. Appearance of partial discharges

The appearance of PDs can be described in two ways:

2.3.1. Classical description

Here, the PDs are seen as an infinitely short phenomenon with no time scale. The current impulses are superimposed with the power frequency (50/60 Hz) voltage. Figure 6 shows the patterns in a phase-resolved partial discharge (PRPD) plot for different defects, the pictures are taken from [8] and [9].

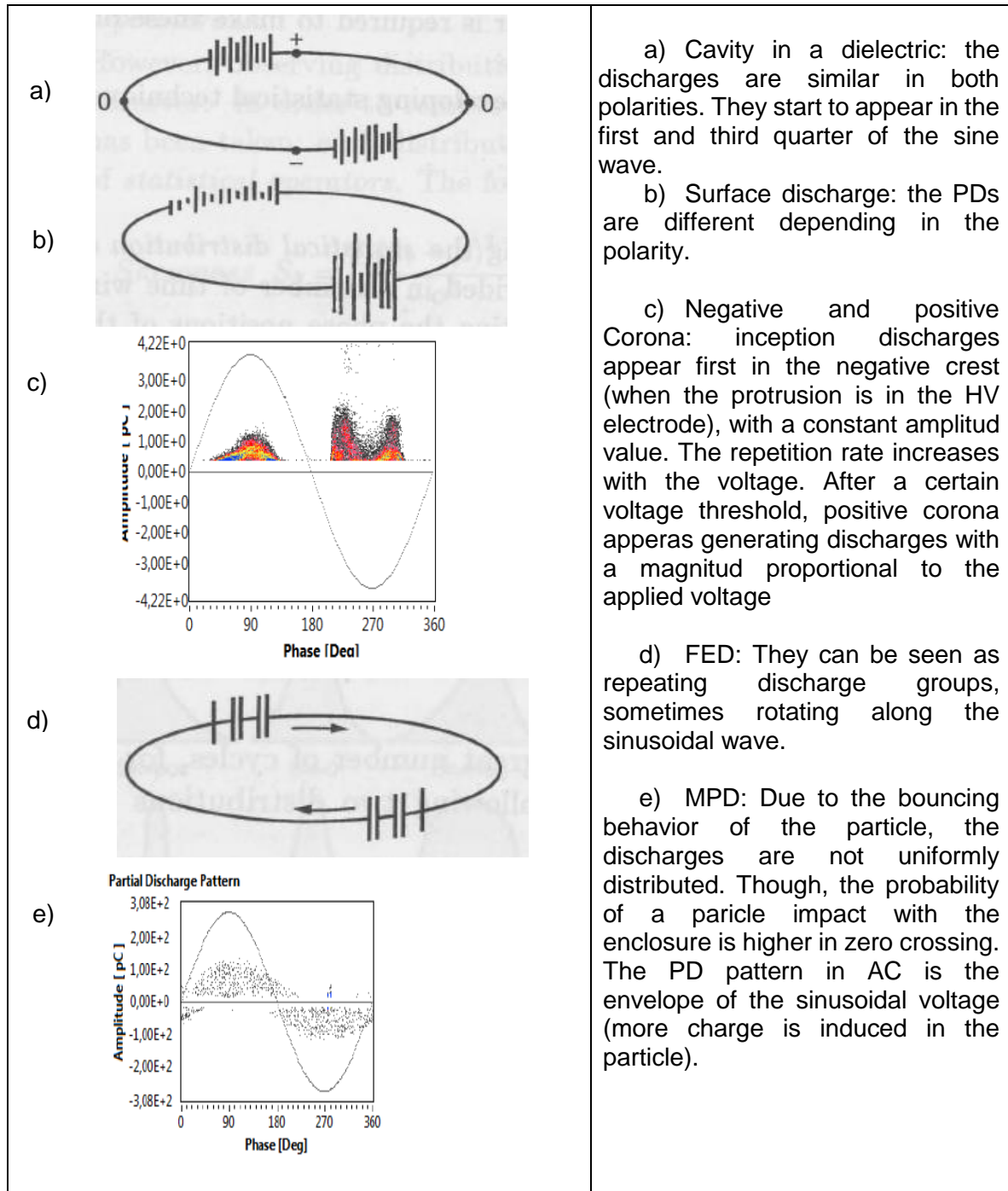


Figure 6. PRPD for different type of defects: a) internal discharge, b) surface discharge, c) corona discharge, d) FED, e) MPD

2.3.2. Time-resolved description

Here the PDs are described as a current or voltage pulse in the real time scale. The pulse shape depends in the physical phenomena and the electric circuit parameters. The shape of the measured pulse is dependent of the BW used. Wide-band detections and travelling wave location are based in this description.

For internal discharges the wave shape will depend in the condition of the cavity. In a virgin cavity where no discharges happen before, no cathode is available, so a Townsend mechanism cannot be formed. Instead a streamer starts the discharges. Unlike the Townsend, the streamer only requires electrons, which are faster to move than ions, therefore, the pulse have a very short duration (1-10 ns) [8]. When the cavity is aged, chemical reactions occur in the cavity and cathode is formed, so now Townsend breakdown takes place. These discharges take more time, giving a pulse duration in the range of 80-800 ns.

In surface charges, when inception voltage happens, the pulse looks similar with internal discharges, by increasing the voltage above the inception one, the magnitude of the pulse increases as well.

In a negative corona, which appears before the positive corona; the rise-time of the pulse is determined by the drift velocity of electrons and is approximately 1 ns. When the electrons are trapped in the air near the anode, a space charge is formed, and the discharge stops, the slow ions drift back and causes the current wave, which decays in a slower range than the rise. The pulse duration will depend in the sharpness of the protrusion. Figure 7 shows the pulse duration for different radii of the protrusion. (Figure taken from [8]). Positive corona corresponds to a Townsend mechanism, with a larger front and longer plateau.

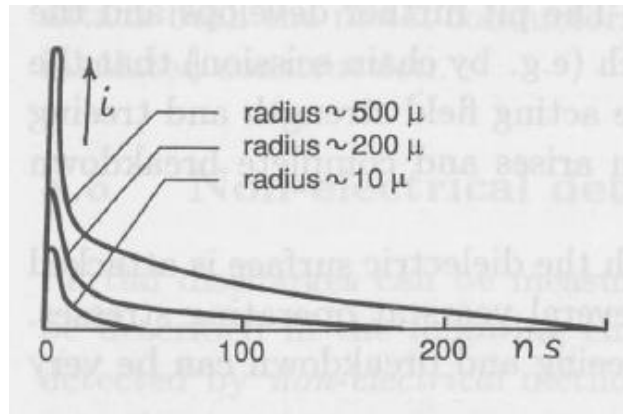


Figure 7. Current wave for a corona discharge with different radii of the protrusion point

2.4. IEC 60270 Detection

The most used measurement of discharge PDs is called the IEC 60270 detection, which measures an apparent charge. Figure 8 shows a diagram of a basic circuit of the IEC 60270 detection.

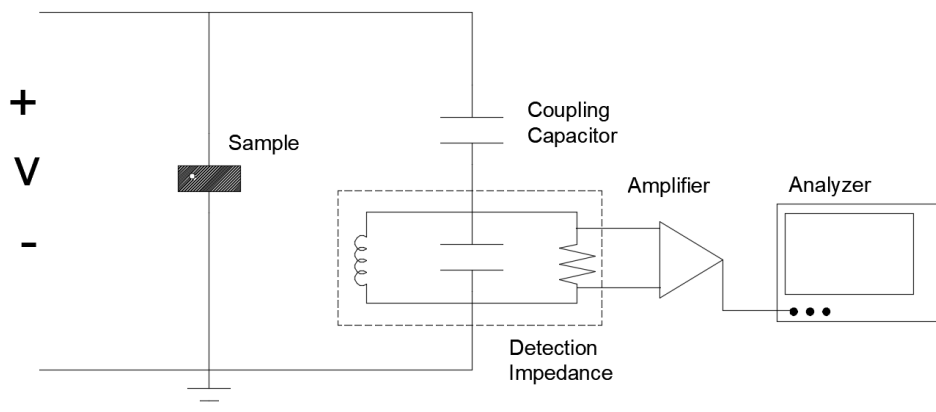


Figure 8. Diagram of an IEC 60270 detection

A high voltage is applied at the terminals of the sample. In parallel with the sample is the coupling capacitor and detection impedance in series. When a discharge is produced at the sample, the pulse will see a high impedance path in the HV source and a low impedance through the coupling capacitor. The coupling capacitor has a lower magnitude than the detection impedance, so most of the voltage is maintained in the coupling capacitor and no HV appears in the measuring section. At the measuring impedance, voltage pulses are formed and then amplified to display them on the PD analyzer. The value of the discharge can be calculated by knowing the value of the output voltage, and the rest of the electric components (sample capacitance, coupling capacitor, detection R, L and C and amplifier). The amplifier used normally has a bandwidth (BW) in the range of 100 to 400kHz, with this BW the pulses length appears in the order of 2 to 10 μs. For a GIS application this detection method is not adequate, because of the great amount of reflection in the GIS, the measured pulse would be the superposition of all the reflections [8].

2.5. Electro-Magnetic Waves propagation

A PD is the movement of a charge in a dielectric medium, the acceleration of this charge will induce electromagnetic (EM) waves according to Maxwell's equations:

$$\nabla \times \hat{E} = -j\omega\mu\hat{H} \quad 1$$

$$\nabla \times \hat{H} = j\omega\mu\hat{E} \quad 2$$

Solution for Maxwell's equations for a wave propagation in z direction, are classified whether both or one EM components are zero in the same direction.

- Transverse Electric and Magnetic (TEM): $E_z = H_z = 0$
- Transverse Electric (TE): $E_z = 0$ and $H_z \neq 0$
- Transverse Magnetic (TM): $H_z = 0$ and $E_z \neq 0$

Maxwell's equations have three orthogonal solutions: two curl-based solutions (TE and TM) and one gradient-based solution, which is linked to the charges (TEM).

When a PD occur, these three modes will propagate in the GIS, the TEM mode is propagated as current in the inner conductor and the enclosure. The TE and TM propagates as radiation at high frequencies. The antenna is coupled capacitively in the enclosure of the GIS, so it measures the induced electric field in the three modes. The Electric field must be at high frequencies to be induced in the antenna, that is why the antenna works as a high pass filter. On the other hand, the HFCT is installed in one of the bolts of the GIS, so it only measures the current that flows in the enclosure. Therefore, HFCT measures the low frequency spectra of the signal, it acts as a band pass filter (Figure 11 and Figure 12). Figure 9 shows an illustrative explanation.

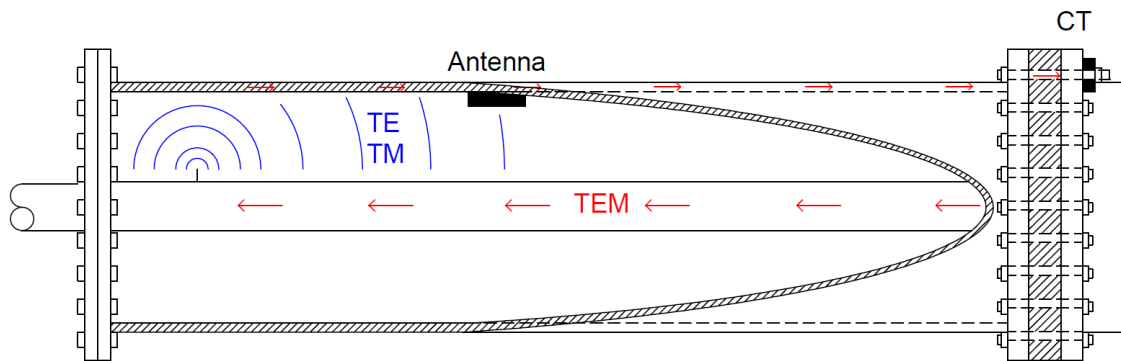


Figure 9. Representation of the EM wave propagation in the GIS with different sensing systems

2.6. Pulse Analysis

According to Fourier Transform, any signal in the time domain can be represented by the sum of sinusoidal waves at different frequencies and a DC (offset) component.

$$F(\omega) = \int_{-\infty}^{\infty} f(t)e^{-j\omega t} dt \quad 3$$

Where:

ω : frequency in radians

$f(t)$: any function in time

In the zero frequency or DC component, equation 3 becomes:

$$F(0) = \frac{1}{T} \int_0^T f(t) dt \quad 4$$

Where
T: is the period of the signal

The minimum frequency component (besides the DC component) that is possible to calculate is the inverse of the period, or the size of the measured window. For example, for a window of 1 μ s, the minimum frequency in the spectrum will be of 1 MHz and the following frequencies will be multiples of this frequency. The maximum measurable frequency depends in the Nyquist criteria, this is the half of the sample frequency.

By definition, current is the amount of charge moving in a certain period. Then, the current produced by a PD is:

$$i(t) = \frac{dq}{dt} [A] \quad 5$$

By knowing the waveform of the current, the charge can be calculated just by integrating the current over the period:

$$q = \int_0^T i(t) dt [C] \quad 6$$

Equation 4 is the same as equation 6. By using Fourier transform of a current wave, the DC component will be the charge.

A pulse is characterized to have short duration with a big steepness. The duration of the pulse depends on discharge mechanism and the electric circuit of the system. A pulse duration is limited by a Dirac delta function. The Dirac delta function is a pulse with a duration approaching to zero, and with a magnitude approaching to ∞ . The Fourier transformation of a Dirac function is plane in all frequencies from $\pm\infty$ (Figure 10).

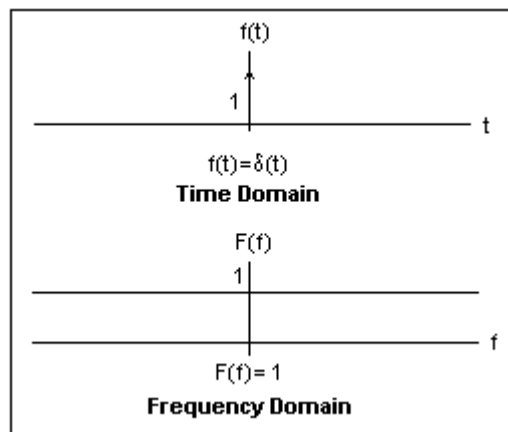


Figure 10. Time and frequency domain of a Dirac delta function, image taken from [10]

When the pulse duration increases, the higher frequencies magnitudes are reduced. In the following figures, the frequency spectrum for two pulses with different duration are shown. The first one has a duration of 10 ns, the cut off frequency for this pulse is 60 MHz (Figure 11). For the second pulse, the duration is 100ns, so the cut-off frequency is reduced to 6 MHz (Figure 12).

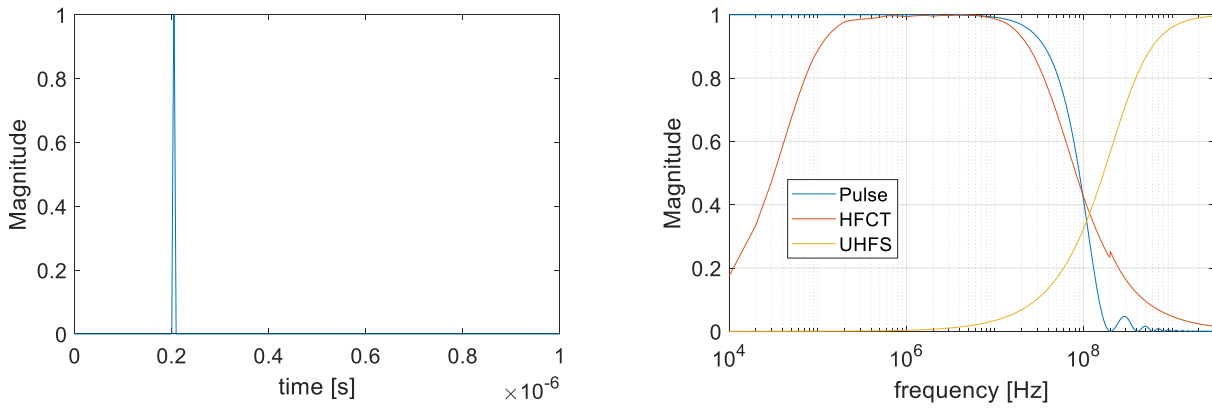


Figure 11. 10ns pulse duration in time and frequency domain

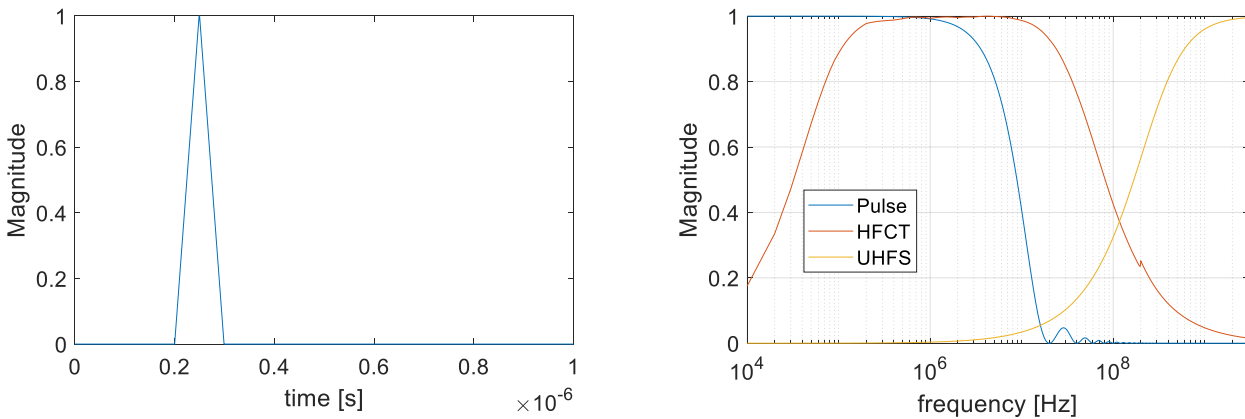


Figure 12. 100ns pulse duration in time domain

The low frequencies are flat and then there is a decay. Therefore, low frequencies approximate to the DC value. The pulse of Figure 11 approximates to the duration of a real PD in SF₆. For high frequencies, the signal has almost disappeared, however, the information of the charge is contained in the low frequencies. In the right side of Figure 11 and Figure 12, the pulse bandwidth is compared with the HFCT and UHFS BW. The HFCT shares part of the low frequency flat zone with the pulse. On the other hand, the cut-off frequency of the antenna starts in a frequency where the pulse is already decayed. It is obvious the great advantage of the HFCT, which works for lower frequencies than the UHFS.

2.7. Chapter conclusions

When a PD occur, it produces an EM wave that travels in the GIS. The EM wave is represented as a current/voltage pulse, the shape of this pulse will depend in the electric circuit parameters, and in the physical mechanism. The breakdown mechanisms depend in the type of defect where the PD was created. In a GIS the most important defects are the internal discharge, surface discharge, corona, MPD and FED. The spectrum of a pulse is a flat region in the low frequencies and then a decay for higher frequencies. The charge is the DC component of a current pulse. Therefore, by measuring the lower frequency, it is possible to find an approximation of the charge magnitude. The charge magnitude is very relevant for monitoring: it is an indicator of the severity of the insulation defect, by knowing the magnitude of the PD is possible to compare measurements between laboratory test and on-site test. The antenna has the disadvantage that it can only measure very high frequency (in the order of GHz), thus, the information of the charge is lost with a UHFS measurement. It is important to know the BW of the sensor to compared with the BW of the signal. The BW, gain, equivalent impedance and other important parameters of the sensor are presented in the next chapter.

3. Sensor Characteristic

The main characteristic of a sensor is its transfer function, this is the relation between the input and output signal of the sensor. This and other important features of the sensor are presented in the chapter. The sensitivity and resolution of the HFCT is covered. The sensitivity is analyzed for different input magnitudes and frequencies. A brief introduction to the resolution is presented, a more complete information of resolution is covered in chapter 7. At the end of the chapter, the sensor is calibrated with an experiment, using the calculated transfer function.

3.1. Accuracy

Accuracy refers to the degree in which a measurement approaches to the real value. An important parameter of accuracy is the sensitivity which represents the relation of the input signal with the output signal. In our case, the accuracy of the measuring system depends on the sensor and the GIS as is described in chapter 5. In this chapter, only the sensor characteristic is covered.

The physical assembly of the HFCT is a toroid in which the primary conductor goes through the center of the toroid, and the secondary is a coil wound around the toroid (Figure 13). The electric representation of the primary and secondary circuit of the CT is the magnetic fields (self-inductance) L , electric field (parasitic capacitances) C , and the load in the secondary R . The primary and secondary conductors are magnetically coupled, this means that the current flowing through the primary will induce a voltage in the secondary and vice versa (Figure 14).



Figure 13. Picture of the HFCT

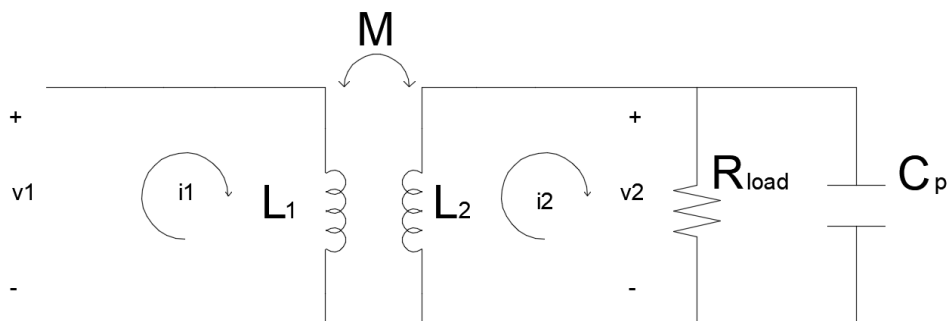


Figure 14. Electric circuit of the HFCT

The equations that govern the electric behavior of the HFCT are 7 and 8:

$$V1(t) = \frac{di_1(t)}{dt} L_1 - \frac{di_2(t)}{dt} M \quad 7$$

$$\frac{di_1(t)}{dt} M = \frac{di_2(t)}{dt} L_2 + V2(t) \quad 8$$

Where:

V1: represents the input voltage.

V2: output voltage.

L1 and L2: primary and secondary self-inductance respectively.

M: mutual inductance.

The core used in the experiments is a ferrite N30 obtained from EPCOS data book 2013. The relative permeability (μ_e) is a variable which depends in the temperature of the core, magnetic field through the core and the frequency of the magnetic field.

To obtain the temperature dependent permeability of the core, it is necessary to calculate the heat transfer from the HFCT to the environment. Although, it is possible to do an approximation, it is believed that the RMS current of the discharges are so low that the core will not increase its temperature, therefore, the permeability is used at 20 °C (Figure 15).

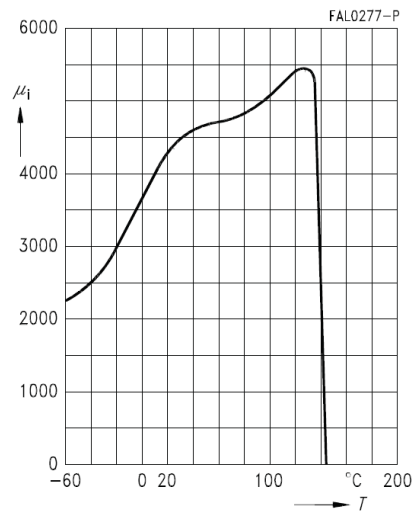


Figure 15. N30 permeability temperature dependent

3.1.2. Magnetic field dependency

The saturation of the core due to high magnetic fields depends on the magnetic field magnitude. This magnetic field is produced by the current through the primary. When the magnetic field increases above the linear region, the core gets saturated. This means that the magnetic flux barely increases when the current is increased. Thereby, the permeability of the core changes in the saturation zone. Figure 16 shows the magnetic flux density (B) vs magnetic field (H) of the N30 core at 20 °C and 10 kHz.

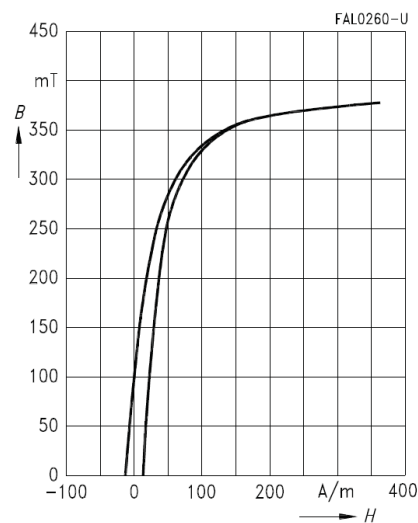


Figure 16. N30 permeability Magnetic field dependent

As it's seen in Figure 16, the saturation starts at 35 A/m. To calculate in the most critical situation and to simplify calculations, it is assumed that almost all the flux goes through the core which makes an almost perfect coupling between the primary coil and the secondary coil current. Therefore, Ampere's law is used in the core (9).

$$\oint H \cdot d\ell = \iint J \cdot ds \quad 9$$

The H field in the core results from the difference between the current from the primary and the secondary circuit.

$$H_{resultant} = \frac{i_1 - i_2 N}{2\pi R} [A/m] \quad 10$$

Where:

R: inner ratio of the core.

N: number of turns of secondary

Because of the non-linearity of the electric circuit, the equations cannot be solved in Laplace domain. Therefore, the system is solved in the time domain using equations 11 and 12.

$$v_1(t) = \frac{di_1(t)}{dt} L_1(t) - \frac{di_2}{dt} M(t) \quad 11$$

$$\frac{di_1}{dt} M(t) = \frac{di_2}{dt} L_2(t) + i_2(t) R \quad 12$$

The function of the inductor is shown in equation 13.

$$L(t) = \frac{NB(t)wD}{i(t)} [H] \quad 13$$

Where:

w: width of the core [m].

D: depth of the core [m].

The initial conditions for the differential equation are known: the current is zero, and the inductance value is known in the linear region.

The relation BH in the magnetic core is the plot in Figure 16, therefore, the permeability is function of the magnetic field.

$$H_c = B/\mu(H) [A/m] \quad 14$$

Due to the complexity of the non-linear equation the differential equation is solved in a numerical way discretizing the variables and replacing $\frac{df(t)}{dt}$ with $\frac{\Delta f(t)}{\Delta t} = \frac{f(t) - f(t-1)}{\Delta t}$. The values $i_1(t)$ and $i_2(t)$ are found for every time step. The differential equation is iterated increasing the peak current, until the H fields reaches a saturation value.

For an AC power system, there is a possibility that current flows in the enclosure; an unbalanced power frequency current, and induced current in the enclosure due to the current in the HV conductor. The induced current in the enclosure circulates in the thickness of it, so the total magnetic field induced in the HFCT is zero. A FEM simulation of the induced current density in the enclosure is shown in Figure 17. The current density in blue is the incoming current and the red is the going current, the magnitude of both currents is the same with opposite way. However, in a real situation the enclosure is not uniform, it has valves antennas etc., and a different income and going current may be different where the HFCT is placed, further investigation

has to be done in the matter. A high current in the primary, may saturate the HFCT; and the gain of the sensor is going to decrease.

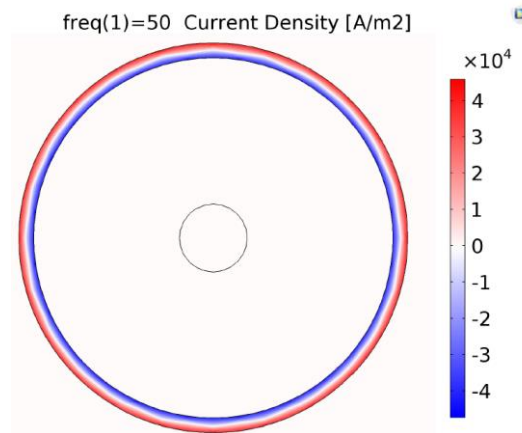


Figure 17. Induced current density in the enclosure due to the power frequency current.

With a 50 Hz current of 3 A., the Magnetic field reached 32 A/m and the output signal is distorted, having some harmonics (Figure 18). The results are obtained for a 5 turns HFCT.

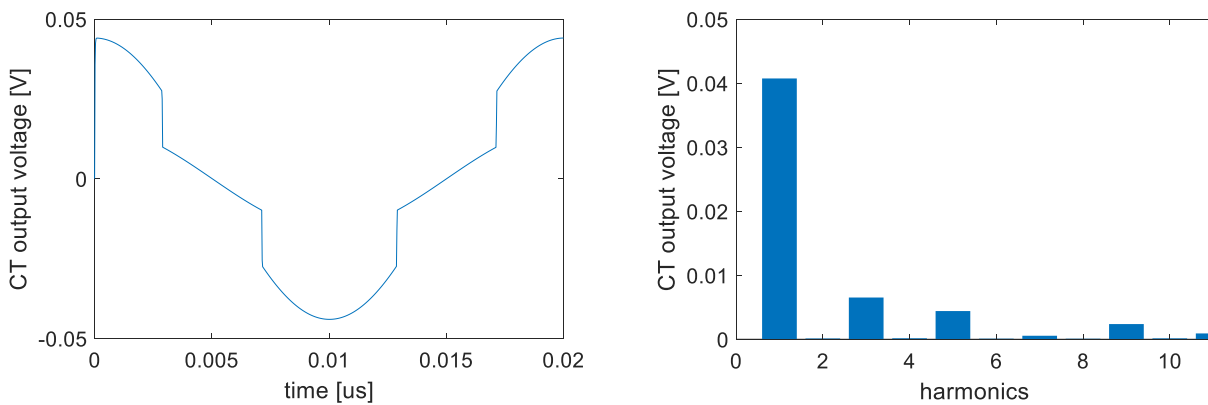


Figure 18. Voltage output (a. time domain b. frequency domain) of the HFCT for a 50 Hz 3 Amps input.

For a PD pulse, the frequency spectrum is very large, so the higher frequencies currents are induced in the secondary and the H field of the core is decreased.

The faster the pulse, the higher the contribution of the high frequencies and thus, more induced current in the secondary and finally, lower resultant H field in the core.

The results of different saturation currents for different pulses and CT's number of turns are presented in Table 2. The saturation of the core depends in the magnitude of the current and the duration of the pulse, so the area under the pulse wave (charge) is calculated.

	10 ns pulse	100 ns pulse	50 Hz
3 turns CT	955 Apeak @ 4.77 μ C	99 Apeak @ 4.9 μ C	3 Apeak
5 turns CT	2.64 kApeak @ 13.2 μ C	266 Apeak @ 13.3 μ C	
10 turns CT	10.5 kApeak @ 52.3 μ C	1.05 kApeak @ 52.5 μ C	

Table 2. Saturation current and Charge for different pulses

The highest magnitude PDs that may occur in the GIS are the FED with a few nano Coulombs [7], so there no real discharge capable of saturate the core. In conclusion the characteristic of the HFCT presented in this work is valid for the PD measured in a GIS.

3.1.3. Frequency dependency

Another variation of the permeability in the core is due to the frequency of the signal. A partial discharge has frequencies ranging from DC up to 20 GHz. A permeability vs frequency characteristic of the N30 core is provided in the paper [11].

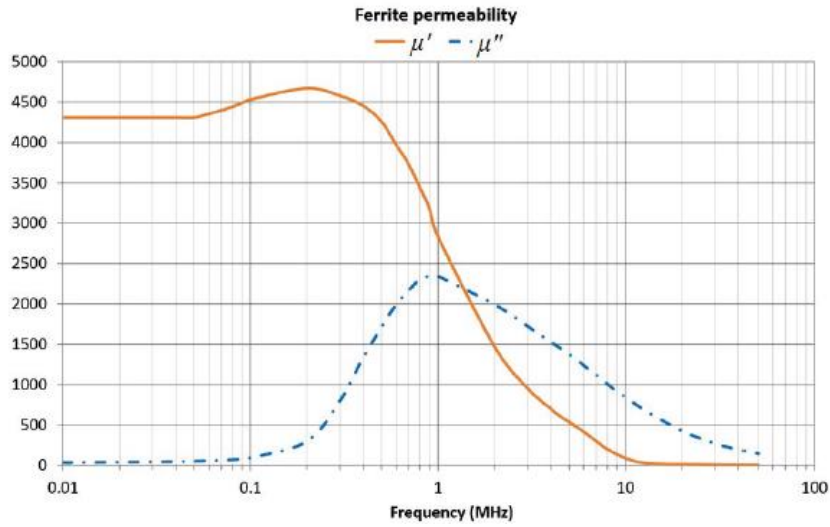


Figure 19. N30 permeability frequency dependent

The permeability has two components: $\mu_e = \mu' - j\mu''$. The real permeability represents the induction of magnetic flux density in the core, while the imaginary permeability represent the losses in the core due to hysteresis and eddy currents. Therefore, the core losses are included in the inductance.

Manipulating equation 7 and 8, using Laplace transform, the transfer function of the sensor is:

$$G(\omega) = \frac{V_2}{i_1} = Z_{eq} \frac{j\omega M(\omega)}{j\omega L_2(\omega) + Z_{eq}} [V/A] \quad 15$$

Where:

Z_{eq} represents the equivalent impedance of the parallel sum of the load and the parasitic capacitance of the HFCT (and/or surge arrester, see chapter 7). Any other load added to the secondary of the HFCT is included in this impedance.

$$Z_{eq} = \frac{-jX_c R}{R - jX_c} [\Omega] \quad 16$$

Where:

R: is the load in the secondary of the HFCT in Ω 's.

X_c : is the parasitic capacitance and capacitive load in the secondary of the HFCT Ω 's.

For an ideal toroid configuration, the secondary and the primary self-inductance are related using equation 17.

$$L_2 = L_1 N^2 [H] \quad 17$$

The mutual inductance is related with the primary and secondary self-inductances and a coupling factor "k" which represents the proportion of magnetic field which cross both windings.

$$M = k\sqrt{L_1 L_2} [H] \quad 18$$

To calculate the k factor, the HFCT was simulated using a finite element method (FEM) software. L1, L2 and M were calculated using different frequencies, and using equation 18, k is obtained. L1 is obtained using equation 19.

$$L_1 = \frac{\varphi}{i_1} [H] \tag{19}$$

Where

φ : is the total magnetic flux in all the domain due to i_1 , in Webers.
The secondary winding was simulated as an open circuit.

To find M, the open circuit voltage is calculated in the software and equation 20 is used

$$M = \frac{V_{oc}}{i_1 \omega} [H] \tag{20}$$

The catalog of the magnetic core gives the inductance at low frequency: $AL= 5.46 \times 10^{-6}$ H. To calculate the inductance for higher frequencies, [12] proposes the following formula:

$$L = AL * (\mu' - j\mu'')/\mu_i [H] \tag{21}$$

Where:

μ_i : is the initial permeability of the core (at low frequencies).

The gain of a HFCT of 3 and 5 turns was measured to compare it with the theoretical one. The frequency spectrum was measured from 10 kHz to 4 GHz. For frequencies from 300 kHz to 4 GHz a spectrum analyzer (Device 1) was used; connecting as input the primary circuit of the HFCT, and as output the secondary. The lower frequencies were measured using a different setup. A function generator (Device 2), was connected in series with the HFCT and then the 50 Ω resistance of the oscilloscope (Device 3). The secondary of the HFCT was connected to another 50 Ω channel of the oscilloscope. By generating sinusoidal waves at different frequencies and comparing the measured voltages in the secondary and the current in the primary, the gain was obtained.

Figure 20 shows the comparison between calculated and measured gain for 5 and 3 turns HFCT.

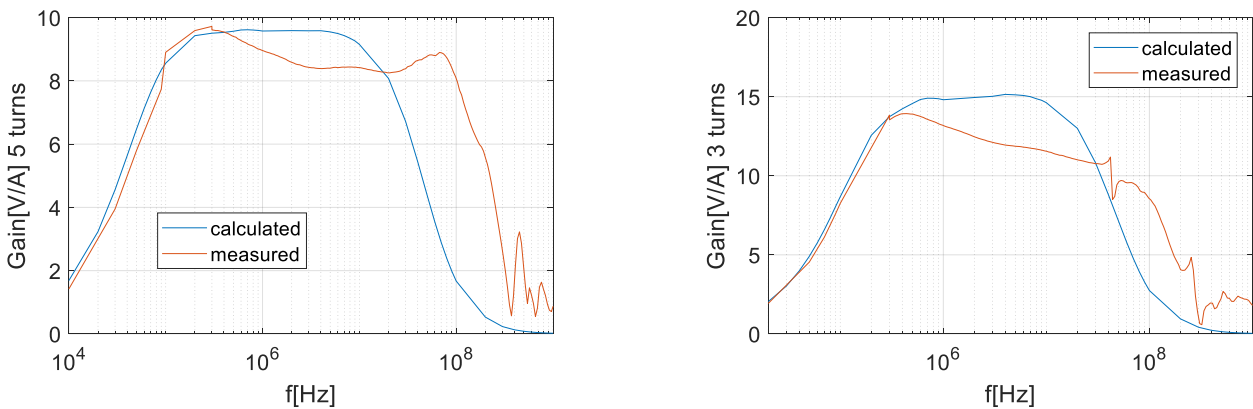


Figure 20. 5 turns (left) and 3 turns (right) HFCTs comparison between measured and calculated gain

The low cutoff frequency is determined by the inductance. At low frequencies, the HFCT is not capable of reading the signal because of the low induced voltage. At a certain frequency a flat response is obtained till the top cutoff frequency, caused by the parasitic capacitance. The sensitivity decreases because at higher frequencies the permeability of the core decreases and the parasitic capacitance of the HFCT takes an important role.

The peaks are the resonances between the parasitic capacitances and the inductance of the HFCT. The measured gain deviates from the calculated one when the frequency increases. As the frequency increases,

the parasitic capacitances and inductances have more impact. Thus, the measurement and calculation lose accuracy for higher frequencies.

3.1.4. Charge calculation method

Figure 20 and equation 15, show that the HFCT does not measure DC components, there is no change in the magnetic flux, so no voltage is induced. When a pulse is measured with a CT, the pulse has a similar shape, but the DC component will be cancelled with a negative lash at the end of the pulse. This can be seen in Figure 21.

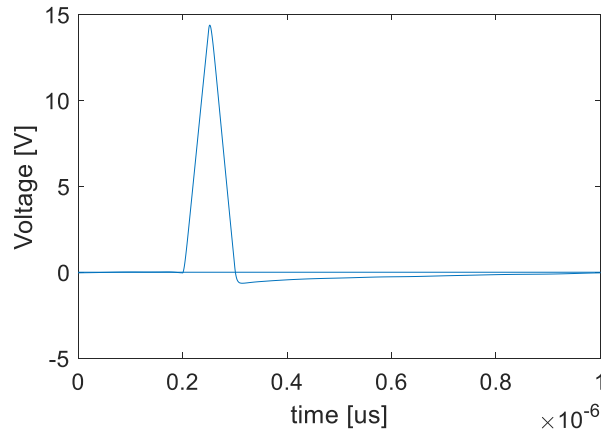


Figure 21. 100 ns pulse output in a 3 turns CT

Calculating the charge by means of the area under the curve gives zero. There are two methods presented in [13], to calculate the charge from a pulse. One method is by using the lowest frequency after DC, which will be similar to the DC value (Chapter 2 section 4). This method cannot be used for a PD in the GIS; reflections and oscillations of the pulse are measured, giving a distorted spectrum of the signal (Figure 22).

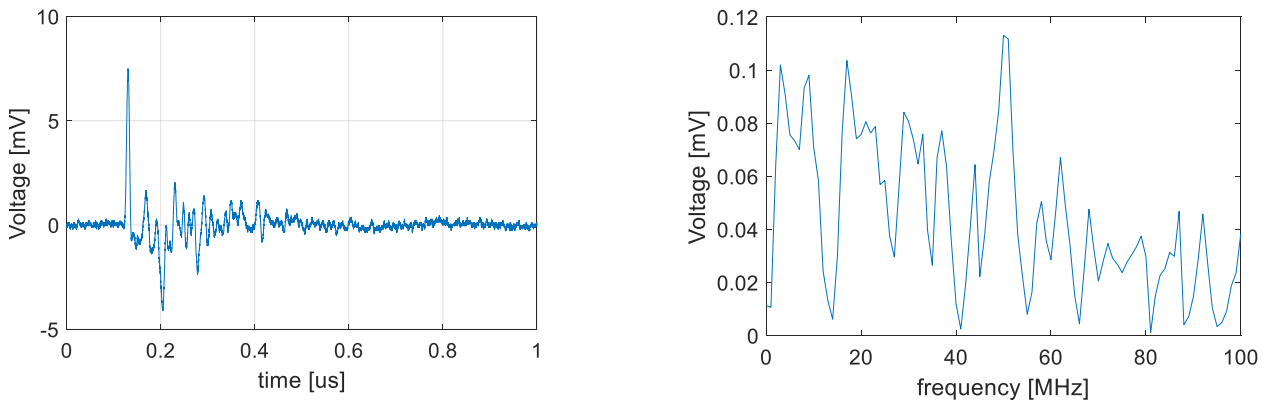


Figure 22. Measurement of a pulse in the GIS (left), frequency spectrum of the pulse (right).

The other presented method is by means of calculating the area of the first pulse, limiting the range to the first zero crossing (Figure 23).

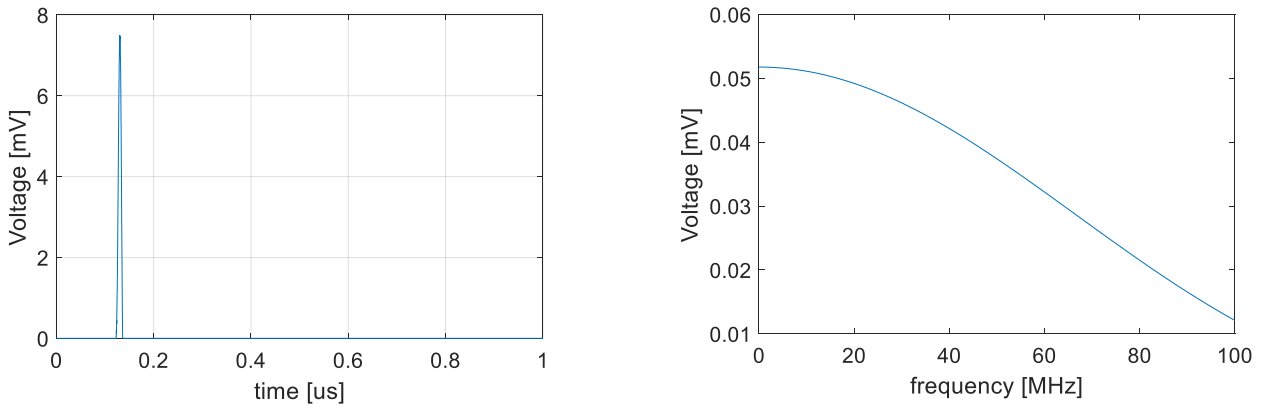


Figure 23. Signal processed of a measurement of a pulse in the GIS (left), frequency spectrum of the pulse (right).

This gives a good approximation but depends on the lower cut off frequency of the CT, giving lesser error for lower cut-off frequency. Therefore, it is important the selection of number of turns of the CT, the lower the number of turns the higher the low-cut-off frequency. The error will also depend in the duration of the pulse. For shorter durations, the error decrease, which is convenient in our case; PD's in SF₆ are in the order of nanoseconds.

To get the HFCT response to a pulse input, first the input pulse is represented in the frequency domain. Using the transfer function (Gain) of the HFCT, the output is obtained by a convolution:

$$V_{out}(\omega) = V_{in}(\omega) * G(\omega) [V] \quad 22$$

By Transforming V_{out} to the time domain using Fourier inverse transform, the pulse in Figure 21 is obtained. Furthermore, the area can be calculated to the first zero crossing. The error is calculated comparing the area from the input pulse and the area of the output pulse times the transfer function (equation 23). The errors for different CT's and pulse durations are presented in Table 3. It can be seen that the short duration of the pulse reduces de error. Also using more turns in the secondary of the CT decreases the error.

$$error = 100 * \frac{Q_{in} - Q_{out}}{Q_{in}} [\%] \quad 23$$

Where:

Q_{in} = Charge measured in the primary circuit of the HFCT.

Q_{out} = Charge measured in the secondary circuit of the HFCT

	Error 100 ns Pulse	Error 10 ns Pulse
3 turns	5.05 %	0.78 %
5 turns	1.87 %	0.16 %
10 turns	1.31 %	0.11 %

Table 3. Error for different CT's and pulse durations

To simplify the calculations and thus increase the signal processing speed, the gain is taken constant in the frequency domain. Therefore, the most suitable gain must be chosen for the more accurate charge calculation.

As it was mentioned in Chapter 2, the information of the charge is contained in the DC and low frequencies components. Therefore, the most convenient gain for charge calculation, is the one with the lowest measured frequency. For instance, in a 1 μ s window measurement, the minimum measured frequency will be 1 MHz. It is also recommended to use the gain in the range of frequencies below 1 MHz, where the parasitic elements do not have any effect. With higher frequencies the calculated and measured gain of the sensor loses accuracy.

The disadvantage of using a constant low frequency gain is that the high frequencies magnitudes are reduced from its original value. If the magnitude of the high frequencies is reduced, the post-processed waveform is

distorted and thus, have lower peak magnitude but a longer duration. When the wave form has a longer duration, then, superposition of the incident and reflected pulses is more likely.

Let's name "Pulse" the calculated input pulse using frequency dependent gain and "Pulse*" the calculated pulse using constant gain. To compare the wave shape of each different calculated pulse, a 2 ns pulse was simulated. The Pulse and the Pulse* are calculated using equations 24 and 25 respectively.

$$V_{inpulse}(\omega) = V_{out}(\omega)/G(\omega) [V] \tag{24}$$

$$V_{inpulse}(\omega) * = V_{out}(\omega)/G(\omega_0) [V] \tag{25}$$

Where:

$G(\omega)$: is the frequency dependent gain.

$G(\omega_0)$: is the gain at a frequency ω_0 .

Figure 24 (left) shows the comparison between the Pulse and the Pulse*. As it was mentioned before, due to the reduction of the higher frequencies, the Pulse* has a lower peak magnitude but a longer duration. Figure 24 (right) shows how the magnitude of the signal for low frequencies is maintained the same for both pulses. On the other hand, the high frequencies are reduced due to the use of a constant frequency. This detail it is very important for the measurement of PD's in the real GIS due to the reflections and resonances. In section 5.4. it is shown that better results are obtained using a constant gain, due to reflections it is difficult to obtain the input pulse.

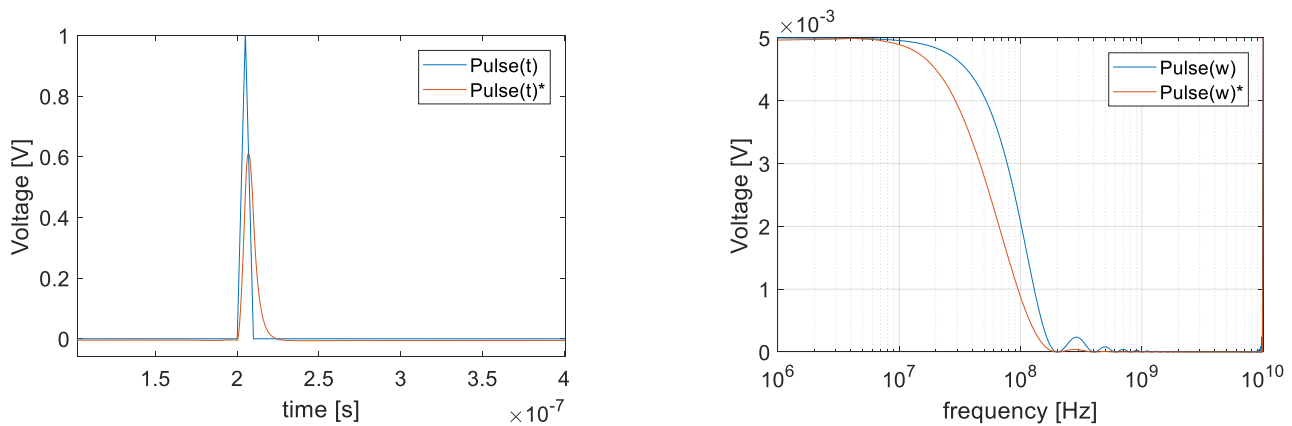


Figure 24. Pulse comparison using a constant gain in the time domain (left), and frequency domain (right).

3.2. Resolution

The resolution describes how precise the sensor is capable of measuring. The resolution depends on the type of measuring done (optical, audio, image etc.). In our case, the resolution is how small a signal can be measured before it is lost with the background noise and interference. The most important noise in the GIS is the thermal (white) noise, which is generated due to the resistance of the CT and the amplifier. The signal to noise and distortion ratio (SNR), measures the relation of the signal of interest and the noise/interference (equation 26).

$$\frac{S}{N} = 20 \log \left(\frac{V_{RMSs}}{V_{RMSn}} \right) [dB] \tag{26}$$

Where:

V_{RMSs} =RMS signal of interest voltage [V].

V_{RMSn} =RMS back ground noise/interference voltage [V].

The SNR will depend in the measured signal. In the case of PDs, the signal is never constant, its magnitude is unpredictable and depends of many factors. Therefore, it is not possible to establish a fixed SNR in PD measurement. In chapter 7, different SNR are established according to the type of discharge.

3.3. HFCT calibration

A pulse with a known charge was measured to compare the output in the CT. Using the calibrator LDC-5/UHF (Device 6), pulses with different charges were injected to the HFCT and an oscilloscope (Device 3). The pulses were measured in the primary (Ch1) and secondary (Ch2) of the HFCT (Figure 25).

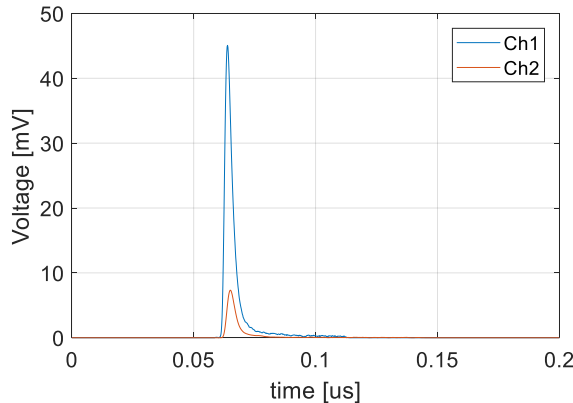


Figure 25. 4pC pulse in a HFCT and 50Ohms circuit

For the pulse in the primary circuit, the charge is obtained dividing the measured voltage over the resistance of 50Ω and then integrating over the period. To measure the charge in the secondary of the HFCT, the obtained voltage is divided over the gain of the sensor and integrated over time (equation 27).

$$Q = \int_{t_0}^{t_1} \frac{V(t)_{out}}{G(\omega_0)} dt [C] \quad 27$$

Where:

t1: time when the first pulses crosses to zero.

t0: time when the pulse starts.

The results using a 5 and 3 turn HFCT, with a gain at 1MHz are presented in Table 4 and Table 5 respectively. The error is calculated using equation 23.

Calibrator output [pC]	Primary circuit charge [pC]	Secondary circuit charge [pC]	Error Primary/Secondary
4.04	4.04	3.95	2.23 %
40.4	40.2	39.0	2.98 %
408	408	384	5.88 %

Table 4. Measured charges using a 5 turns CT

Calibrator output [pC]	Primary circuit charge [pC]	Secondary circuit charge [pC]	Error Primary/Secondary
4.00	3.90	4	-2.56 %
40.0	39.2	35	10.71 %
400	393	346	11.96 %

Table 5. Measured charges using a 3 turns CT

Three observations are important from the results:

1. Using the presented technic in [13], with the area under the curve; the charge can be estimated with good approximation.
2. The error increases with a higher charge injected. The injected pulse increases it's duration with the magnitude. The measurement in the HFCT losses accuracy for longer duration pulses.
3. The 5 turn CT shows more accurate results than the 3 turns CT. The reason might be that the 5 turn CT have a higher range of frequency with constant gain, also, the 5-turn CT has lower cutoff frequency, so more accurate low frequency measurements and less pulse distortion.

3.4. Reflected primary impedance

Another important characteristic of the sensor is the equivalent impedance seen in the primary, this impedance will have an important impact on the interaction with the GIS as will be seen in Chapter 5. To calculate the equivalent impedance, the same equations and procedure as with the gain is used. In this case we are interested in the relation V_1/I_1 :

$$\frac{V_1}{i_1} = Z_{in} = j\omega L_1(\omega) + \frac{\omega M(\omega)^2}{j\omega L_2(\omega) + Z_{eq}} [V/A] \quad 28$$

A low input impedance is obtained at low frequencies because of the low induced voltage. At a certain frequency the reflected impedance is almost the coaxial cable impedance over the square of the number of turns $50\Omega/N^2$. At higher frequencies, the core losses have higher impact and the impedance increase, till a certain frequency where the inductance is too low, and the parasitic capacitance has a higher effect, thus, the total impedance decreases. Figure 26 shows the calculated reflected impedance for a 5 and 3 turns HFCT respectively.

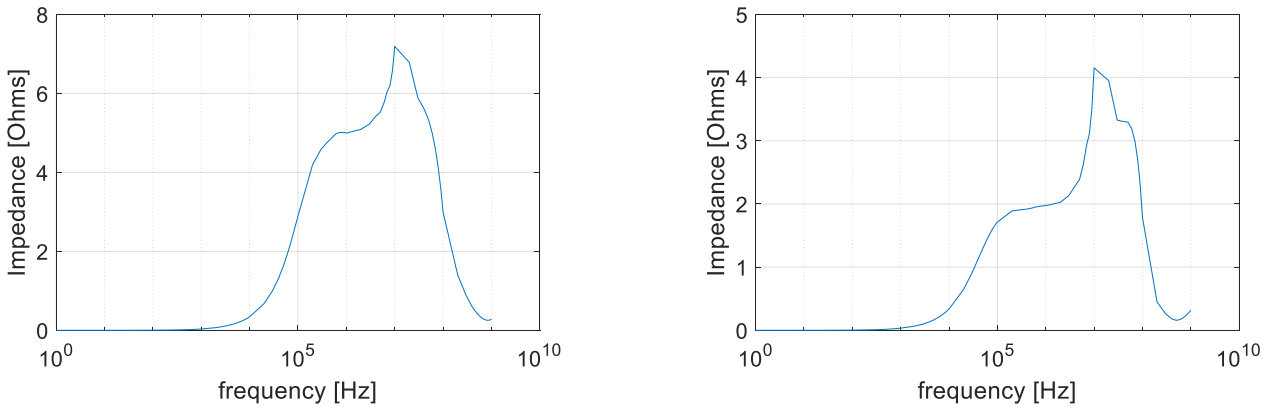


Figure 26. 3 turns (left) and 5 turn (right) HFCT primary reflected impedance.

To measure the reflected impedance in the primary, a set-up illustrated in Figure 27 was performed. The function generator is connected in parallel with a load of $1\text{ M}\Omega$ from the oscilloscope and the connection in series of the HFCT and a load of $50\ \Omega$ of the oscilloscope.

The current that goes through the branch of the HFCT is known by dividing the Voltage of the $50\ \Omega$ over the same resistance. And the voltage of the whole branch is the same as the measured in the $1\text{ M}\Omega$, so the impedance can be calculated in the following way:

$$Z = \frac{V_{1M} * 50}{V_{50}} * (\cos(\theta_{1M} - \theta_{50}) + j\sin(\theta_{1M} - \theta_{50})) - 50 - Z_{line} [\Omega] \quad 29$$

Where:

Z_{line} : represents the voltage drop due to the coaxial cable that connects each component, for high frequencies this parameter becomes important.

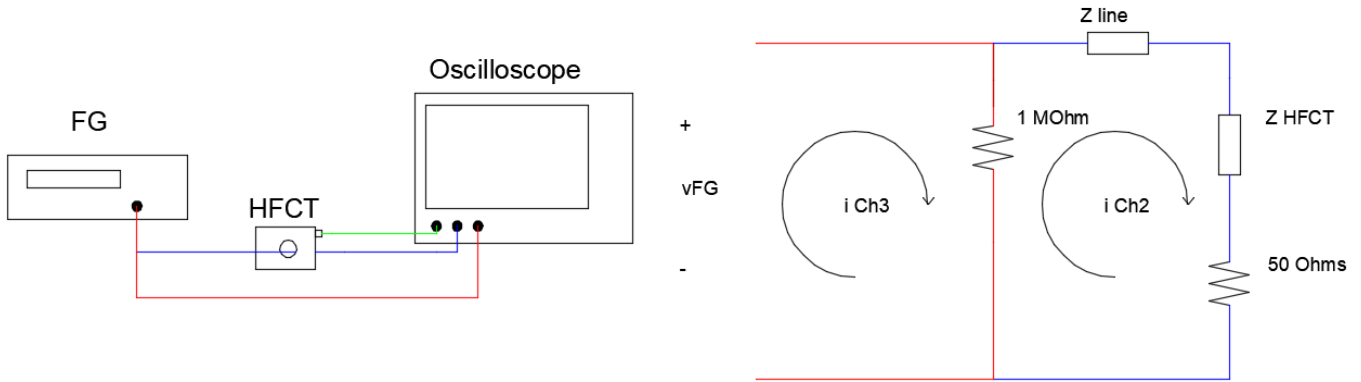


Figure 27. Setup for measuring the reflected impedance of the HFCT

The impedances are found for two frequencies; 1 MHz and 10 MHz. The importance of the reflected primary impedance is explained in chapter 5. In this setup, more components and coaxial cables were used, thus, increasing the uncertainty of the measurement.

	3CT	5CT
1MHz	$4.96+j1.2 \Omega$	$1.32+j0.18 \Omega$
10MHz	$6.23+j0.95 \Omega$	$1.44+j4.56 \Omega$

Table 6. Reflected impedance for a 3 and 5 turns HFCT for 1 and 10 MHz

3.5. Chapter conclusions

To provide the calibration method, the electric behavior of the CT and the GIS must be calculated. The transfer function of the sensor was calculated. The calculated gain is compared with measurements, giving similar results for frequencies below 10 MHz. Three CTs with 3, 5 and 10 number of turns were compared, giving different gains and bandwidths. The results showed that the 3 and 5 turns CT are the most suitable. Different pulses with known charges were measured directly with the HFCTs, using a PD calibrator. The calculated charges gave similar results with errors below 12 % for both sensors. The most important characteristics of each HFCT are summarized in the following table:

	3 turns	5 turns	10 turns
Gain	14.77 V/A	9.56 V/A	4.94 V/A
Bandwidth (cut off frequencies)	0.15-50 MHz	0.06-40 MHz	0.02-40 MHz
Reflected primary inductance 1 MHz	4.98 Ω	1.97 Ω	0.55 Ω
Charge measurement error	0.78-5.05%	0.16-1.87%	0.11-1.31%

Table 7. HFCT characteristics summary

The measured pulses will have a different output when the CT is installed in the GIS. The GIS has its own electric behavior and in combination with the HFCT gives a different pulse shape. In the next chapter the electric parameters that affect the pulse sensing are calculated and measured.

4. GIS characteristic

The measured pulse is dictated by the electric characteristics of the sensor (HFCT) and the circuit in which is installed (GIS), therefore, it is important to determine the affecting parameters of the GIS. In this chapter, the characteristic impedance and propagation speed of GIS elements are calculated. The parameters are computed by means of calculation and measurements in the GIS. All the experiments are based on the diagram of the GIS presented in Figure 28, in this diagram the location of the HFCT and UHFS are presented. A full-page figure of the GIS is added in the appendix.

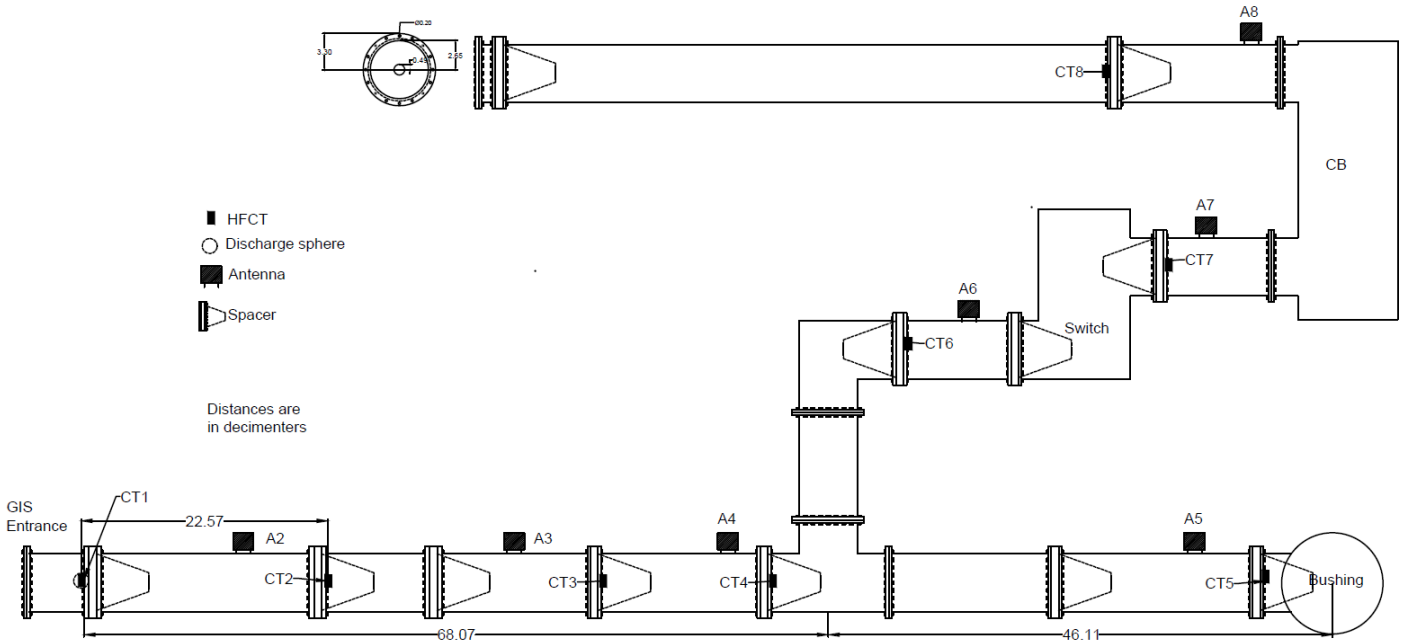


Figure 28. GIS layout with location of UHFS (A#) and HFCT (CT#)

4.1. Characteristic impedance and phase velocity

A PD in SF₆, is a very fast signal, in the range of nano seconds, At the speed of light “c”, the pulse can measure a few meters. Therefore, the GIS act as a transmission line, and the circuit must be analyzed using the telegraph equations. To calculate the parameters of the GIS, measurements were done in different sections. Figure 28, shows a CAD drawing of the GIS used for the tests. The drawing shows the locations for the HFCT and UHFS, where CT refers to a HFCT and A to a UHFS.

There are 3 types of EM propagation: TEM, TE and TM. Unlike the antenna sensor, the HFCT is only capable of measuring TEM. Therefore, it is only important to find the characteristic impedance (Z_0) and phase velocity (V_p) for this mode in each section of the GIS. In equation 30 and 31 the calculation of Z_0 and V_p are shown.

$$Z_0 = \sqrt{\frac{L}{C}} \text{ [}\Omega\text{]} \quad 30$$

$$V_p = \frac{1}{\sqrt{LC}} \text{ [m/s]} \quad 31$$

The GIS is a coaxial structure with the enclosure and the inner conductor (Figure 29), the characteristic Impedance can be calculated as follow.

$$Z_0 = \sqrt{\frac{\mu \ln(r_e/r_i)}{\varepsilon}} \text{ [}\Omega\text{]} \quad 32$$

Where:

r_e =inner ratio of the enclosure.

r_i = is the ratio of the inner conductor.

μ = permeability of SF₆ (\approx vacuum permeability).

ϵ = permittivity of SF₆ (\approx vacuum permittivity).

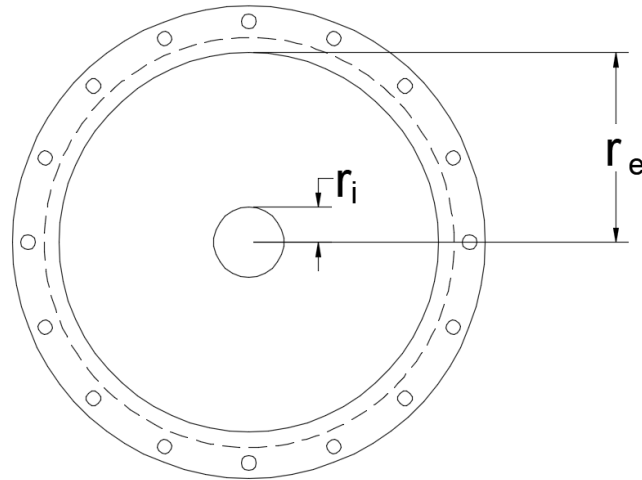


Figure 29. Coaxial structure of the GIS

The value was also obtained, simulating inductance and capacitance with a FEM software. According to the computation, the Z₀ of the GIS is $\approx 101 \Omega$ and the V_p is ≈ 300 m/ μ s.

To calculate the GIS parameters, the setup in Figure 30 was used. The pulse is sent from the pulse generator (PG) and then is divided to the oscilloscope and the GIS. When the pulse encounters the GIS part of the pulse will be reflected and the rest refracted to the GIS. In the GIS, HFCT were installed to measure the traveling wave in different sections (Figure 28).

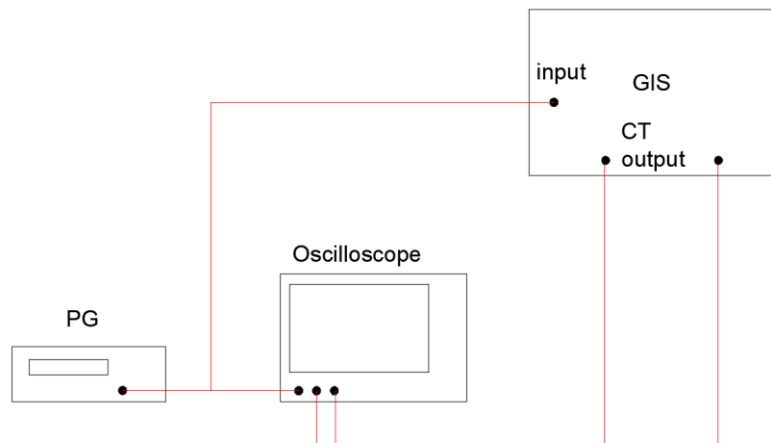


Figure 30. Setup for GIS parameters determination

To calculate the spacer propagation speed, the following procedure was used. A pulse was sent using the PG PM5712 (Device 4), this pulse is measured by the oscilloscope and sent to the GIS. Let's call this pulse the incident pulse, which is indicated with a red circle in Figure 31. The pulse in the green circle correspond to the reflection in the entrance of the GIS, and the yellow one to the reflection in the T joint of the GIS. The recorded time from the incident pulse to the yellow encircled pulse corresponds to the traveling wave through the coaxial cable, enclosure and spacers up to the T joint and back. Only the speed of the spacer is not known. By using this method, the calculated speed is 190 m/ μ s.

$$t = \frac{l_{cc}}{V_{p_{cc}}} + \frac{l_{gis}}{V_{p_{gis}}} + \frac{l_{sp}}{V_{p_{sp}}} \quad 33$$

$$V_{p_{sp}} = l_{sp} \left(t - \frac{l_{cc}}{V_{p_{cc}}} - \frac{l_{gis}}{V_{p_{gis}}} \right)^{-1} \quad 34$$

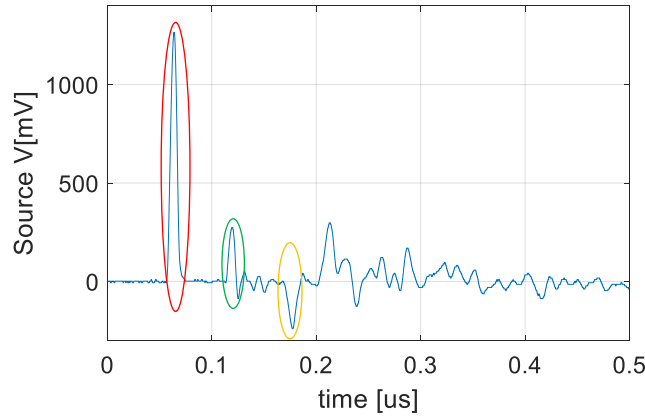


Figure 31. Pulse measurement to find the ZO of the enclosure and spacer speed propagation, red circle: incident pulse, green circle: GIS entrance reflection, yellow circle: T junction reflection

To check the validity of the spacer's V_p , sensors were placed along the GIS (Figure 28). The time in which each HFCT sense the incident pulse was measured, and by knowing the distance between them, it is possible to calculate the average speed. A generic PG (Device 5) was used, Figure 32 shows the measured pulses for the sensors in different locations. In this figure, only the first zero crossing pulse is plotted.

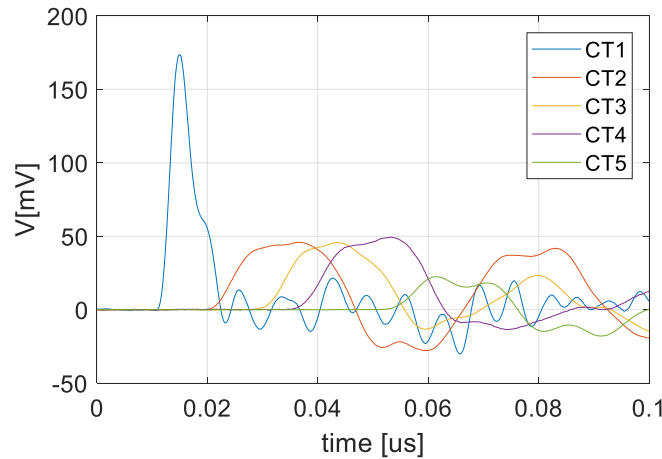


Figure 32. Measured pulses at different sections

Table 8 demonstrates the time for the incident pulse, distances of the sensors to the entrance and the average speed. The average speed is compared with a calculated one using the speed propagation in the spacer and enclosure. To calculate the error of a calculated parameter compared with a measured one equation 35 is used.

$$error = 100 * \frac{M - C}{C} [\%] \quad 35$$

Where:

M= is the measured value.

C= is the calculated value.

	CT2	CT3	CT4	CT5
Time [ns]	8.07	18.2	24.1	40.6
Distance [m]	2.19	4.76	6.3	10.8
Average speed [m/μs]	271	262	262	266
Calculated speed [m/μs]	280	272	272	276
Error [%]	-3.17	-4.00	-4.02	-3.67

Table 8. Speed calculation for wave propagation in the GIS

The error percentage comes from human factor errors, such as: approximated measured length of the GIS and indetermination of where exactly the measured pulse starts.

The Z₀ of the GIS is verified using the measurement in Figure 31. A pulse is sent from a pulse generator (PG) and the signal is divided to the oscilloscope and to the GIS. The first pulse is the incident one, the pulse travels along the coaxial cable (Z₀=50 Ω) and encounters a change of impedance at the entrance of the GIS, part of the pulse is reflected, and the rest is refracted to the GIS. The reflected pulse will travel back and is reflected again in the coaxial division between the branch of the PG and the oscilloscope.

To calculate the characteristic impedance using the measurements, the reflection equation is used (36), then, the Z₀ of the GIS is solved (equation 37).

$$\Gamma = \frac{V_r}{V_i} = \frac{Z_2 - Z_1}{Z_2 + Z_1} \quad 36$$

$$Z_2 = Z_1 \frac{(\Gamma + 1)}{(1 - \Gamma)} [\Omega] \quad 37$$

The Characteristic impedance of the GIS was calculated using the first (red, first circle) and second pulse (green, second circle), giving the results shown in Table 9. The Z₀ of the T joint is calculated comparing the first and third pulse (yellow circle). The second pulse is due to the T section, knowing the distance and the speed propagation.

	V _i	V _r	Z ₁ [Ω]	Z ₂ [Ω]	%error
GIS entrance	1.266	.274	50	98	2.97
T joint	.147	.044	98	52	5.94

Table 9. Calculation of Z₀ with measurements

The Z₀ of the T joint is just the GIS divided in two: 101/2 Ω ≈52 Ω.

The Z₀ of the bushing is calculated using equation 37 and the wave measured in Figure 32 of channel 6. Knowing the transmitted wave after the T joint, it is possible to calculate the Z₀ of the bushing, which results in 236 Ω. The value of the bushing has a higher error; the Z₀ of the bushing changes along the conductor axis, therefore, the calculated value is subjected to the distance between the sensor and the bushing.

The Z₀ calculation of the spacer is more complicated. The spacer is a dielectric material which is distributed not uniformly in the z direction. The relative permeability of the material is the same as the gas in the rest of the GIS, therefore the inductance must be the same. On the other hand, the capacitance is dependent on the permittivity of dielectric material, so it will be different in the z direction (Figure 33).

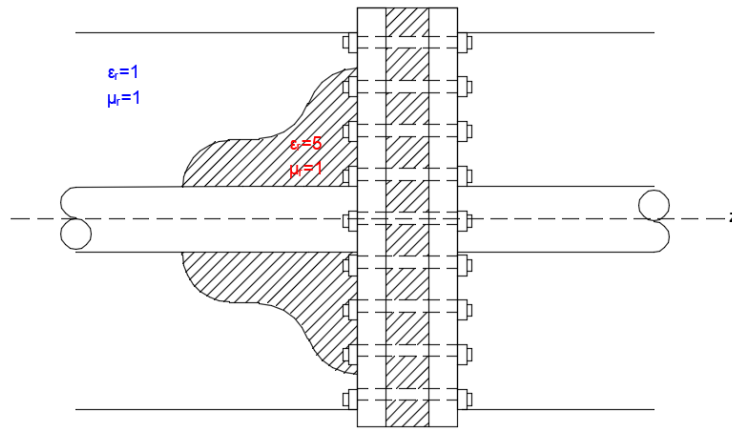


Figure 33. Difficulty of spacer capacitance due to it's geometry.

The spacer has a small length compared to the pulse width, this makes it not possible to distinguish its reflections. However, using the speed propagation in the spacer and its inductance, it is possible to calculate and average Z_0 by using equation 30 and 31. The calculated Z_0 of the spacer is: 70Ω .

To validate the calculated parameters of the different sections of the GIS, a simulation of the wave propagation was done using Matlab Simulink, RF module. The wave propagation in CT1 is simulated and compared with the real measurement. In Figure 34 a comparison between the measured (on the left) and simulated (on the right) wave is shown.

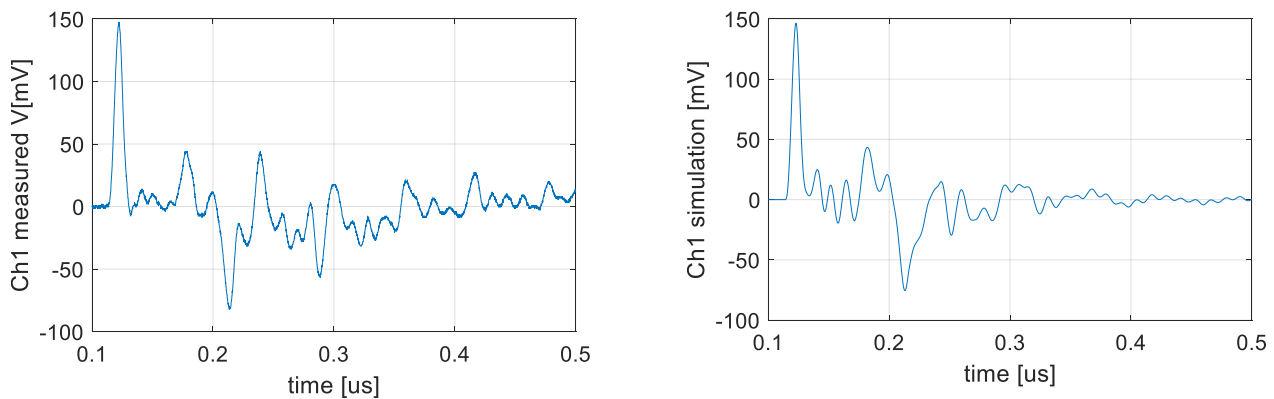


Figure 34. Reflections measured (left) and simulated (right) in CT1

Although, the simulation has a different wave shape than the measured one, the time delayed of the reflections and their magnitude give a similar value, the error is calculated using equation 35:

	Measured	Simulated	Error
T reflection time	179 ns	182 ns	1.68 %
T reflection magnitude	44 mV	43 mV	2.27 %
Bushing reflection time	214 ns	220 ns	0.47 %
Bushing reflection magnitude	82 mV	75.6 mV	7.32 %

Table 10. Time delay and impedance comparison between measurements and Simulink

Information about the characteristic impedance of the GIS's CB and switch where not found, and the calculation of them by means of finite element is beyond the scope of the thesis project. However, by measuring the pulses before and after these elements, it is concluded that their parameters are similar to the enclosure.

4.2. Chapter conclusions

The GIS has a length compared to the wave length of the pulse. Therefore, it was important to find the phase velocity and the characteristic impedance of each element in the GIS. The phase velocity helps to localize the discharge source, and the characteristic impedance determines the reflections of the traveling pulse. This information is used further this chapter to calculate the distribution of the current. Table 11 shows the summary of the approximated characteristic impedance and phase velocity of each element on the GIS.

	Characteristic Impedance [Ω]	Propagation velocity [m/ μ s]
Enclosure	101	300
Spacer	70	190
T joint	50.5	300
Bushing	236	300
Switch	x	300
CB	x	300

Table 11. Summary of the characteristics of the GIS

Once the electric behavior of the GIS is found, the interaction of it and the HFCT can be evaluated to determine the relation of the input and output pulse (transfer function).

5. Sensor and GIS interaction

Knowing the electric characteristics of the GIS and the HFCT is possible to generate models to predict the charge source by measuring the pulse. This chapter describes how the installation of the HFCT modifies the current distribution in the GIS. In chapter 3 was seen that the HFCT has an equivalent primary impedance, this impedance will have an effect in the circuit of the GIS. Consequently, the measured pulse, is shaped by the LCR (inductive, capacitive and resistive) characteristic of the sensor and GIS electric circuit.

5.1. Sensor and GIS electric circuit model

When a PD occurs, the current flows from the inner conductor to the outer and travels all along the enclosure as an EM wave. When the traveling wave encounters a spacer, the current flows through the bolts. The distribution of the current depends on the impedance of each path. Fixing the HFCT in the bolt adds an extra impedance to the bolt, hence reducing the current. The induced impedance of the HFCT, is the primary reflected impedance of it (found in chapter 3). Therefore, the output measured current will not only depend on the gain but also in the interaction of the HFCT with the GIS.

The conducting path of the bolt is about 16 cm. The bolt is short enough compared to the pulse width, so it can be considered as a lumped element.

The impedance of the bolt will be the electric equivalent of a resistance in series with the self-inductance and the mutual inductance of the other bolts and of the inner conductor of the GIS. Also, there is a capacitance between the bolt and the flange. This capacitance can be seen in Figure 35.

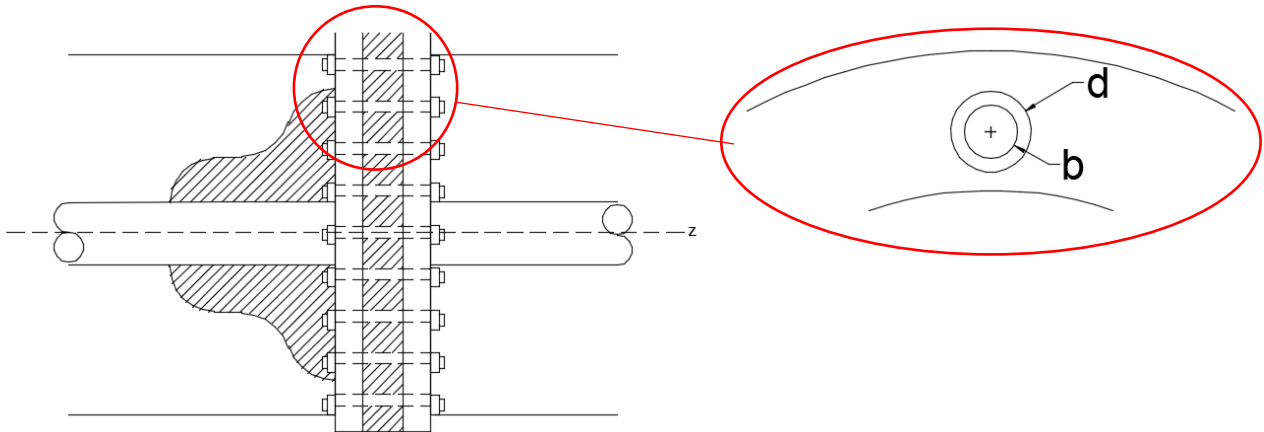


Figure 35. Parasitic capacitance in the bolt path

The capacitive reactance between the bolt and the flange is considered as a cylindrical capacitance:

$$X_c = \frac{1}{j\omega} \frac{\ln(d/b)}{2\ell n\pi\epsilon} [\Omega] \quad 38$$

Where:

n : is the number of bolts.

ℓ : Is the length of the bolt which goes through the flange, in meters.

d : is the outer diameter

b : is the inner diameter

ϵ : is the permittivity of the medium, in this case is air.

All the bolts which hold the flange can be considered as parallel conductors. According to [14] the self-impedance and mutual impedance of parallel conductor is calculated using equation 39 and 40 respectively.

$$Z_{jj}(\omega) = R + Z_{eq} + j\omega \left(L\ell + \frac{\mu}{2\pi} \left(\ell \ln \left(\frac{\ell + \sqrt{\ell^2 + r^2}}{r} \right) - \sqrt{\ell^2 + r^2} + r \right) \right) [\Omega] \quad 39$$

$$Z_{ij}(\omega) = j\omega \left(\frac{\mu}{2\pi} \left(\ell \ln \left(\frac{\ell + \sqrt{\ell^2 + D_{ij}^2}}{D_{ij}} \right) - \sqrt{\ell^2 + D_{ij}^2} + D_{ij} \right) \right) [\Omega]$$

40

Where

L =internal inductance ($\mu\ell/8\pi$) [H].

r =conductor radius [m].

D_{ij} =distance between conductor j and i [m].

r =conductor resistance [Ω].

ℓ = is the length of the parallel conductors [m].

Z_{eq} =any impedance connected in series with the bolt such as the HFCT [Ω].

The equivalent circuit of the model is presented in Figure 36, using the same method as in [15], the current in each bolt is found.

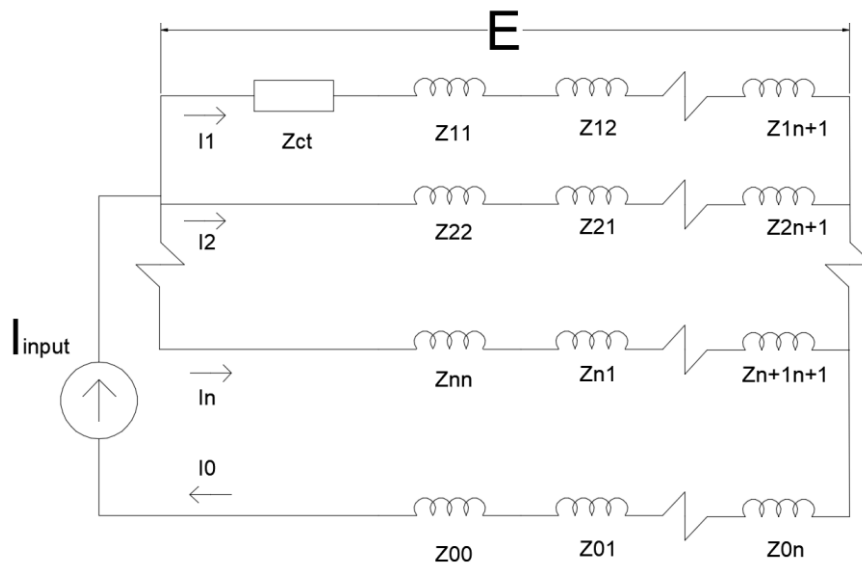


Figure 36. Equivalent electric circuit of the bolts and inner conductor

The voltage in each bolt is

$$[E(\omega)] = [I(\omega)][Z(\omega)]$$

41

Where

$[E]$ is a vector of the potential in each bolt. The potential difference from the start and end of the bolt is the same for every bolt. $E_1=E_2=\dots E_{n+1}$. Here, n is the total number of paths for the current and the element 0 represents the inner conductor.

$[Z(\omega)]$ is a $(n+1) \times (n+1)$ matrix, where the diagonal represents the self-impedances and the rest of the elements the mutual impedance of the i and j element.

$$[Z(\omega)] = \begin{bmatrix} Z_{11}(\omega) & \cdots & Z_{1\ n+1}(\omega) \\ \vdots & \ddots & \vdots \\ Z_{n+1\ 1}(\omega) & \cdots & Z_{n+1\ n+1}(\omega) \end{bmatrix}$$

42

The $[I(\omega)]$ vector represents the unknown currents in each branch and $I_0(\omega) = -I(\omega) = I_1(\omega) + \dots I_{n+1}(\omega)$

$$[I(\omega)] = \begin{bmatrix} I_1(\omega) \\ \vdots \\ I_{n+1}(\omega) \end{bmatrix} \quad 43$$

K is a matrix of ones and zeros to represent the direction of the current and voltage in each branch.

$$[K] = \begin{bmatrix} 1 & 0 \\ \vdots & \vdots \\ 1 & 0 \\ 0 & 1 \end{bmatrix} \quad 44$$

$$[\hat{E}(\omega)] = [K] \begin{bmatrix} E_1 \\ \vdots \\ E_{n+1} \end{bmatrix} \quad 45$$

And

$$[\hat{I}(\omega)] = [K]^T \begin{bmatrix} I(\omega)_{input} \\ -I(\omega)_{input} \end{bmatrix} \quad 46$$

Solving for [I] and eliminating the voltages by replacing equation 45 over 41 and then into 46, the resulting equation is:

$$[I(\omega)] = [Z(\omega)]^{-1}[K]([K]^T[Z(\omega)]^{-1}[K])^{-1}[\hat{I}(\omega)] \quad 47$$

5.1.1. Current calculation in multiple paths

First, a general case is presented, the HFCT is connected in one of the bolts, and the current is free to flow in any of the bolts in the flange-spacer-flange connection. This is the case where less current will flow through the bolt of the HFCT.

The current distribution was computed using the procedure explained before. The results were compared with real measurements. The input current pulse is known by measuring the current at the entrance of the GIS (CT1). Then, the measured current in the CT in a spacer (CT3) is compared with the input current, applying the corresponding reflections. Table 12 shows the percentage of current flowing through the primary of the HFCT. The peak current of CT3/CT1 is compared. To calculate the error equation 35 is used.

# of turns CT	Current peak [%] calculated	Current peak [%] measured	Error
3	3.7 %	4.9 %	-25.1 %
5	5.1 %	6.0 %	-14.8 %
10	5.3 %	6.2 %	-14.7 %

Table 12. Results of current ratio for different CT's and different frequencies

The flange is fastened with 16 bolts, ideally, the current in each bolt would be 1/16. However, the reflected impedance in the primary of the CT, adds an extra impedance for the current, reducing its magnitude. The more number of turns in the CT, the lower the reflected impedance. It is clear to see that if the rest of the bolts are not insulated, a lot of sensitivity is lost. In conclusion, it is recommended to use insulating washer in the rest of the bolts, to guaranty that all the current flows in one bolt.

The main reason of error between the calculation and the measurements is attributed to the geometrical factor. The mutual and self-inductances are calculated assuming that are parallel conductors and that their intersection is smooth without any other mutual inductances.

5.1.1. Current calculation in a single path

In this case, the bolts and the flange are connected with an insulating washer, only the bolt with the HFCT will have a conductive path, this is the recommended case in a real situation. Almost all current will flow through the HFCT bolt, and a leakage displacement current will flow through the capacitance of the other bolts.

When only one conductive bolt exists, the inductance of it becomes important for high frequencies. When the traveling wave reaches the spacer, it encounters the impedance of the bolt and the spacer. This changes the characteristic impedance of the transition point, thus, the relation of the incident and refracted wave changes. The bolt and the spacer length are too short compared to the traveling wave, hence, they can be treated as a lumped element. Figure 37 shows a representation of the impedances which the wave encounters.

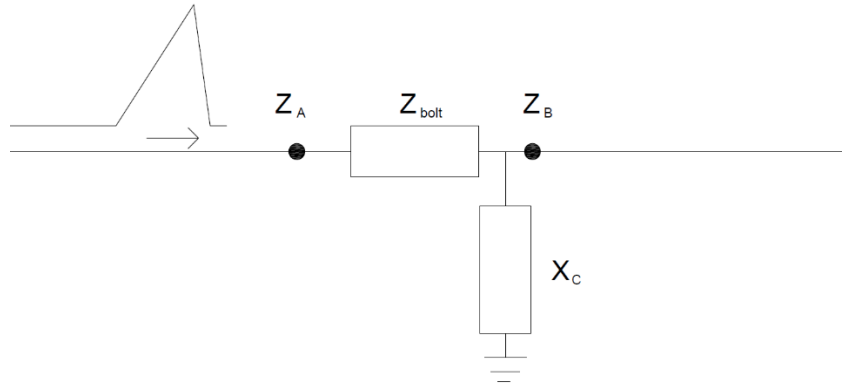


Figure 37. Traveling wave through the bolt with CT

Following the similar procedure as in ([16], pg. 128), and using equation 36, the reflection coefficient at point A will be:

$$\tau_A(\omega) = \frac{Z_b(\omega) + Z_p(\omega) - Z_A}{Z_b(\omega) + Z_p(\omega) + Z_A} \quad 48$$

Where:

$Z_b(\omega)$: Equivalent impedance of the bolt and the HFCT in series with the parallel sum of

$Z_p(\omega)$: Equivalent impedance of the parallel sum of the GIS Z_0 and the capacitive reactance of the spacer.

Z_A : Characteristic impedance of the GIS before the spacer

The expression for the voltage at point A is:

$$E_A(\omega) = E(\omega)\{1 + \tau_A(\omega)\} = \frac{2E(\omega) + Z_p(\omega)}{Z_b(\omega) + Z_p(\omega) + Z_A} [V] \quad 49$$

Where:

$E(\omega)$: is the incident voltage pulse.

Consequently, the current that flows through the bolt with the HFCT is:

$$I_{bolt}(\omega) = \frac{2I_A(\omega)Z_A}{Z_b(\omega) + Z_p(\omega) + Z_A} [A] \quad 50$$

And the refracted current that travels through the GIS after the spacer is:

$$I_B(\omega) = I_{bolt}(\omega) \frac{X_c(\omega)}{X_c(\omega) + Z_B} \quad [A] \quad 51$$

Where:

Z_B : is the characteristic impedance of the GIS after the spacer, it is considered the same as Z_A .

$X_c(\omega)$: is the equivalent capacitive reactance of the spacer.

A fast pulse was measured directly to the oscilloscope and in the CT at the GIS entrance. Using the incident measured pulse, equation 51 and the gain of the HFCT, the pulse was calculated. The incident measured pulse, the measured pulse in CT1 and calculated pulse in CT1 are shown in Figure 38.

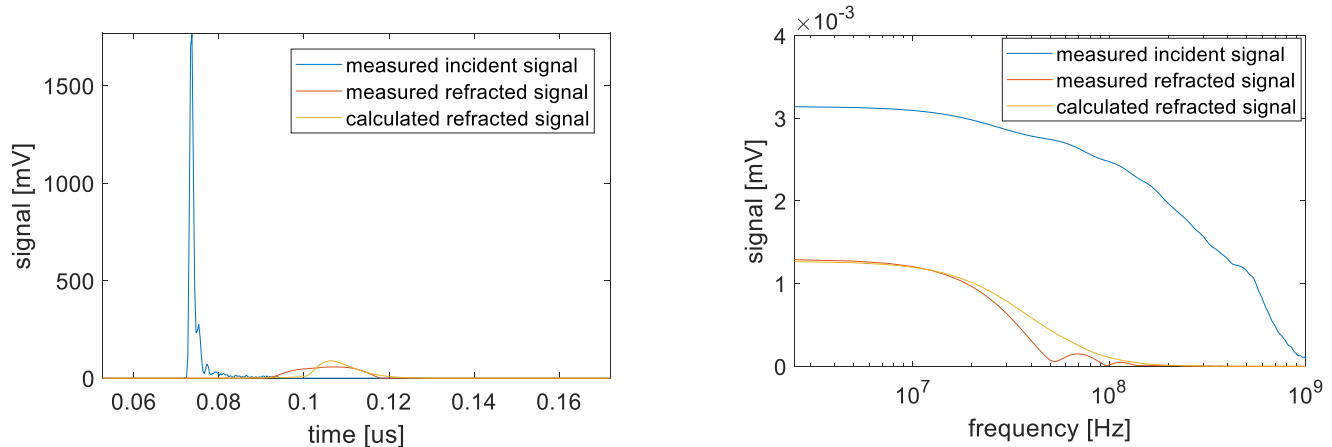


Figure 38. Incident and refracted pulses in the time (left) and frequency (right) domain

The higher frequencies get more attenuated due to the increasing of the inductive reactance of the bolt and the decreasing of the capacitive reactance. Resulting in the reduction of the peak magnitude of the pulses. The main error between the measured and calculated refracted pulse is because is impossible to consider all existing parasitic elements.

5.1.2. Current through bridges

The grounding arrangement of a GIS substation shall ensure that touch and step voltages are limited to safe values, as stated in IEEE std. 80-200. Therefore, the enclosures of the GIS shall be grounded at several points. The ground continuity between each enclosure shall be maintained; copper/aluminum bridges are connected to give continuity between flanges [17], see Figure 39.



Figure 39. Bridge between to flanges.

The bridge reduces the current flow in the bolt of the HFCT. Using equation 47, the current in the HFCT bolt can be calculated. The rest of the bolts are insulated. A diagram of the distance ("x") of the bridge to the

bolt where is installed is shown in Figure 40. Figure 41 shows how the current percentage changes depending with the distance of the bridge to the installed bolt, for 5 and 3 turns HFCT.

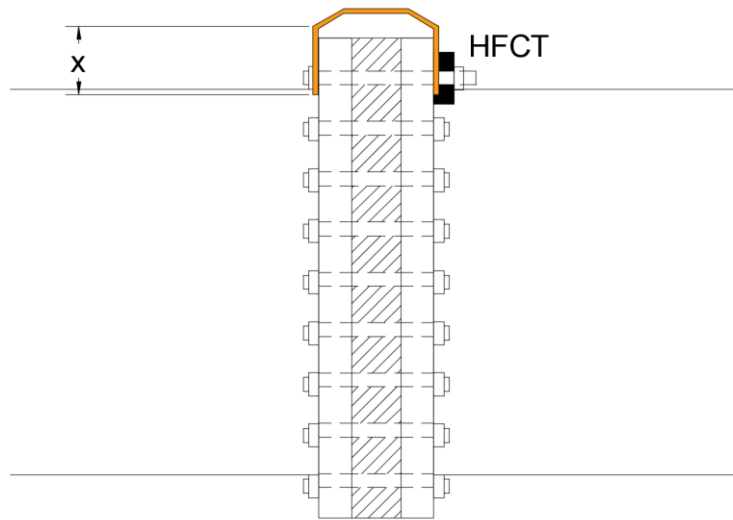


Figure 40. Representation of the the bridge situated in different positions.

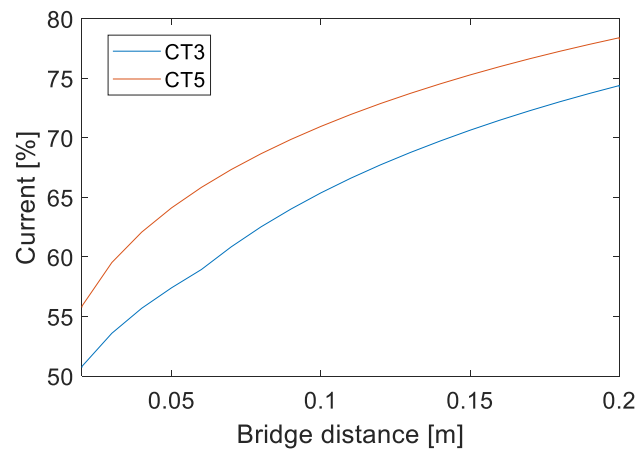


Figure 41. Current % in the HFCT bolt for different distances of the bridge

Depending in the position and distance of the bridge, the sensitivity of the HFCT is different. The results are compared with measurements done with different positions of a bridge, with a 5 and 3 turn HFCT. Table 13 and Table 14 show the results of the proportion of current in the HFCT, equation 35 is used for the error calculation. The peak current in the CT without any bridge is compared with the peak current when a bridge with different distances exist.

Distances	Measured	Simulated	Error
4 cm	58.3 %	62.1 %	6.52 %
20 cm	81.3 %	78.4 %	-3.57 %

Table 13. Measured and calculated current percentage for different bridge distances with a 5 turns HFCT

Distances	Measured	Simulated	Error
4 cm	54.3 %	55.7 %	2.58 %
20 cm	77.7 %	74.4 %	-4.25 %

Table 14. Measured and calculated current percentage for different bridge distances with a 3 turns HFCT

5.2. Current distribution

When a discharge appears inside the GIS a current will flow from the inner conductor to the outer conductor. The current will be distributed in the conductor depending in the impedance of each infinitesimal part of the material. This means that more current density will be found in the shorter paths, with less resistivity and less induced electric field. The current density will depend on the so called diffusive fields. Neglecting the displacement current (capacitive currents) we get the diffusive equations from Maxwell's equation, in the frequency domain:

$$\nabla \times \hat{H} + \hat{j} = 0 \quad 52$$

$$\nabla \times \hat{E} + s\mu\hat{H} = 0 \quad 53$$

$$\hat{j} = \sigma\hat{E} \quad 54$$

Where:

\hat{H} is the magnetic field vector in x, y and z direction.

\hat{j} is the current density vector in x, y and z direction.

\hat{E} is the electric field vector in x, y and z direction.

μ is the permeability of the medium

σ is the electric conductivity of the conductor

s is the complex number

Taking the rotation for equation 53 and solving for \hat{j} we ended with the following equation:

$$\nabla^2 \hat{j} - s\sigma\mu\hat{j} = 0 \quad 55$$

For the case of multiple paths (more than one conductive bolt and bridges), it is important to know the distribution of the current in the GIS enclosure, near a discharge. If a discharge happens on the top of the enclosure, near a flange, the current in each bolt will be different. The bolts close to the discharge will have larger currents than the bolt farther.

In the laboratory an experiment was done to probe that the current is different in each bolt for different discharge positions. To simulate the discharge injection from the inner conductor to the enclosure, a rode was rotated along the inner conductor (Figure 42), hence, giving different discharge positions. Three sensors were place: the first one, in the rode where the inner and outer conductor are connected (CT1 position). The second one at the first encountered spacer, at 7cm. And the last sensor in the position of CT2 (226 cm). The Device 4 was used to inject the pulse.

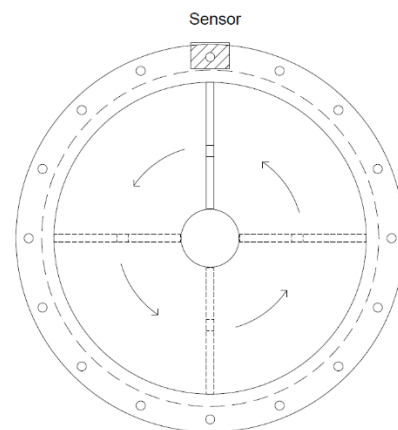


Figure 42. Measurement setup for current distribution

The percentage of current at 1MHz, in the bolt with the sensor is presented in Table 15. 16 bolts are installed in each spacer, so the current is distributed in 16 paths.

	First spacer: 7 cm	Second spacer: 226 cm
Bottom discharge	3.13%	4.55%
Top discharge	7.95%	4.55%

Table 15. Current distribution for a top and bottom discharge for 7 cm and 202 cm distance from the source to the sensor.

For 2 meters from the discharge, the current is already uniform along the enclosure, the current distribution is the same for a top and bottom discharge.

To have an estimation of how the current distributes in the enclosure, a FEM simulation was done. Figure 43 shows how the current density is distributed in the enclosure. The figure shows a view from top of the GIS. The current source is located at the point $z=1$ m. The range of the magnitude of the current density is reduced to have a better view of the flux distribution. At a distance 50 cm from the discharge the current is almost uniform in the enclosure.

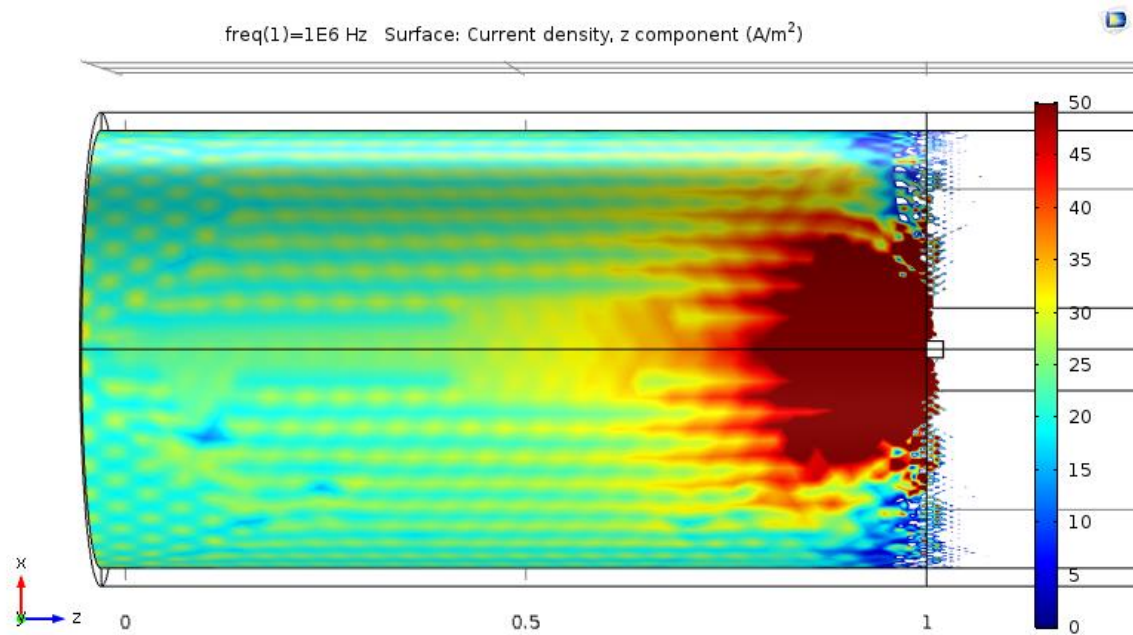


Figure 43. Current density distribution along the propagation axis (z), units in meters.

Figure 44 is a plot of the current distribution in the xy plane at 5 cm from the discharge ($z=0.95$ m). Again, the range of the magnitude of the current density is reduced to have a better view of the current distribution. The value of the current density is the norm of the x , y and z direction, so is an absolute value, for that reason the going (inner conductor) and returning (outer conductor) are both positive. The figure shows that at 5 cm, the current density is not uniform, and the majority is in the position of the discharge (left position). In the case where a discharge happens near the spacer with the HFCT, and there are multiple conductive paths, the sensitivity of the CT will change. Hence, it is important to take the current distribution into consideration.

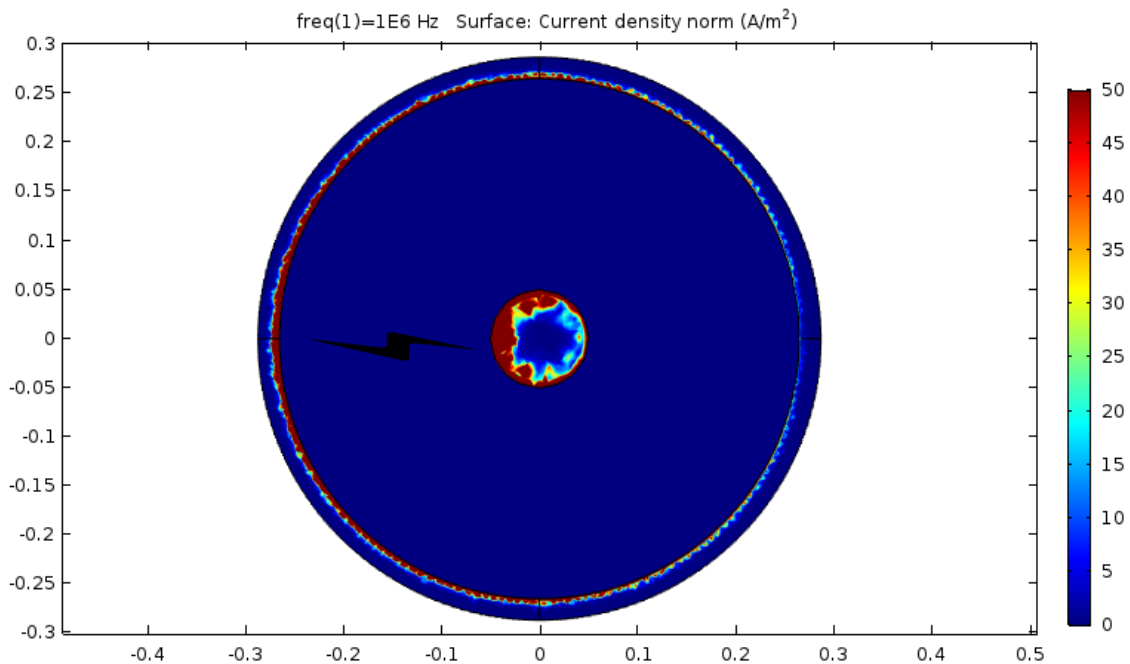


Figure 44. Current distribution at 5 cm from the discharge, units in meters.

5.3. Interference signal

The GIS is a big metallic structure; this, makes it act as a big antenna, picking up magnetic interference (MI), electric interference (EI) and electromagnetic interference (EMI). EI and MI are mainly in the power frequency and come from the power current and voltage. The EMI could make an appearance in any frequency and are mainly caused by electronic switching.

An important interference that was found in the measurements when applying high voltage, is the so-called ground loop. The ground loop is a potentially detrimental loop formed when two or more points in an electrical system that are normally at ground potential, are connected by a conducting path such that either or both points are not at the same ground potential [18]. The grounding of the GIS and the oscilloscope form a ground loop with the HFCTs and UHFSSs. The left drawing in Figure 45, shows the current path in the grounding circuit (the HV circuit is not shown). A solution, also presented in [18], is to avoid the cable shields grounded at both ends. The HFCT has the feature to connect the secondary winding to the case shielding of the sensor or to isolate the winding. The isolation of the secondary eliminates the physical grounding loop (parasitic capacitance will still exist) and therefore, decreases the interference read in the oscilloscope (Figure 45 (right)).

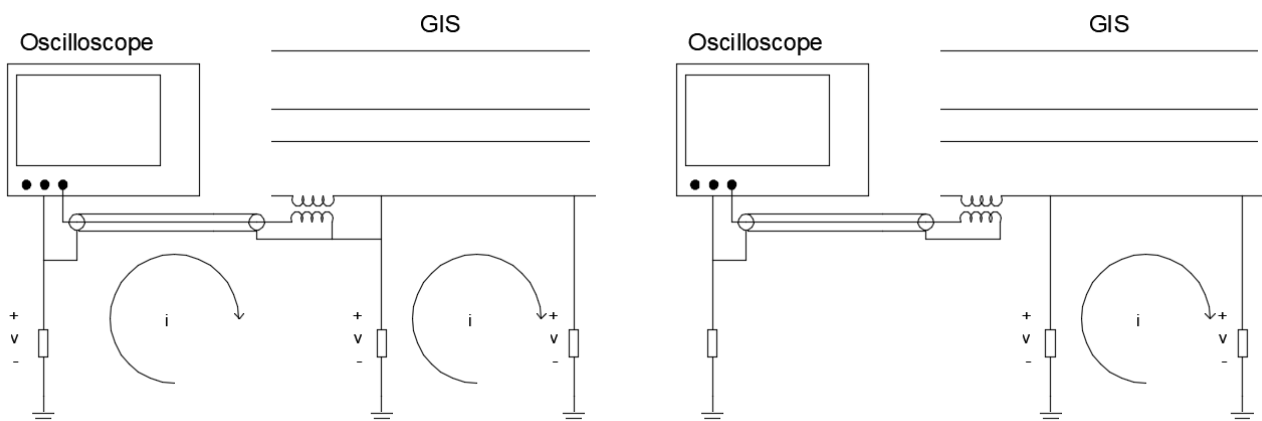


Figure 45. Ground loop from with the grounding of the HFCT (left) and solution for ground loop

5.4. Calibration in the GIS

The calibration process is used to compare the real input signal and the calculated one. A known charge is injected in the GIS using a calibrator, by measuring the signal in the HFCT and applying the transfer function it is possible to calculate the discharge and compared it with the calibrator discharge. The calibration for charge magnitude is not possible in antennas, as it was explained in chapter 2 section 6, the bandwidth of the antenna does not cover the spectrum where charge information of the pulse is.

5.4.1. Discharge magnitude with constant Gain

Knowing the transfer functions (sensor and the GIS) and the measured pulse, it is possible to calculate the incident pulse. The total transfer function is shown in equation 56.

$$\frac{V_{out}(\omega)}{I_{in}(\omega)} = G(\omega) = G1(\omega) * G2(\omega) * H(\omega) * (1 + \tau) \quad [V/A] \quad 56$$

Where:

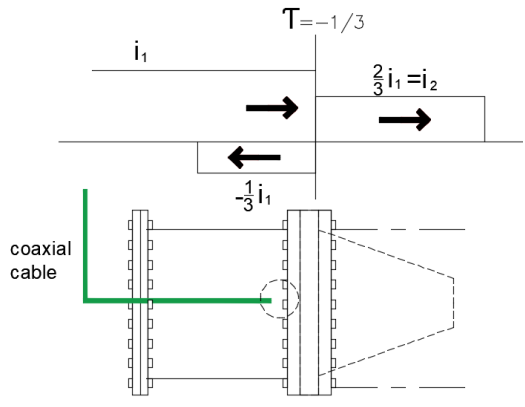
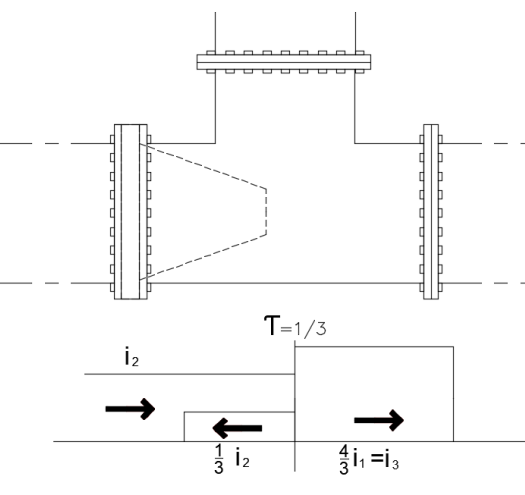
G1: is the transfer function of the HFCT, equation 15.

G2: is the transfer function of the current division in equation 51.

H: is the transfer function of the amplifier and filter used for the HFCT.

τ : Represents the reflections in the GIS.

To calculate the injected discharge, the setup in Figure 30 was used. The discharge was injected with a PD calibrator (Device 6). Different reflection factors were applied to the charge calculation depending on its location. In the following table a description and diagram of each reflection is shown.

	<p>In this experimental case, a charge was injected outside the GIS (the calibrator), the pulse will have a $-1/3$ reflection in the interface between the GIS and the coaxial cable.</p>
	<p>Also, for each different HFCT, a different reflection occurs. In CT 2, because of the long duration of the pulse, the reflection $1/3$ in the T joint is added to the incident pulse. When the pulse goes through the T section, the refracted pulse is $4/3$ of the incident pulse and divided in two by the two different paths, this factor is applied for CT 5 and 8.</p>

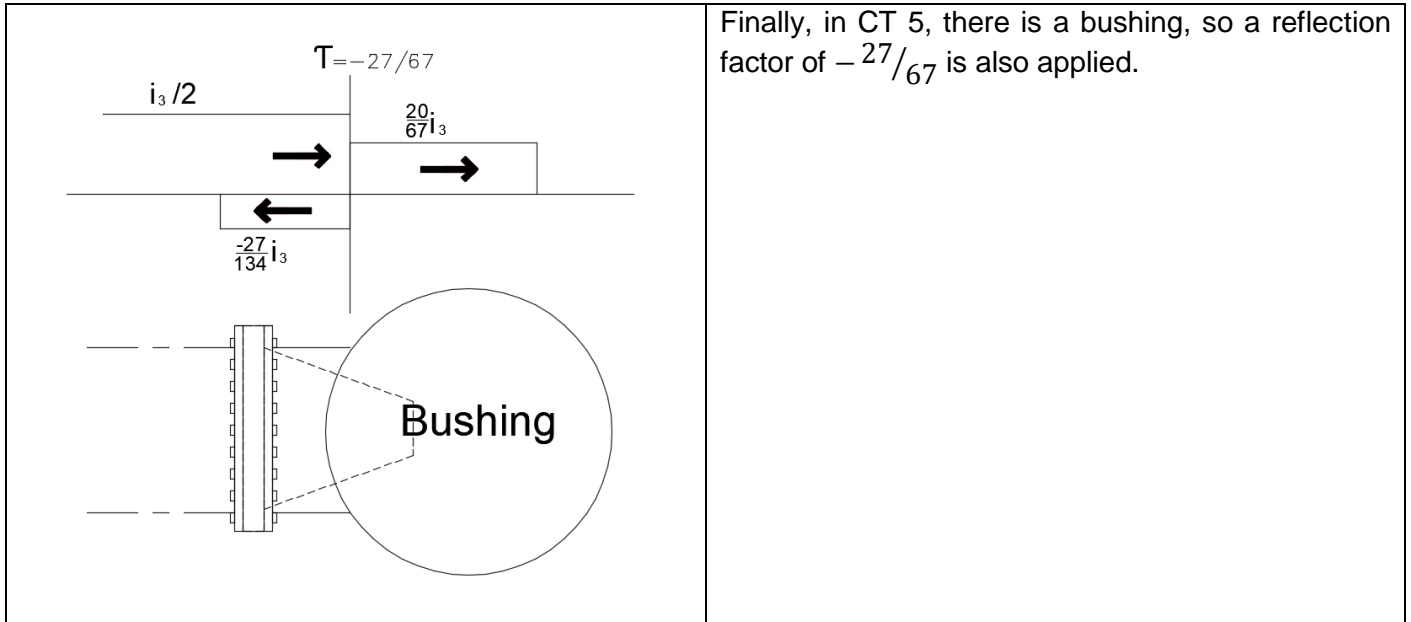


Table 16. Different reflection factors applied in the charge calculations.

The calculation of the discharge is then, using a constant Gain:

$$Q = \int_{t_0}^{t_1} \frac{V_{out}(t)}{G(\omega_0)} dt \quad [C]$$

57

Where:

t1: time where the first pulses crosses to zero, using the method presented in [13].

t0: time where the pulse starts.

Figure 46 shows measurements using a 3 turns CT, in CT2, CT5 and CT8 for a pulse of 40 pC. By applying equation 57 with 1 MHz frequency, a good approximation of the charge is obtained for each sensor for 5 turns CT (Table 17) and 3 turns CT, The error is calculated using equation 35.

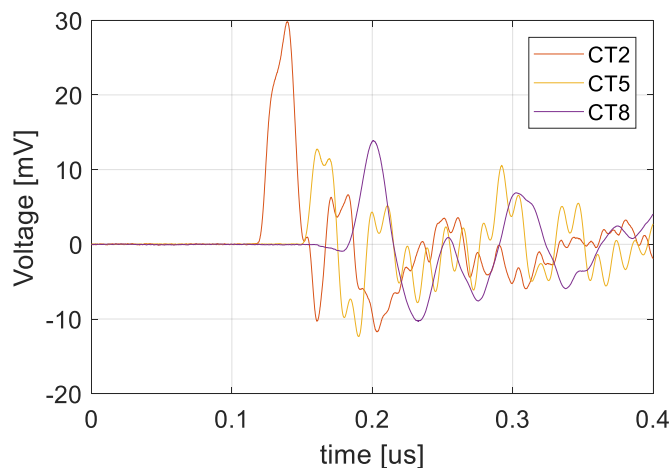


Figure 46. Pulse measured to calculate the charge of 40pC from calibrator

	Calibrator [pC]	Calculated [pC]	Error
Ch2	40	41.6	-4.0%
Ch5	40	52.9	-32.3%
Ch8	40	35.2	12.0%

Table 17. Calculated charge compared with a calibrator with a 5turns CT

	Calibrator [pC]	Calculated [pC]	Error
Ch2	40	31.7	20.75%
Ch5	40	58.1	-45.25%
Ch8	40	38.9	2.75%

Table 18. Calculated charge compared with a calibrator with a 3turns CT

For low frequencies the effect of G2 is no so critical, in the last calculation it had a value of 0.977, 0.963, .969; for CT 2, 5 and 8 respectively. In a different GIS, it might be difficult to calculate the inductances and capacitances in the bolt and spacer, so for low frequencies G2 can be ignored. The error in the calculations are mainly because of the reflections. It is too difficult to determine how the reflected pulses affect the incident pulse, the superposition of the pulses depends on their duration. The measured duration of the pulse is already the superposition of incident and reflected pulse. The CT5 in the bushing is the one with more indetermination, the calculated Z0 of the bushing is an average one, from a different pulse.

5.4.2. Discharge magnitude using frequency dependent Gain

As it was mentioned in section 3.1.4., by using a gain which varies with the frequency, a more real input pulse can be obtained. The calculated input pulse would be shorter and with more magnitude. In consequence, it would be less likely to have superposition with reflections and oscillations. Finally, the discrimination of the pulse with the zero crossing would be better. The charge is calculated using equation 58.

$$Q = \int_{t_0}^{t_1} \frac{V_{out}(t)}{G(\omega)} dt \quad [C] \quad 58$$

One of the problems with this method is that Gain in the DC component and high frequencies tends to zero and thus, the input current at these frequencies will tend to infinite after applying the gain. As an attempt to correct the problem the DC component was matched with the value of the lower measured frequency. And in the higher frequencies the gain was used with a value of 1. Using these assumptions, the calculation gave incorrect results. It is believed that is not possible to recover the input pulse. The measured wave is already distorted with the superposition of reflected pulses, in consequence, the original pulse is lost on it. In conclusion, it is preferred to calculate the charge using a constant gain, giving a more accurate charge value and reducing the calculating time.

5.5. Discharge location

With the information obtained in chapter 4 (speed propagation and reflection coefficients), it is possible to determine the location of the discharge source. The method for charge location is the time difference of arrival (TDoA), the method uses the minimum required sensors to get the best approximation.

Experiments were done to establish the most suitable location of the HFCT. With the simple assemble of the GIS in the HV lab, it is possible to determine the location of the defect with only 2 HFCT. For example, using CT2 and CT8, having the measurements in Figure 47. The only needed information from the measured pulses, is the time delay of the pulse, and its peak magnitude.

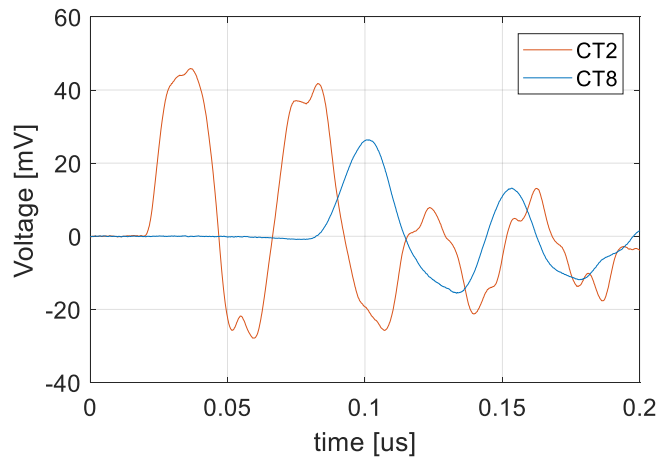


Figure 47. Measurements to detect defect location.

The peak magnitude of CT2 and CT8 is: 45.9 mV and 26.3 mV. This means that the pulse can only come from the left branch of the T joint. If it would come from the right branch the magnitude would be equal for both CT's and if it comes from the upper branch, CT2 would be lower. The polarity of the pulses also helps to determine where does the pulse comes from. If the polarity is different for each sensor, it means that the discharge comes somewhere in between the two sensors. If the polarity is the same, then it means that the source is in one endpoint of both sensors. There is a time difference between both pulses of 64 ns, using an average speed of 262 m/ μ s, the calculated distance is 16.8 meters. The measured distance between the CT's is about 16 meters. Hence, with this information is possible to determine that the pulse is coming from the left of the of CT2.

In long cables (1-2 km), by means of reflections, it is possible to know the location of the discharge with an accuracy of 5-10 meters [8], where the pulse is very small compared with the distance of the cable. In the case of the GIS substation, the pulse length is comparable with the time delay of reflections, therefore, it is not possible to calculate discharge position between the HFCT and an open circuit. The closer the HFCT is to the open circuit, the uncertainty of the pulse location is reduced, but also the HFCT signal magnitude is reduced. Therefore, we can guarantee that the pulse source is situated at the left of the CT2 in a 2.3 meters range. Is concluded that the most suitable location of the sensors is near an open circuit, but it is required to leave a distance with the dimensions of half the length of a pulse.

If the discharge is located in between the two HFCT's, it is possible to calculate a more approximated location of the discharge source. Let's suppose that the discharge is at a distance x from the nearest CT and the distance between both CT's is ℓ .

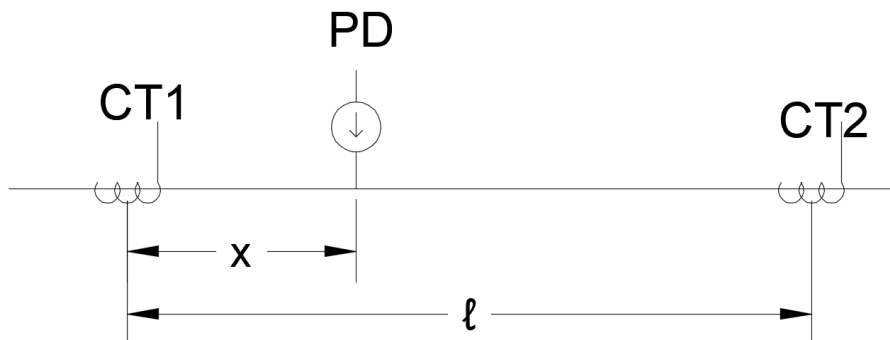


Figure 48. PD location between two CT's

The distance x is the product of the time (t_1) that takes the pulse to travel from PD to CT1 and the propagation speed V_p . The distance $x - \ell$ is the product of time (t_2) that takes the pulse to travel from PD to CT2 and the propagation speed V_p . And the measured time difference between both HFCTs is $\Delta t = t_2 - t_1$. Thus, we have three equations and three unknowns (x , t_1 , and t_2). The only variable of interest is x , consequently, it is found using equation 59.

$$x = \frac{\ell - V_p \Delta t}{2} [m]$$

Given the following example, in a hypothetical situation with the following measured data:

- CT4: 10 mV peak, 10 ns starting pulse.
- CT8: 15 mV peak, 25 ns starting pulse.

First, we know that the pulse is located at the upper branch of the T joint; the magnitude of CT8 is bigger than the one in CT4 (3/2 times bigger). The distance between the two CT's is 12 meters and the time lag difference is 15 ns. Consequently, the discharge is located at 4 meters from CT4. The precision of the location will depend on the Δt used, which depends on the interference and noise of the measurement.

The pulse location is important not only to determine the position of the source, but also, it defines the calculation of the magnitude. For instance, if the PD is located in a place where the pulse travels in both directions, the measured pulse will be half of the real one. On the other hand, if the PD is located near an open circuit, the measured pulse will be the same as the real one. This is illustrated in Figure 49. All the measurements done in the laboratory was in an endpoint of the GIS, so the pulse was not divided in two.

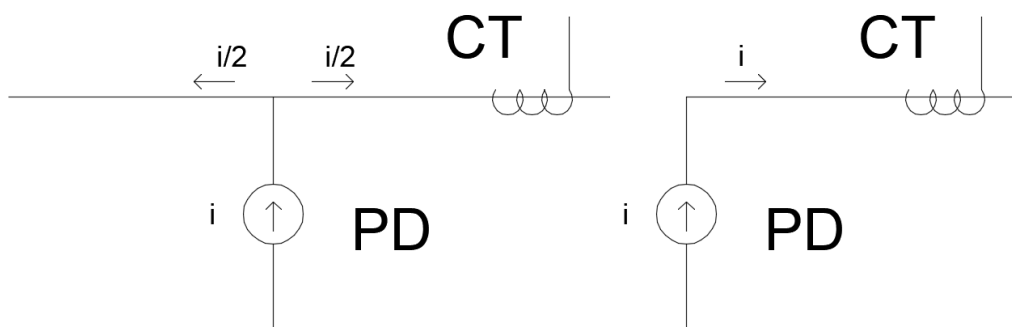


Figure 49. Importance of PD location for magnitude calculation

5.6. Chapter conclusions

Chapter 5 uses the information provided in the previous two chapters to establish an equation to calculate the pulses charge with the HFCT in the GIS. The interaction of the reflected primary impedance of the HFCT and the electric characteristic of the GIS, determines the distribution of the current in the GIS. Different situation where studied, such as many conductive bolts in the spacer, just one conductive bolt, and the use of bridges in the spacer. Although specific situations where studied in this section, it is possible to apply the same methodology for different configurations. For instance, different number of bolts in the flange, many bridges in the same flange. In fact, the spacers in the lately GIS come inside the enclosure, giving a different alternative for the CT placement, this involves different capacitances that can be included in the equation presented in the chapter.

Using a calibrator with known injected charges, the calculated discharges measured with the HFCT gave errors below 30% (except near the bushing). Therefore, the charge calculation accuracy is expected to have a tolerance of $\pm 30\%$. With the HFCT is possible to calculate the PD location with a minimum of 2 sensors. In the next chapter an attenuation comparison is made between the HFCT and the antennas.

6. Antenna measurement

The antennas are used to determine a defect location and the type of insulation defect, this two factors are affected with in attenuation of the signal. The goal of the chapter is to present the signal measured with antennas. These antennas are distributed in different sections of the GIS, so the attenuation and sensitivity of the antenna can be compared with the HFCT. The location of the antennas is indicated with the letter A and a number in Figure 28.

As it was explained in Chapter 2, a PD creates EM waves in three modes (TEM, TE and TM). For the TE and TM modes, the characteristic impedance depends in the frequency, giving different reflections for each frequency. Depending on the frequency, attenuation or amplification of the EM-waves are expected; amplifications could occur due to resonances [7]. Higher attenuations are expected in higher frequencies due to the capacitances and inductances of the system. For the defect location, measurements in the time domain are used to obtain the time lag between antennas, using the TDoA technique. In the type of defect determination, the signal is analyzed in the frequency domain and with the phase-resolved PD pattern. Because the signal at high frequencies is weak, resonances at high frequencies are used in the post-processing.

A generic pulse generator of 1 ns rise time and 2 Volts peak amplitude (Device 5) was injected at the entrance of the GIS. The 1 nanosecond rise time pulse was chosen to simulate very fast pulses, which are expected in a PD in SF₆. The antennas were connected directly to the oscilloscope; without any amplifier, filter or surge arrester which could decrease the bandwidth. To compare the sensitivity and attenuation of the antenna with the HFCT, the peaks of the pulses are used. Table 19 shows the voltage peak values for UHFS and HFCT and their comparison. In the first meters, there is already a strong difference in the sensitivity between sensors; the HFCT is almost 5 times bigger than the Antenna.

Location	Antenna [mV]	HFCT [mV]	Relation HFCT/UHFS
2	9.6	45.9	4.8
3	4.9	45.7	9.3
4	6.2	49.5	8.0
5	3.6	22.4	6.2
6	2.0	25.5	12.8
7	0.6	25.9	43.2
8	2.0	26.3	13.2

Table 19. Sensitivity comparison between the UHFS and the HFCT

6.1. Attenuation

The attenuation is a reduction of the amplitude strength when it propagates in a medium. The attenuation compares the input and output in a system. The attenuation is commonly measured in dB which is 10 (for power) or 20 (for voltage) times the logarithm of the out/input ratio signal (equation 60).

$$A = 20 \log \frac{f(t)_o}{f(t)_i} [dB] \quad 60$$

According to [19], for TEM propagation, preliminary tests proved that a 100 m long straight line composed of a central conductor and the enclosure, does not distort or damp a propagated pulse. On the other hand, other components are damped in the TEM such as spacers, T and L joints. The attenuation of the signal will depend on the frequency. Results of attenuations, for different frequencies in a spacer, a T and a L joint are shown in Figure 50 and respectively.

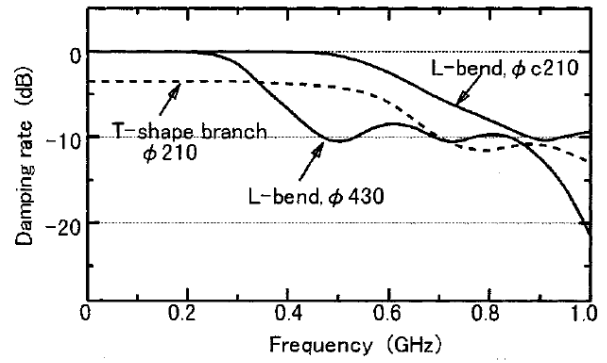
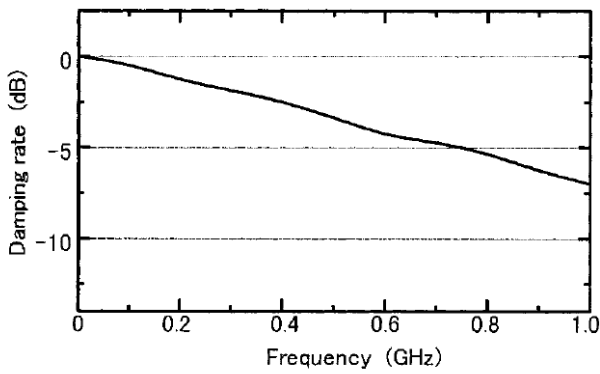


Figure 50. Frequency attenuation of a spacer (left) and T and L section (right) [19].

The T-shape section starts in -3.5dB; as it was mentioned before, the GIS is divided in two branches, which is the same as the two circuits in parallel. Using equation 60, the refracted value is 2/3 which is -3.5 dB.

The attenuation comparison between the sensors is made in each different section. The attenuation is calculated using equation 60, where $f(t)_o$ is the signal after the section and $f(t)_i$ is the signal before the section. The results are presented from Table 20 to Table 23.

Section	Antenna Attenuation	HFCT Attenuation
2 spacers at 2.5 meters distance.	-5.8 dB	0.0 dB

Table 20. Attenuation comparison in 2 spacers and 2.5 m distance

Section	Antenna Attenuation	HFCT Attenuation
2 spacers, 1 T division and a bushing at 4.4 meters distance	-4.7 dB	-6.9 dB

Table 21. Attenuation comparison in 2 spacers, 1 T division and a bushing at 4.4 m distance

Section	Antenna Attenuation	HFCT Attenuation
2 spacers, 1 T division, 1 L section at 4.3 meters distance	-9.8 dB	-5.8 dB

Table 22. Attenuation comparison in 2 spacers, 1 T division, 1 L section at 4.3 m distance

Section	Antenna Attenuation	HFCT Attenuation
2 spacers, 1 switch at 2.2 meters distance	-10.5 dB	-0.1 dB

Table 23. Attenuation comparison in 2 spacers, 1 switch at 2.2 m distance

According to Figure 50, there is a high attenuation for the antennas when the signal goes through spacers, L and T sections. In the case of the bushing the HFCT senses a higher attenuation, the reason could be that the bushing is almost an open circuit for the TEM mode. On the other hand, the TE and TM radiates and don't need a conductive path.

When the switch is closed the attenuation in the HFCT is negligible; for the antenna is almost -10 dB. If the switch is open, then it is an open circuit and no current flows anymore, so only the antenna can sense the radiation.

6.2. Chapter conclusions

The antennas use TE and TM modes, this are more affected by attenuations in higher frequencies. For GIS application, it is concluded that the HFCT has better sensitivity and less attenuation that the UHFS. The UHFS have attenuation in every section of the GIS; pipe long distances, spacers, T sections, L sections, switches, CB. The advantage of the UHFS over the HFCT is that the TEM mode divides in the number of conductive paths and also cannot propagate in a nonconductive medium. The HFCT measuring method shows attenuation in two situations; when the GIS has an intersection of many electric paths (T section), and when the conduction path is discontinuous (bushings and open switches/CB).

With the information of the attenuation in each section is possible to establish the minimum number of sensors to cover all the GIS substation and predict the location of the PD. More UHFS are required to measured and locate the PD in different locations in comparison with HFCTs.

In previous chapters and including this one, different measurements and simulations were done to estimate different parameters of the HFCT in a GIS. All the measurements were done by injecting pulses from a pulse generation. The next chapter presents the measurements from real PDs in a GIS situation.

7. PD Measurements in GIS

The goal of this chapter is to measure real PDs in the GIS. The main objective of the HFCT measuring method is for HVDC GIS application, however it might be extended to HVAC GIS. The tests are performed using an AC voltage because of the advantage of having greater amount of discharges in a short period, compared to a DC voltage. It is believed that results are valid for DC and AC voltages, the breakdown mechanism does not change.

The measurements are done with the HFCT and UHFS, to compare them. Also, an approximation of the PD is done by means of the calibration procedure. This chapter covers the setup made for different PD measurements. Thus, the equipment used to create and sense the PD are covered, such as: amplifiers, filters, oscilloscope, voltage source, artificial defects, etc.

The data is analyzed using the software PDFlex. In this software, the charge is calculated using the same method presented before. The incident pulse is isolated and integrated over time to find the charge. The results given by the software are calculated using the gains of the sensors and the amplifiers. Therefore, the presented results of the pulses are the calculated ones, not the measured at the oscilloscope.

7.1. PD measurement setup

In Figure 51, the GIS figure is simplified, the real GIS composition is presented in Figure 28. Some of the elements are explained with more detail in the same chapter. The setup is composed of the high voltage part, and the sensing system. The HV part includes the elements which are subjected to power frequency voltage. In the measuring system, only the elements necessary to measure the PD are mentioned.

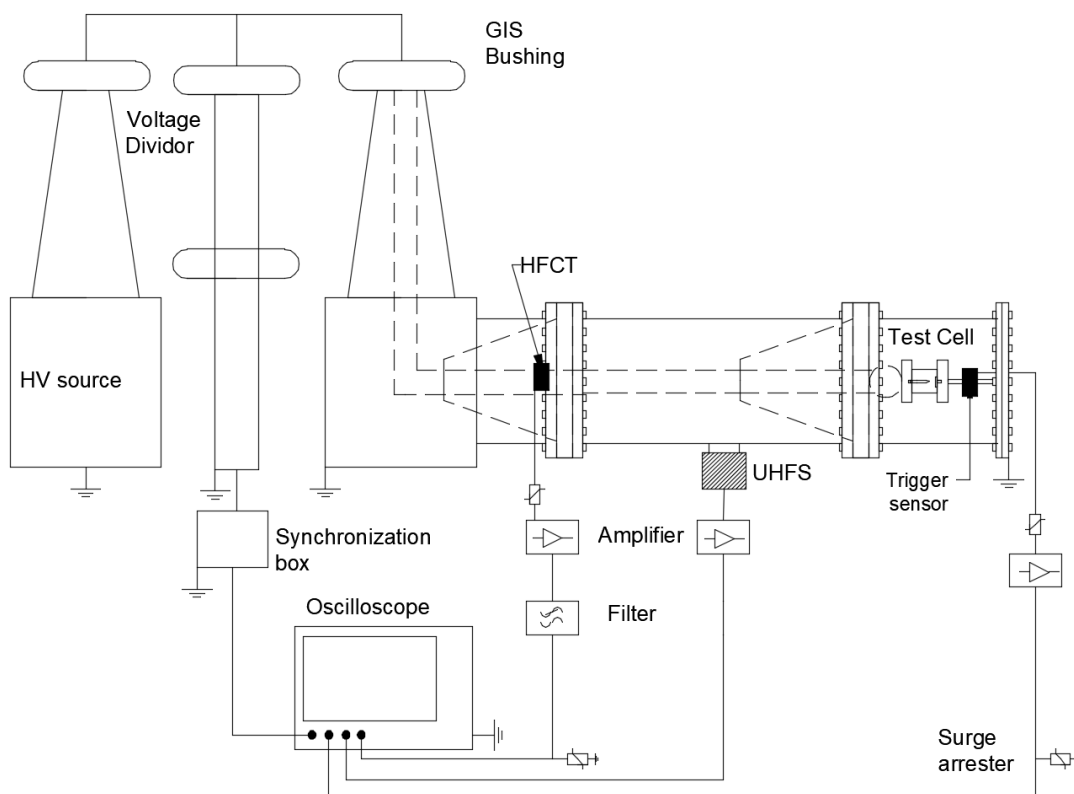


Figure 51. Setup drawing for the creation and measurement of PD.

7.1.1. High Voltage section

The HV comes from a regulating transformer which feeds the GIS through the bushing. The HV is measured with a capacitor voltage divider, located between the HV transformer and the bushing. At the termination of the inner conductor, a test cell is installed. The test cell is connected between the inner conductor and the enclosure by a shaft (Figure 52, left), making a better contact. For the case of the moving particle test cell, the cell was connected vertically by means of wires; the cell requires a vertical position due to the gravity influence to the discharge mechanism (Figure 52, right).



Figure 52. Installation of the test cell in the GIS

Test cell: From the entrance of the GIS to the third spacer (Figure 28), the GIS contains 1 atm pressure air. To simulate a real GIS situation, the defects must be placed in SF₆ at a nominal pressure. To place a defect directly inside the GIS, it is necessary to pressurize and depressurize it for each test. This takes a lot of time and a risk of SF₆ leakage is present. To avoid the GIS pressurization problem, a test cell was designed. This test cell is a sealed chamber where the defect is placed, then, the chamber is pressurized with SF₆. A rated pressure of 4 bar is used inside the test cell [6]. Another advantage of the test cell is that the type of defect can be verified using an IEC 60270 detection setup. Different chambers were made for each type of defect. In this thesis only 3 out of the 5 discharges introduced in this document are created. Although the 5 types of discharges were attempted to be tested the surface discharge and floating electrode were not possible to be measured in the GIS. The tests in the GIS were limited for protection reasons; no voltage higher than 20 kV was allowed due to the sections of the GIS where SF₆ was not presented, and no breakdowns in the test cell were permitted to not risk the GIS and HV transformer with a short circuit current. Consequently, only measurements for corona, moving particle and internal discharge were tested.

7.1.2. Measuring system

The PD signal is measured by a triggering sensor (TS), and the HFCT and UHFS installed along the GIS. The HFCTs and UHFSs are connected to an amplifier and then to the oscilloscope channel. To obtain PRPD, the 50/60 Hz signal is required, for that, a synchronization unit (SU) is connected from the voltage divider to an input of the oscilloscope. All the sensors are connected from the GIS to the oscilloscope with a 50 Ω, RG58, 15 meters coaxial cable. Surge arresters are connected in parallel with the oscilloscope to protect it from high peak voltages coming from the HFCT.

Triggering sensor: The shaft which connects the test cell and the enclosure, goes through the triggering sensor. The sensor is installed inside the GIS, so it is shielded against interferences. The secondary of the HFCT is connected to a coaxial cable that transport the signal coaxially outside the GIS. The trigger of the oscilloscope is made through this sensor because is the signal with highest amplitude and less interference.

Synchronization unit: The SU generates a sawtooth wave in phase with the 50/60 Hz voltage signal (Figure 53). The wave is triggered with the positive zero crossing of the power frequency voltage. The ramp has a steady slope of $\Delta V/\Phi=4.54$ V. At the instant when a PD occurs, the value of the sawtooth signal is recorded. Each value of the ramp corresponds to a different phase of the power frequency sinusoidal wave [20].

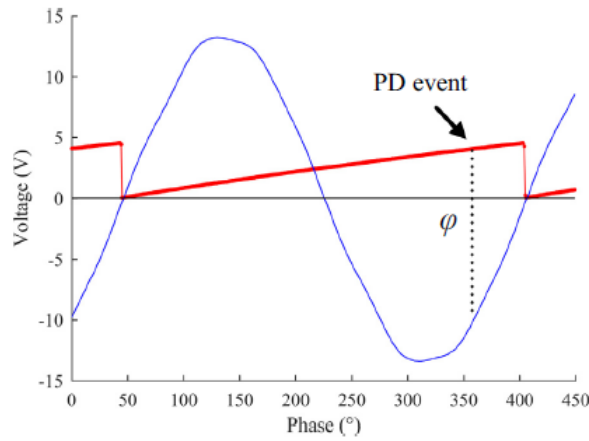


Figure 53. Sawtooth wave generated by the SU

Amplifier: The created PDs are in the range of pC, these values are represented in voltage pulses in the range few mV or even hundreds of μV . The oscilloscope is not able to detect voltages with that magnitude. Then, an amplifier is necessary to increase the signal, to a measurable one. The amplifier will boost not only the signal of interest but also the noise and interferences; therefore, a filter is necessary to focus only in the signal of interest. The gain of the amplifier is frequency dependent, so it will act as a filter for certain frequencies. The antenna gain is lower compared to the HFCT, thus the amplifiers used in the UHFS have bigger gain. The amplifiers bandwidth must be in the range of the sensor's BD. The amplifier for the antenna must have BD from hundreds of MHz to some GHz, the CT's BD must be a band pass amplifier in the range of tens of kHz to hundreds of MHz.

Filter: Any circuit with resistance will have thermal (white) noise, the noise power in every frequency is the same. The RMS noise voltage is $V_{n,rms} \propto \sqrt{B}$, where B is the band-width. Another not desirable signal is the interference. The GIS is a big metallic structure; thus, it acts as a big antenna, picking up magnetic interference (MI), electric interference (EI) and electromagnetic interference (EMI). EI and MI are mainly in the power frequency and come from the power current and voltage. The EMI could make an appearance in any frequency and are mainly caused by electronic switching. The objective of the filter is to reduce the bandwidth of the measuring system to the minimum range where the signal of interest exists.

The antenna does not need the filter for the experiments, the amplifier already acts as a high pass filter eliminating low frequency noise and interference. The antenna senses only high frequencies so is not wise to reject high frequencies with a low pass filter. Finally, the HFCTs in the bolts could use a filter, the flat gain in the transfer function of the HFCT is in a bandwidth from tenths of kHz to tenths of MHz's. Therefore, it may not be required to have bandwidth outside this range. However, by cutting the high frequencies, the sensed pulses become with less magnitude but with higher duration, this will reduce the SNR, and the reflected pulses may overlap.

Surge arrester (SA): The oscilloscope is protected with a surge arrester. In case of a signal with a voltage higher than the withstand voltage of the oscilloscope ($5V_{rms}$), the SA acts as a short circuit and the voltage drops to zero. Two different SA are connected for pulses of different frequencies. The SA acts as a low frequency filter, so it is not used for the antennas to avoid attenuation of it. An extra SA is used for the case of the moving particle, this SA is located before the amplifier and filter to protect them. This SA is required with more power; therefore, its capacitance is higher. The capacitance of the SA is represented in parallel with the load; thus, the transfer function of the HFCT might change.

7.2. Corona PD

Occurs in sharp points in one of the electrodes. The sharp point can occur in either high-voltage or ground electrode. Due to the electric field enhancement due to the charge accumulation in a sharp edge, a partial breakdown occurs. The inception of negative corona under alternate current (AC) and direct current (DC) voltage occur at a similar voltage level. The starting electron is originated by field emission from the cathode, this happens for any gas. In SF_6 , the positive corona has a different behavior; the starting electron is generally originated away from the sharp point, by photo-ionization mechanism [9]. The corona defect can appear in

the GIS when either the enclosure or inner conductor are scratched during the installation and a protusion in the aluminium is created.

Corona discharge is simulated by using a thread needle as the sharp electrode. It is estimated that the point radius of the needle is about 50µm. The distance between electrode is 1.2 cm (Figure 54). The electrode sharpness and the electrodes distance are selected not to treat the security of the GIS. A small distance between electrodes is more likely for a total breakdown to happen. Big distance on the other hand, requires higher voltage to create corona, thus, putting in the danger the spacers of the GIS where there is no SF₆. Also, a rounded point creates bigger discharges, which are easier to detect, however, a higher voltage is required.

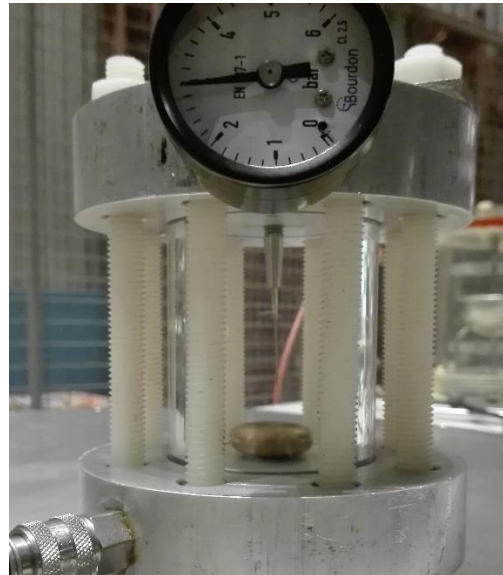
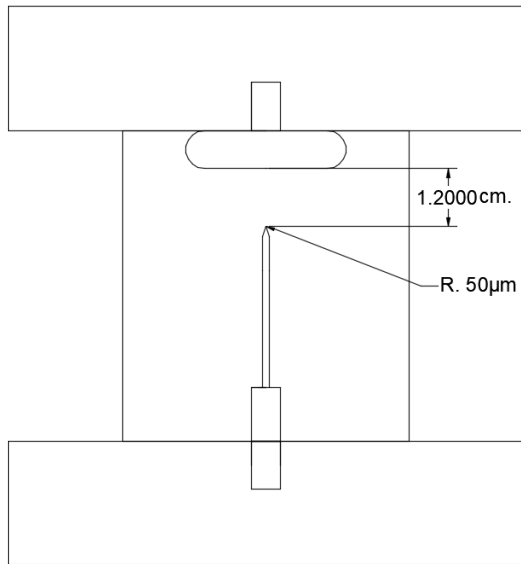


Figure 54. Sketch and photo of the corona test cell (left and right respectively)

Previously to the experiments in the GIS, the chamber was tested using IEC 60270 detection. By this means, the gap distance and the sharp radius was selected to achieve an appropriate inception voltage. Also, the magnitude of the discharges was measured. However, it is not expected to have the same magnitude of discharges in the GIS; it is a different circuit, and the discharges are an stochastic process where the magnitude varies.

The main goal of the test is compare the measurements between the antennas and the HFCT. The antenna and 3 turns CTs where tested at the same time, this means, the same pulses where measured by both sensors. Furthermore, it is also of interest the behavior of the CT with different number of turns. It is not possible to place the different CT in the same position to compare them. Therefore, in a different measurement, but using the same set-up and parameters, tests were done with a 5 turn CT.

The results of the PD in the IEC 60270 detection are shown in Table 24, using SF₆ at 4 bars.

Voltage [kV]	PD magnitude [pC]	Type of corona
10 kV	1.5	Negative
15 kV	5	Positive

Table 24. measured PD's in the IEC 60270 detection

For the tests in the GIS, the following configurations where used (the oscilloscope has internal filters, different bandwidth was used depending of the sensor connected):

Voltage source: 15 kV, 50 Hz.

Test-cell: corona discharge, SF₆-4 bar, 12 mm gap distance, 50 µm protrusion radio.

Oscilloscope: (Device 3), 3.125 GS/s, 1000 pulses per channel, 1 μ s window, 250 MHz filter for CT's, 1.5 GHz filter for Antenna.

CT 1: TS, 3 turns HFCT, 25 dB 500 MHz amplifier.

CT 2: 3/5 turns HFCT, 25 dB 500 MHz amplifier.

CT 4: 3 turns HFCT, 5 kHz high pass filter.

CT 8: 3/5 turns HFCT, 25 dB 500 MHz amplifier.

A2: Antenna, 30 dB 1.7MHz-1.36 GHz amplifier.

A8: Antenna, 30 dB 1.7MHz-1.36 GHz amplifier.

Coaxial cable: 50 Ω , RG58, 15 meters

7.2.1. Corona PRPD pattern

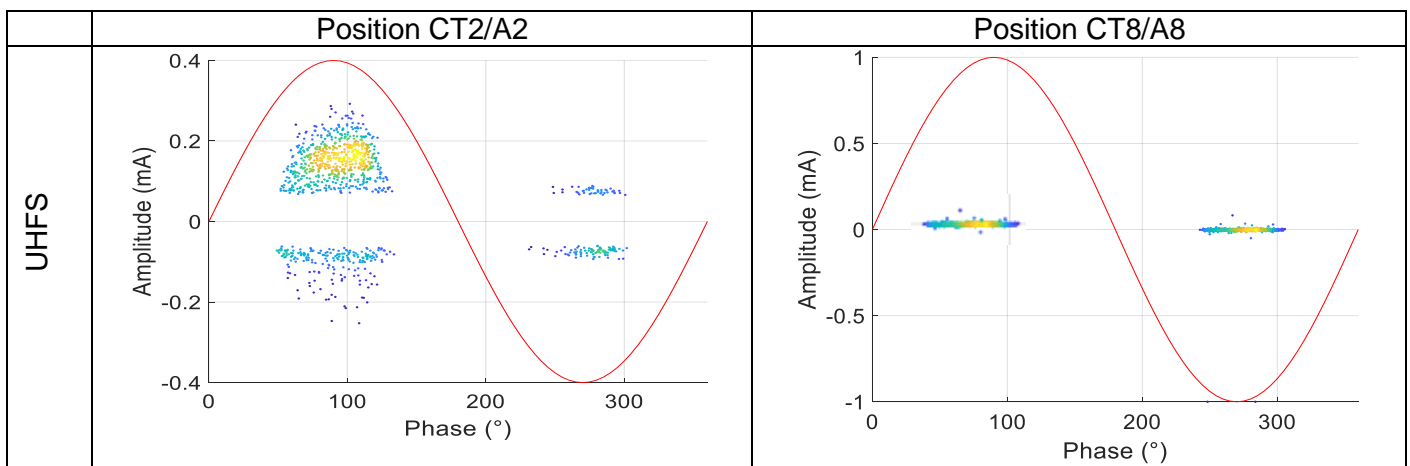
In Figure 55 the PRPD pattern is plotted. A comparison between UHFS (first row), 3 turn HFCT (second row) and 5 turn HFCT (third row) is made for two different locations. For the antenna does not make sense to talk about the charge value. Nevertheless, is useful to have a representation to identify positive and negative corona.

First, the negative corona appeared at 10 kV, the magnitude of the discharge is maintained with the increased voltage. After a voltage threshold, positive corona appears, with a higher magnitude. The positive corona PD increases its value as the voltage increases. Another characteristic of a corona discharge is that they are concentrated in the crest of the sinusoidal wave.

In some of the measurements, both polarities appear in the positive and negative half-cycle. This is because in some cases, the measured pulse was smaller than the background interference, therefore, the computed pulse is a noise wave. In the A2 for negative corona, is not possible to identify between real PDs and noise/interference in the negative PDs. In the PRPD of A8, the measured signal is only background noise, there is no trail of the PD. It exists the possibility that there were more negative corona PD's, but because of their lower magnitude the oscilloscope may not be triggered.

A clearer PRPD image is obtained with the HFCTs than the UHFSs, this is a consequence of a better SNR and sensitivity. Comparing between the 3 and 5 turns is observed that the 5 turn PRPD has better precision (less deviation). Also, the 5 turns CT measured charges are more approximated to the measured ones in the IEC 60270 detection, therefore it appears to have a better accuracy.

The colors in graphs represent the charge density, where blue is the lowest density and yellow the highest.



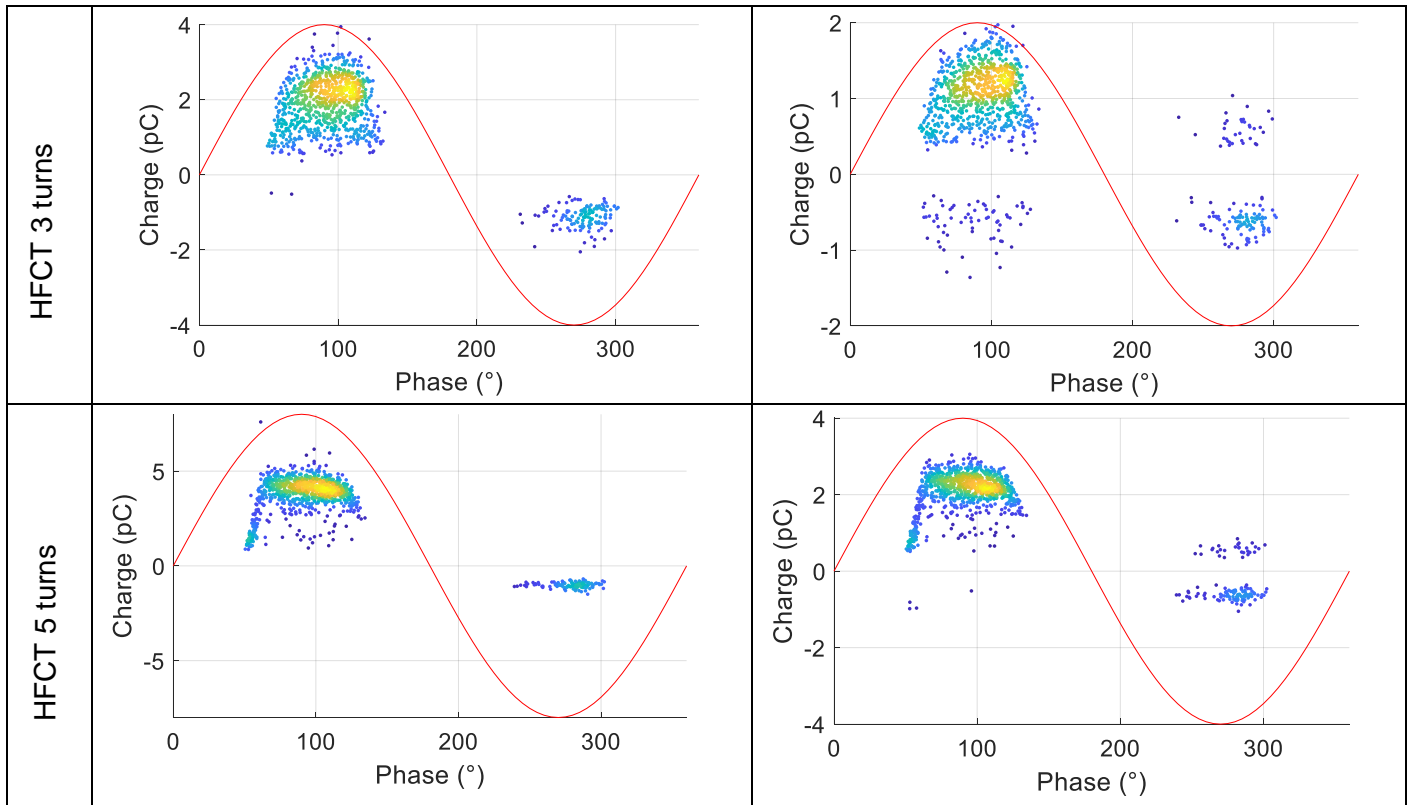


Figure 55. Corona PRPD pattern for HFCT and UHFS in different positions

The charge was evaluated from a pulse corresponding to the yellow area. By inspection of the charge, it is deduced that for the CT2 and CT4, the measured pulse is the superposition of the incident pulse and the 1/3 reflected pulse in the T joint. The measured pulse in the CT8 is the 2/3 refracted pulse from the T joint. In Table 25, the second column with the name “Apparent PD” represents the measured discharges. The third column, named “calculated PD” is the calculated charge applying the reflection coefficients.

The calculated charge goes below the measured one in the IEC 60270 detection. The reason might be the different charge calculation method by means of resonance in the IEC 60270 detection. Also, the equivalent electric circuit of the set-up of the IEC 60270 detection is different than the GIS set-up, this shapes differently the analyzed pulse.

Sensor	Apparent PD [pC]	Calculated PD [pC]
CT2	2.19	1.64
CT4	2.30	1.73
CT8	1.20	1.80

Table 25. Measured charge for an PD in each 3 turns HFCT

Sensor	Apparent PD [pC]	Calculated PD [pC]
CT2	4.30	3.22
CT8	2.22	3.33

Table 26. Measured charge for an PD in each 5 turns HFCT

Because of the reflections and resonances in the GIS, the calculated PD might not be the exact discharge value. The discrimination method for the pulse area calculation is by means of the zero crossing of the triggered pulse. In Figure 56, in the left plot, the selected pulse for area calculation is correctly discriminated from the rest of the pulses. The right plot in the figure, is another pulse measured with 3 turns HFCT, the discriminated pulse is the superposition of the incident pulse and a reflected one. The duration of the pulse affects the correct discrimination of the pulse. As it was seen in Chapter 3, section 3.1.4., the use of a constant frequency affects the duration of the pulse, using a HFCT with a longer range of flat gain (more number of turns) may help to avoid this error. The measured pulse duration (zero crossings) are in the order of 35 ns

and 27 ns for a 3 turn and 5 turn CT respectively. With the 5 turns measurement there was not an overlapping detected.

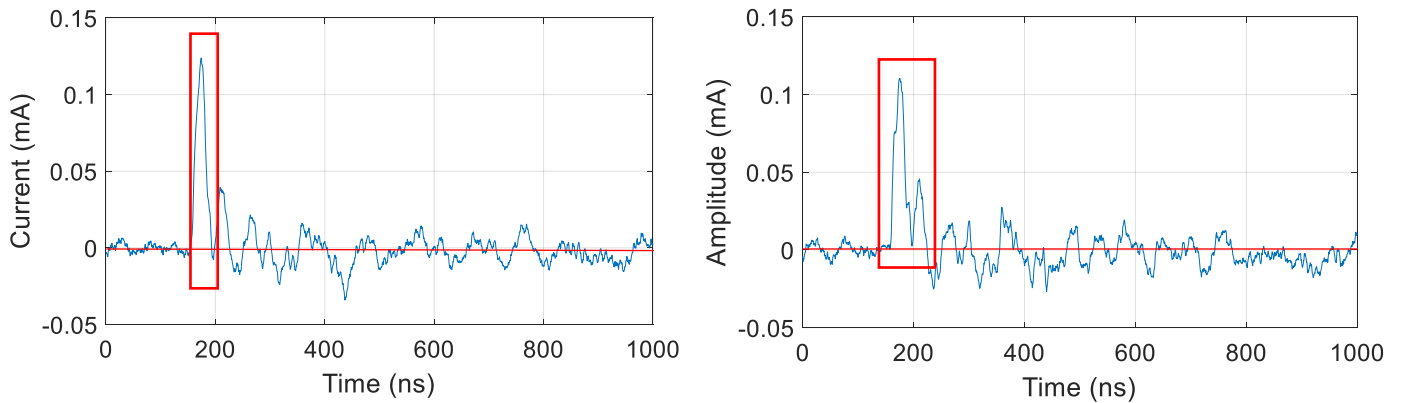


Figure 56. Correct (left) and incorrect (right) pulse discrimination for corona discharge in a 3 turns HFCT

7.2.2. Corona SNR

The SNR is calculated for each sensor, for positive and negative PD. The discharge selected for the calculation is one in the yellow area (where most of the discharges are located). To calculate the SNR equation 26 is used. The noise used for the calculation, is the measured wave before the trigger. The signal used for the calculation is the first pulse after the trigger. In Table 27, the SNR in each sensor for positive and negative PD's is presented.

	Positive Corona SNR [dB]	Negative Corona SNR [dB]
A2	8.93	3.95
CT2-3 turns	24.60	14.02
CT2-5 turns	33.38	19.25
A8	0	0
CT8-3 turns	16.26	6.04
CT8-5 turns	28.37	9.37

Table 27. SNR for positive and negative corona

The relation of a HFCT and a UHFS in the same position near the PD source, is approximately 6 and 3 times bigger for positive and negative PDs respectively. For the sensors located farther, the attenuation is more noticeable in the antenna; the antenna is not capable or reading the PD neither for positive nor negative discharge. The HFCT is attenuated because of the T joint, the distance does not significantly affect it.

It was not expected but the 5 turns HFCT shows a better SNR than the 3 turns HFCT. This means that the main noise and interference comes from the primary circuit of the CT. Therefore, the bigger gain of the 3 turn CT, increases the amplitude of the signal of interest, as well as the noise and interference. In this case the 5 turns-CT SNR ratio was larger.

7.2.3. Amplifier and filter outcome

CT2 and CT4 shows a similar pulse measurement, therefore, some test were made to compare the difference of the measurements with/without amplifiers and filters. In Figure 57, a comparison between the CT2 with amplifier (25 dB 20 kHz-500 MHz) and CT4 with high-pass filter (5 kHz), in the time domain (first row) and in the frequency domain (second row) was made. The amplifier increases the gain of the signal in a certain frequency range, so it acts as a band-pass filter. According to specification, it has cut-off frequencies of 20 kHz to 500 MHz. Therefore, the high frequencies are rejected by the amplifier. As a result, the noise is reduced and the signal in the CT2 is neater than in the CT4.

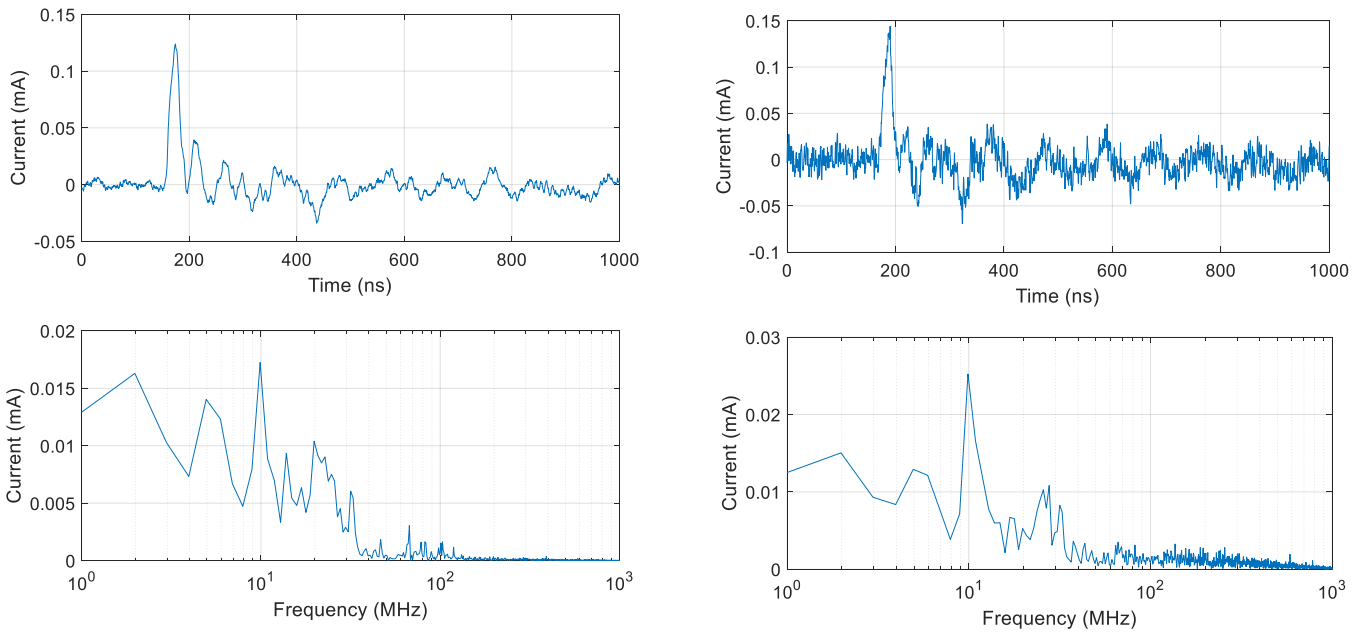


Figure 57. CT2 with amplifier (left) and CT4 with high pass filter (right) comparison.

It is concluded from the previous test that a better signal is obtained with a filter, however, is not clear about the amplification. Another test was carried out, where both CT's used the same filters with a BW of 5 kHz-50 MHz but CT2 with an amplifier (25 dB, 20 kHz-500 MHz) and CT4 without. To determine the necessity of the amplifier a small detected pulse was selected, thus, a negative corona discharge of 1.1 pC (Figure 58).

According to the results, the best signal is obtained with the amplifier and the band-pass filter. Nonetheless, an amplifier requires an external power source. For the tests, the amplifiers used were battery powered since the use of a power supply from the electric grid, injects interference to the measurements. However, is not practical to use battery supplied amplifiers, the batteries must be changed over a short period.

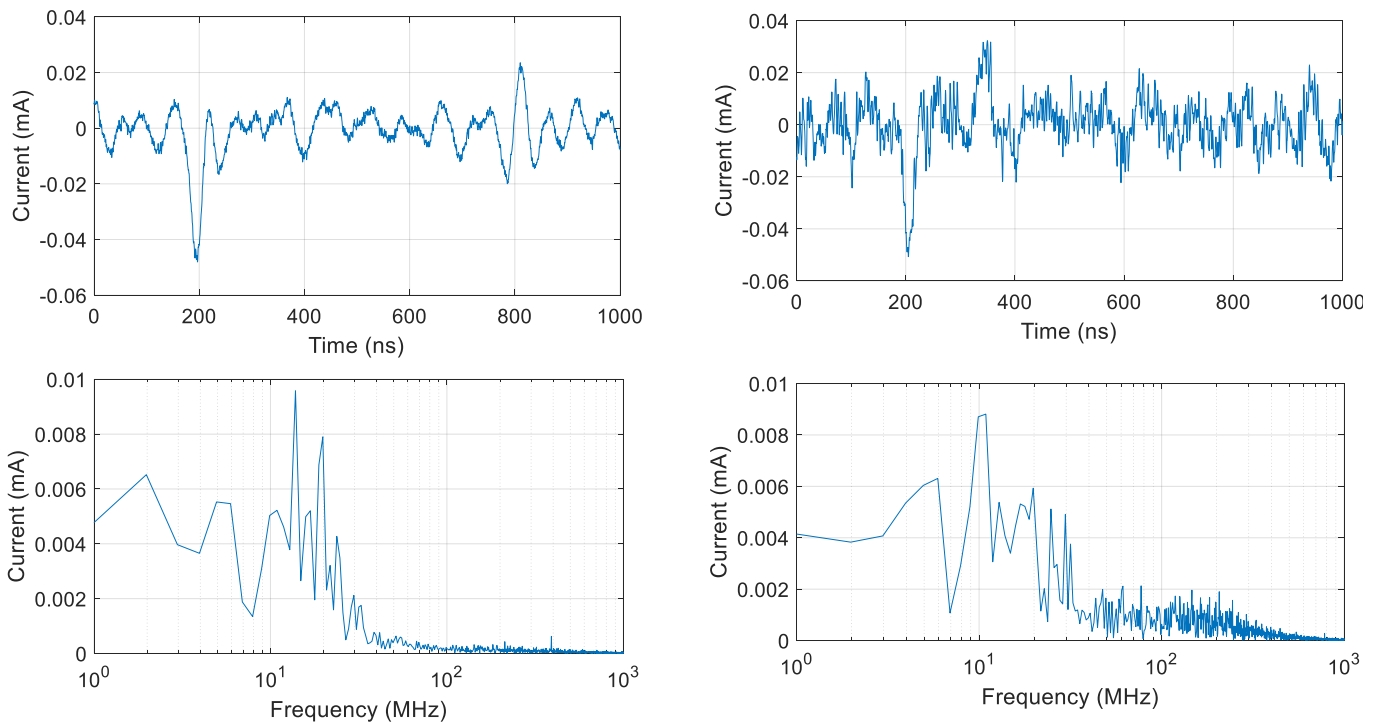


Figure 58. CT2 with amplifier and filter (left) and CT4 with filter (right) comparison.

7.3. Moving particle discharge

In resting position, a free moving particle is in contact with the grounded electrode (enclosure). With the energization of the GIS it acquires an induced charge, which creates an interaction with the external electric field and exerts a Coulomb force on it. This particle is subjected to Coulombs force drag and gravity force, accelerating the particle in the direction of the resultant force. The particle accelerates towards the electrode discharging itself and returning back to the grounded electrode. Sometimes during installation, some conductive particles can be left inside the GIS, such as metallic shavings

A Moving particle discharge was simulated using a dry ice ball covered with aluminium foil. The approximated weight of the particle is 3 mg with a diameter of 6.6 mm. The particle is rested in a concave brass electrode. The HV electrode consist of a 16 mm sphere, separated 13 mm from the grounded electrode (Figure 59). In theory [9], the gas in the chamber should not change the mechanism of the discharge; it depends in the ejected forces (gravity, drag and electric force) to the particle. However, the chamber was filled with 4 bar SF₆ to simulate a more real GIS situation and avoid any other type of discharge.

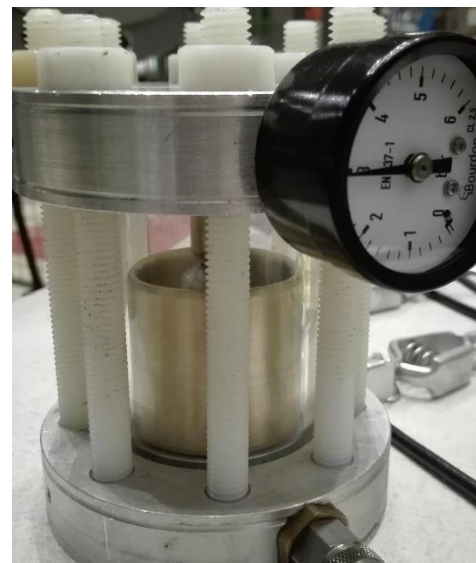
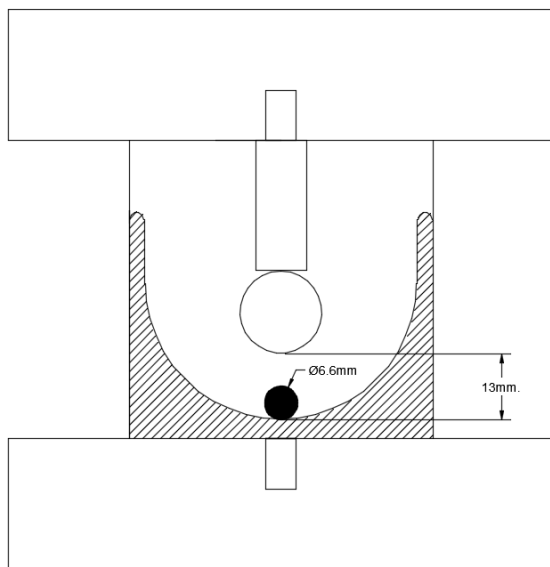


Figure 59. Sketch and photo of the moving particle test cell (left and right respectively)

The results of the PD in the IEC 60270 detection are shown in Table 28, using SF₆ at 4 bars.

Voltage [kV]	PD magnitude [pC]
15 kV	30

Table 28. measured moving particle PD's in the IEC 60270 detection

For the tests in the GIS the following configurations where use:

Voltage source: 14 kV, 50 Hz.

Test-cell: corona discharge, SF₆, 4 bar, 13 mm gap distance, 6.6 mm particle diameter.

Oscilloscope: (Device 3), 3.125 GS/s, 1000 pulses per channel, 1µs window, 250 MHz filter for CT's, 1.5 GHz filter for Antenna.

CT 1: TS, 3 turns HFCT.

CT 2: 3/5 turns HFCT, surge arrester.

CT 8: 3/5 turns HFCT, surge arrester.

A2: Antenna, 30 dB 1.7 MHz-1.36 GHz amplifier.

A8: Antenna, 30 dB 1.7 MHz-1.36 GHz amplifier.

Coaxial cable: 50 Ω, RG58, 15 meters.

7.3.1. Moving particle discharge PRPD pattern

In Figure 60 the PRPD pattern is plotted. A comparison between UHFS (first row), 3 turn HFCT (second row) and 5 turn HFCT (third row) is made for two different locations. The plots show the typical PRPD pattern of a moving particle. The particle moves in a random way, the PD pattern in AC is the envelope of the sinusoidal voltage [9].

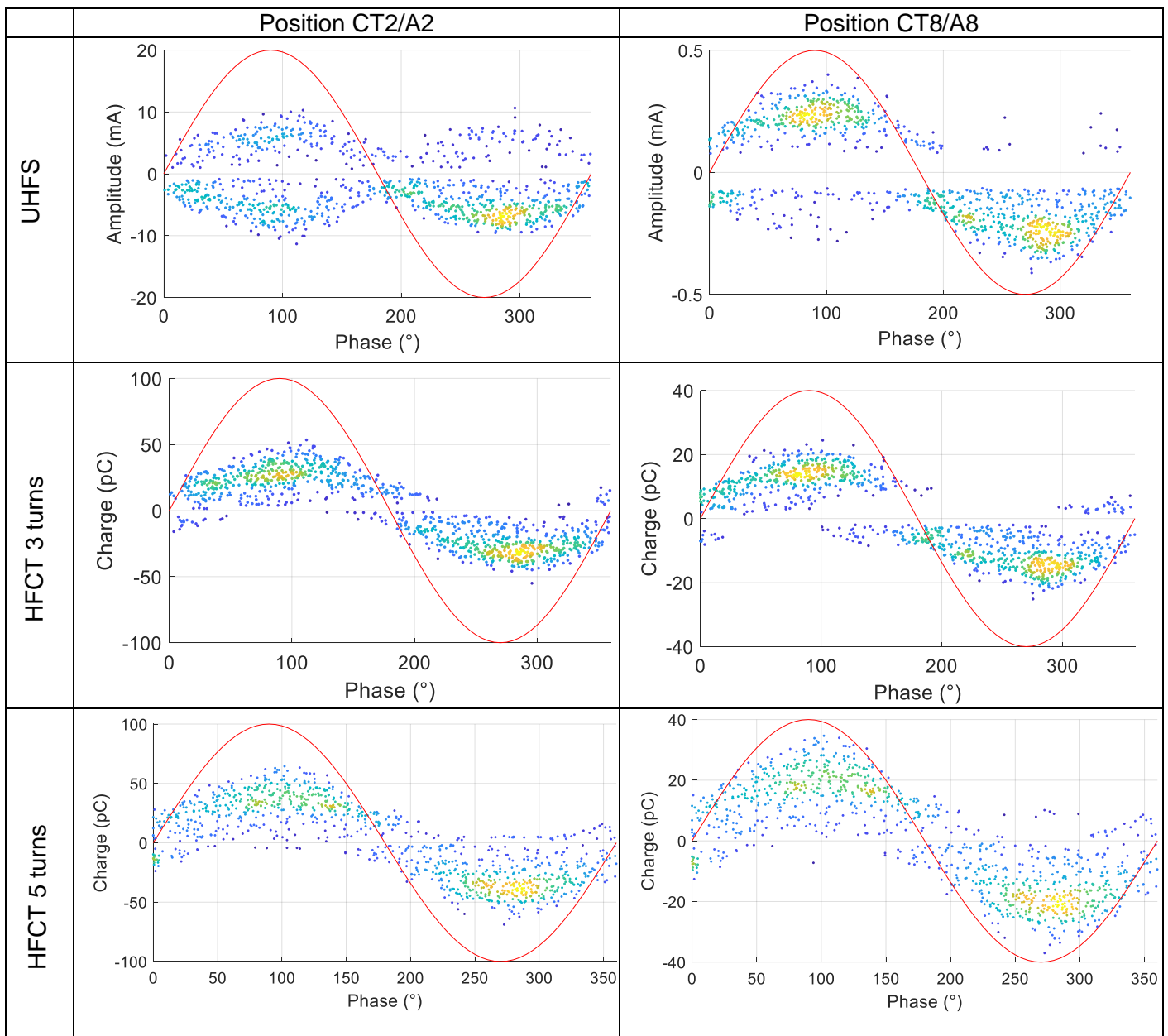


Figure 60. MPD PRPD pattern for HFCT and UHFS in different positions

Following the procedure used to calculate the charge in corona, Table 29 and Table 30 shows the results for the “apparent” and “calculated” PD using 3 and 5 turns CT respectively. For the MPD, the calculated results are values more approximated with the obtained ones in the IEC 60270 detection. Still the 5-turn CT shows a closer value to the one obtained in the IEC 60270 detection method.

Sensor	Apparent PD [pC]	Calculated PD [pC]
CT2	31.6	23.7
CT8	15.2	22.8

Table 29. Measured charge for an PD in each 3 turn HFCT for MPD

Sensor	Apparent PD [pC]	Calculated PD [pC]
CT2	31.6	30
CT8	15.2	29.0

Table 30. Measured charge for an PD in each 5 turn HFCT for MPD

In MPD the measured pulses had a shorter duration than in the corona discharge. In these dischargers there were no noticeable pulses superposition, this might be the reason of a similar charge magnitude with the IEC 60270 PD detection. Figure 61 shows the pulse discrimination from a random pulse in CT2.

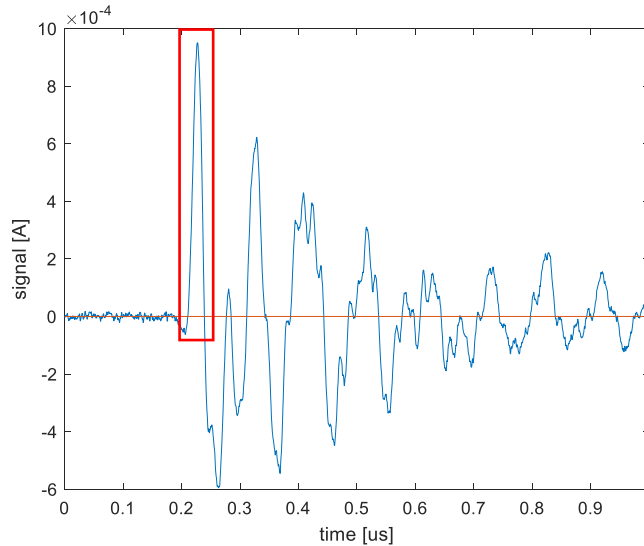


Figure 61. Pulse discrimination in MPD

7.3.2. Moving particle discharge SNR

The same procedure as in corona is used for MPD. In Table 31, the SNR in each sensor is presented. Better results occurred in this type of discharge. The obvious reason is because of the greater magnitude discharges; the setup does not change, so the noise and interference stay with the same magnitude as in corona, but the signal of interest is increased. In this case the 3-turn shows a higher SNR, as it was expected; it was a higher gain, consequently a higher SNR.

	MPD SNR [dB]
A2	25.38
CT2-3 turns	41.20
CT2-5 turns	37.79
A8	17.83
CT8-3 turns	37.99
CT8-5 turns	35.11

Table 31. SNR for MPD

7.4. Internal Discharges

Internal discharges occur in a gas-filled cavity in a solid dielectric. The difference in permittivity between the solid and gas dielectric, creates a field enhancement in the dielectric with lower permittivity (usually the gas). When the electric field is high enough to create a breakdown, the accumulated electrons in the cavity are emitted and a breakdown occurs. The process is repeated until the electric field produced by the voltage source (sinusoidal 50/60Hz or DC source) is equal to the electric field of the accumulated electrons in the cavity. In the case of the GIS, the internal discharge can occur when there are cavities in the solid insulation, e.g. bubbles introduced in the spacer or bushing in the production process.

To simulate an internal discharge, a different test cell was constructed. In an internal discharge, there must be an interface gas-solid dielectric, where the gas is surrounded by the solid. Three 1 mm layers of polycarbonate discs were stuck in a pile, the layer in the middle had 3 mm diameter holes to simulate the cavity. The plastic discs are compressed by the electrodes by tightening bolts. The two electrodes have a different size so the distance surrounding the solid insulator is larger. The smaller electrode is an aluminium disk with 59 mm diameter, and the bigger electrode is a brass disc of 120 mm diameter. To avoid surfaces and/or corona discharges, the set-up is kept inside a container, filled with mineral oil. Figure 62 shows a sketch and a picture of the internal discharge test cell.

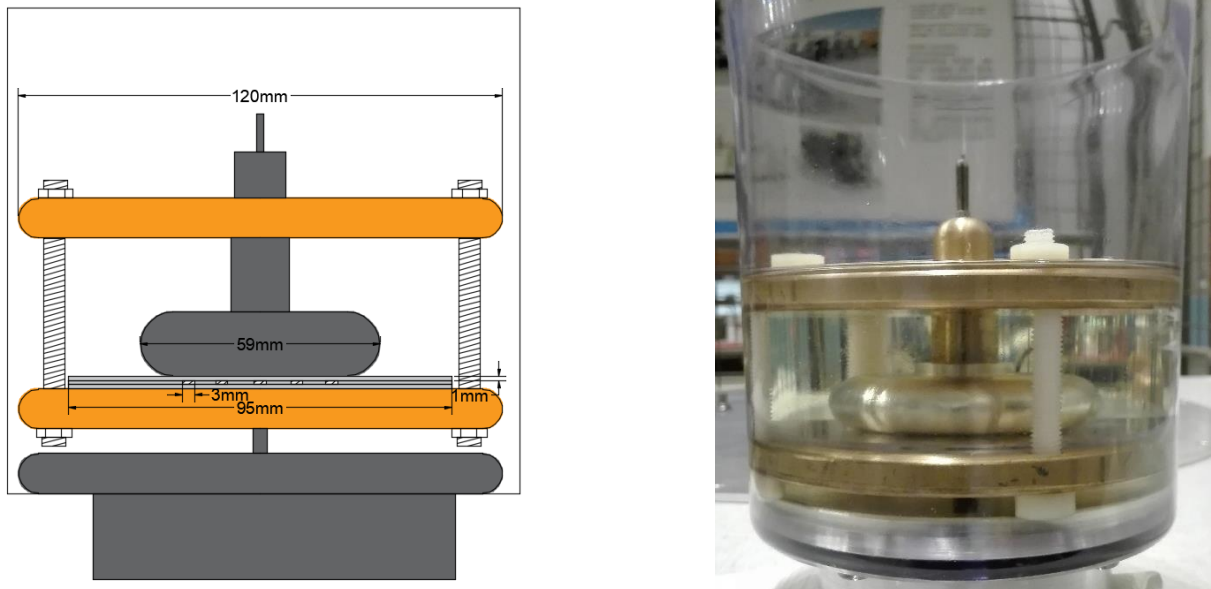


Figure 62. Sketch and photo of the internal discharge test cell (left and right respectively)

The results of the inception PD voltage and average discharge magnitude using the IEC 60270 detection are shown in Table 32.

Voltage [kV]	PD magnitude [pC]
4 kV	150

Table 32. measured internal PD's in the IEC 60270 detection

For the tests in the GIS the following configurations were used:

Voltage source: 4 kV, 50 Hz.

Test-cell: internal discharge

Oscilloscope: (Device 3), 3.125 GS/s, 1000 pulses per channel, 1µs window, 250 MHz filter for CT's, 1.5 GHz filter for Antenna.

CT 1: TS, 3/5 turns HFCT.

CT 2: 3/5 turns HFCT.

CT 8: 3/5 turns HFCT.

A2: Antenna.

A8: Antenna.

Coaxial cable: 50 Ω, RG58, 15 meters.

In this case no filters nor amplifiers were used. The magnitude of the discharges is high enough that the amplifier is not necessary; for the same reason the background noise is very low compared to the signal of interest that the filter is not necessary.

7.4.1. Internal discharge PRPD pattern

In Figure 60 the PRPD pattern is plotted. A comparison between UHFS (first row), 3 turn HFCT (second row) and 5 turn HFCT (third row) is made between in two different locations. The plots show a typical PRPD

pattern for an internal discharge, the discharges are presented from 0° to 90° and from 180° to 270°. The increase of voltage resulted in more discharges distributed in the first and third quarter of sinusoidal wave.

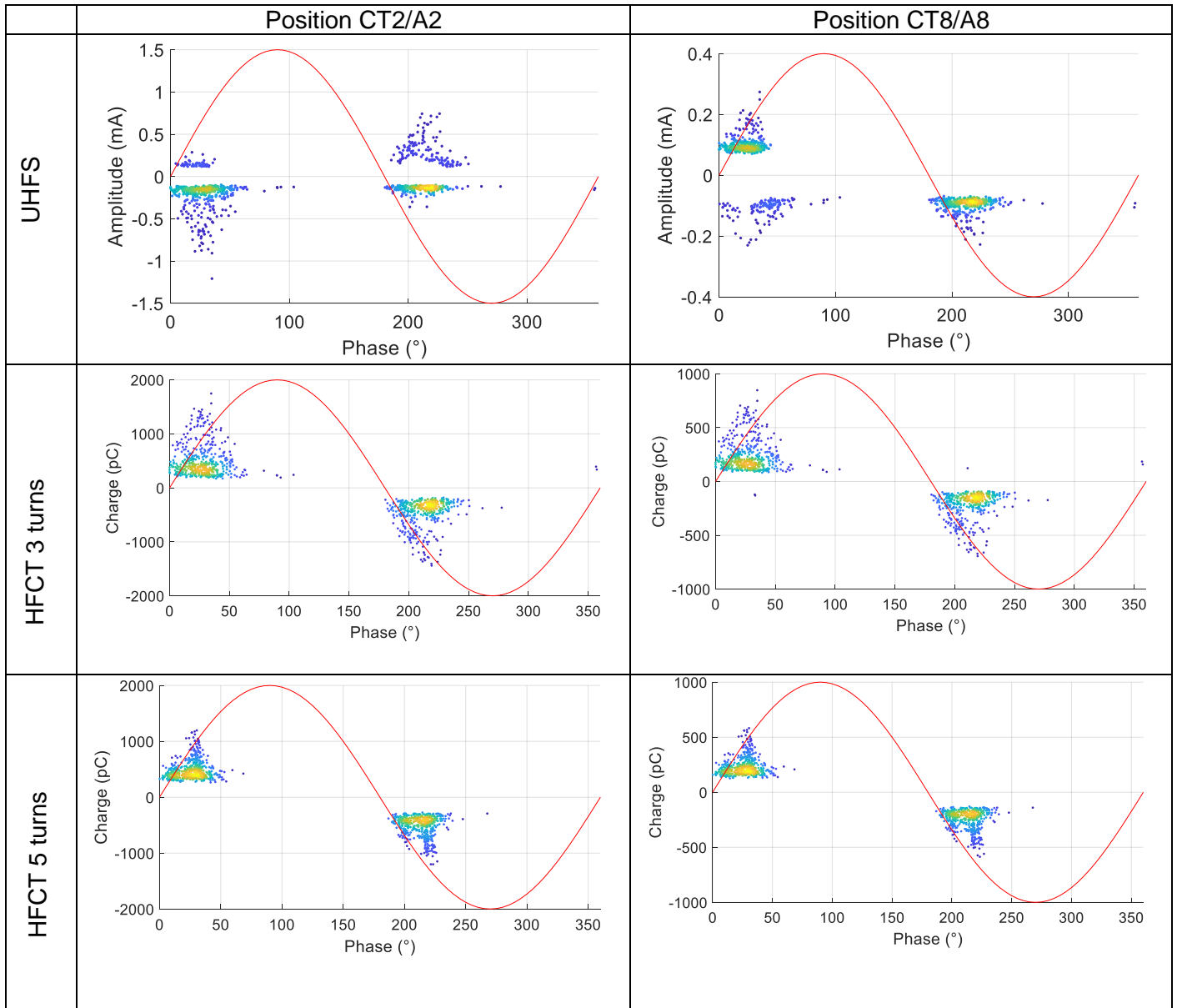


Figure 63. Internal discharge PRPD pattern for HFCT and UHFS in different positions

Following the procedure used to calculate the charge in corona, Table 33 and Table 34 show the results for the “apparent” and “calculated” PD.

Sensor	Apparent PD [pC]	Calculated PD [pC]
CT2	388	291
CT8	185	278

Table 33. Measured charge for an PD in each 3 turn HFCT for internal discharge.

Sensor	Apparent PD [pC]	Calculated PD [pC]
CT2	398	299
CT8	190	285

Table 34. Measured charge for an PD in each 5 turn HFCT for internal discharge.

In this case, it is difficult to compare the results with the IEC 60270 detection method. The values have a lot of variance, and 150pC presented in Table 32 was an average value picked from the quadruple detector.

The measured pulses duration for a 5 and 3 turn CT was 30 ns and 35 ns respectively (using times between zero-crossings).

7.4.2. Internal discharge SNR

The same procedure as in corona is used for internal discharge. In Table 27, the SNR in each sensor is presented. Because of the great magnitude of the discharges, the internal discharge shows higher SNR than the corona discharge. The SNR was lower in magnitude compared to the MPD. It is believed that the internal discharge is slower than the MP, the cavity is not virgin anymore, so a Townsend mechanism takes place. Even though the discharge magnitude was greater, the duration was higher giving a lower pulse peak.

	MPD SNR [dB]
A2	8.95
CT2-3 turns	30.1
CT2-5 turns	27.00
A8	4.56
CT8-3 turns	32.5
CT8-5 turns	29.10

Table 35. SNR for MPD

7.5. Chapter Conclusion

The sensitivity of the sensors depends on the PD magnitude and duration. The UHFS is more benefited with very fast pulses (higher frequencies). On the other hand, for the HFCT, the sensitivity is more exploited if the pulse has a slow duration; more information of the pulse is included in the low frequency. The discharges magnitude and duration depend on the type breakdown mechanism. Therefore, the sensitivity of the sensor will depend on the type of defect.

In all the tested defects, the HFCT showed better results over the UHFS. The HFCT gave higher SNR ratio, better sensitivity and less attenuation. The current transformer also has the advantage of no needing filters and/or amplifiers in some of the tested discharges. Anyhow, it is recommended the use of them to read a higher range of PD. Although the difference between the 5 turn and 3 turn HFCT is not very clear, it is believed that the 5 turn CT has better advantages over 3 turn CT. The 3 turn CT showed better SNR over the 5 turn CT, however, the difference was no very important. The 5 turn CT showed better accuracy in the charge calculation which is one of the essential characteristics of this new sensing method.

Further research can be made by including other important defects in GIS such as surface discharge and floating electrode. During the investigation many attempts were made to reproduce the FED and surface discharge in the GIS. The results were not obtained because the inception voltage was higher enough to risk the security of the GIS (there were sections without SF₆). Another important investigation for the future, is the measurement of PD in GIS under DC voltage.

8. Results and Conclusions

The goal of this research was to find the measuring characteristics of a new method for sensing PDs in a GIS. These characteristics include resolution, attenuation and sensitivity. The most important feature of this new sensing method is the capacity of measuring the PDs magnitude. Therefore, a calibration method for charge calculation is provided. Finally, the HFCT and UHFS are compared with real PD in a GIS.

To provide the calibration method, the electric behavior of the CT and the GIS were calculated. In chapter 3, the transfer function of the sensor was calculated. The calculated gain is compared with measurements, giving similar results for frequencies below 10 MHz. Three CTs with 3, 5 and 10 number of turns were compared, giving different gains and bandwidths. The results showed that the 3 and 5 turns CT are the most suitable. Different pulses with known charges were measured directly with the HFCTs, using a PD calibrator. The calculated charges gave similar results with errors below 12% for both sensors.

In chapter 4, the electrical characteristics of the GIS were calculated considered as a transmission line, due to its big length compared to the pulse wavelength. The phase velocity and characteristic impedance for some sections of the GIS were calculated. This information is important for the charge calculation and the location of the PD source.

Chapter 5 uses the information provided in the previous two chapter to establish an equation to calculate the pulses charge with the HFCT in the GIS. Different situation where studied, such as many conductive bolts in the spacer, just one conductive bolt, and the use of bridges in the spacer. Again, using a calibrator with known injected charges, the calculated discharges measured with the HFCT gave errors below 30% (except near the bushing). Therefore, the charge calculation accuracy is expected to have a tolerance of $\pm 30\%$. With the HFCT is possible to calculate the PD location with a minimum of 2 sensors.

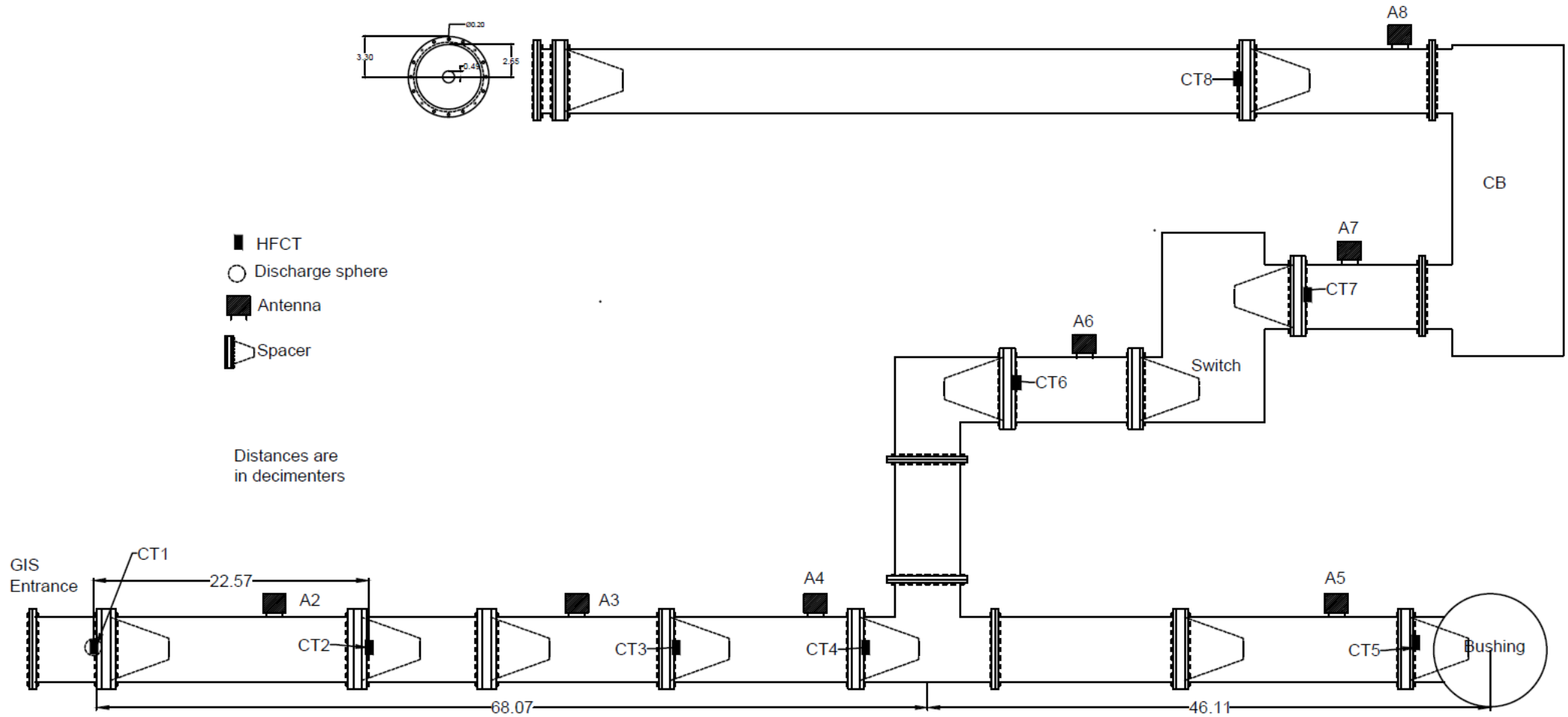
According to the results presented in chapter 6, the HFCT shows a lower attenuation than the antennas. The HFCT measuring method shows attenuation in two situations; when the GIS has an intersection of many electric paths (T section), and when the conduction path has an increase of characteristic impedande (bushings and open switches/CB). On the other hand, the UHFS have attenuation in every section of the GIS; pipe long distances, spacers, T sections, L sections, switches, CB.

In chapter 7, measurements of PD in real defects were performed. Measurements in the HFCT showed better results over the UHFS. The HFCT gave higher SNR ratio, better sensitivity and less attenuation. The discharge calculation using the HFCT method gave approximated values compared with the IEC 60270 detection method. Therefore, it is believed that the measuring method presented in this thesis is capable enough to measure a PD charge magnitude in an acceptable tolerance.

Detection of PDs in GIS has been used since some years already. This gives the advantage to evaluate an electric power device. One important way to know the severity of the PD is by its magnitude. It has been demonstrated that the method presented in this thesis can measure the discharge magnitude. Consequently, giving more precise information of the assessed equipment. The use antennas require high resolution equipment to measure the high frequencies of the discharges. Due to the high attenuation, many antennas must be placed in a GIS, increasing the cost of the measuring system. For an existing GIS, the installation of a UHFS requires a de-energization of the system and dismantling of the GIS. It is concluded that HFCTs for measuring PD in GIS has lower cost compared to the traditional method and gives the advantage of higher resolution, sensitivity, lower attenuation and the ability of measuring PD magnitude.

9. Appendix

9.1. TUDelft GIS sketch



9.2. Devices Index

Device 1. Spectrum Analyzer, Rohde & Schwarz



Spectrum analyser
Rohde & Schwarz
ZVB
BW: 300 kHz-4 GHz

Device 2. Function Generator, Keysight 33500B



Function Generator
Keysight
33500B Trueform
BW: 20 Hz-30 MHz
Amplitude: 1 mV-10 V

Device 3. Oscilloscope, Tektronix MSO58



Oscilloscope
Tektronix
MSO58

Band Width: 2 GHz
Sample Rate: 6.25 GS/s
8 Channels

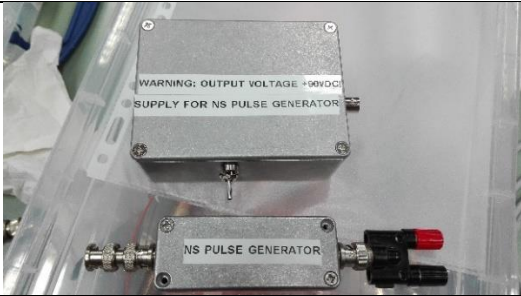
Device 4. Pulse Generator, Phillips PM5712




Pulse Generator
Phillips
PM5712

Band Width: 50 MHz
Rise and fall time: 4ns

Device 5. Pulse Generator, generic

	<p>Pulse Generator Generic</p> <p>1.8 V peak pulse Rise and fall time: 1 ns</p>
---	---

Device 6. PD Calibrator, LDC-5/UHF

	<p>PD Calibrator LDC-5/UHF</p> <p>2-2000pC Rise time: 10ns</p>
---	--

9.3. List of Figures

Figure 1. TUDelft GIS; 1: bushing, 2:CB, 3: switch, 4:spacer, 5:enclosure 7

Figure 2.TenneT / HelWin alpha Offshore HVDC substation (picture taken from [3]. 8

Figure 3. Spacer and flanges joined with bolts. 9

Figure 4. Photo of an installed HFCT in the GIS 9

Figure 5. Defects in a GIS; 1) cavity, 2) surface particle, 3) protrusion in the HV electrode, 4) floating electrode. 13

Figure 6. PRPD for different type of defects: a) internal discharge, b) surface discharge, c) corona discharge, d) FED, e) MPD 14

Figure 7. Current wave for a corona discharge with different radii of the protrusion point..... 15

Figure 8. Diagram of a IEC 60270 detection 15

Figure 9. Representation of the EM wave propagation in the GIS with different sensing systems 16

Figure 10. Time and frequency domain of a Dirac delta function, image taken from [13]..... 17

Figure 11. 10ns pulse duration in time and frequency domain 18

Figure 12. 100ns pulse duration in time domain..... 18

Figure 13. Picture of the HFCT 19

Figure 14. Electric circuit of the HFCT 19

Figure 15. N30 permeability temperature dependent 20

Figure 16. N30 permeability Magnetic field dependent 20

Figure 17. Induced current density in the enclosure due to the power frequency current. 22

Figure 18. Voltage output (a. time domain b. frequency domain) of the HFCT for a 50 Hz 3 Amps input. ... 22

Figure 19. N30 permeability frequency dependent..... 23

Figure 20. 5 turns (left) and 3 turns HFCTs comparison between measured and calculated gain 24

Figure 21. 100 ns pulse output in a 3 turns CT 25

Figure 22. Measurement of a pulse in the GIS (left), frequency spectrum of the pulse (right). 25

Figure 23. Signal processed of a measurement of a pulse in the GIS (left), frequency spectrum of the pulse (right). 26

Figure 24. Pulse comparison using a constant gain in the time domain (left), and frequency domain (right). 27

Figure 25. 4pC pulse in a HFCT and 50Ohms circuit	28
Figure 26. 3 turns (left) and 5 turn (right) HFCT primary reflected impedance.....	29
Figure 27. Setup for measuring the reflected impedance of the HFCT	30
Figure 28. GIS layout with location of UHFS (A#) and HFCT (CT#)	31
Figure 29. Coaxial structure of the GIS	32
Figure 30. Setup for GIS parameters determination.....	32
Figure 31. Pulse measurement to find the Z0 of the enclosure and spacer speed propagation, red circle: incident pulse, green circle: GIS entrance reflection, yellow circle: T junction reflection	33
Figure 32. Measured pulses at different sections	33
Figure 33. Difficulty of spacer capacitance due to it's geometry	35
Figure 34. Reflections measured (left) and simulated (right) in CT1	35
Figure 35. Parasitic capacitance in the bolt path	37
Figure 36. Equivalent electric circuit of the bolts and inner conductor	38
Figure 37. Traveling wave through the bolt with CT	40
Figure 38. Incident and refracted pulses in the time (left) and frequency (right) domain.....	41
Figure 39. Bridge between to flanges.....	41
Figure 40. Representation of the the bridge situated in different positions.	42
Figure 41. Current % in the HFCT bolt for different distances of the bridge.....	42
Figure 42. Measurement setup for current distribution	43
Figure 43. Current density distribution along the propagation axis (z)	44
Figure 44. Current distribution at 5 cm from the discharge	45
Figure 45. Ground loop from with the grounding of the HFCT (left) and solution for ground loop	45
Figure 46. Pulse measured to calculate the charge of 40pC from calibrator.....	47
Figure 47. Measurements to detect defect location.....	49
Figure 48. PD location between two CT's	49
Figure 49. Importance of PD location for magnitude calculation.....	50
Figure 50. Frequency attenuation of a spacer (left) and T and L section (right).....	52
Figure 51. Setup drawing for the creation and measurement of PD	55
Figure 52. Installation of the test cell in the GIS	56
Figure 53. Sawtooth wave generated by the SU	57
Figure 54. Sketch and photo of the corona test cell (left and right respectively)	58
Figure 55. Corona PRPD pattern for HFCT and UHFS in different positions.....	60
Figure 56. Correct (left) and incorrect (right) pulse discrimination for corona discharge in a 3 turns HFCT .	61
Figure 57. CT2 with amplifier (left) and CT4 with high pass filter (right) comparison.	62
Figure 58. CT2 with amplifier and filter (left) and CT4 with filter (right) comparison.....	62
Figure 59. Sketch and photo of the moving paticle test cell (left and right respectively)	63
Figure 60. MPD PRPD pattern for HFCT and UHFS in different positions	64
Figure 61. Pulse discrimination in MPD	65
Figure 62. Sketch and photo of the internal discharge test cell (left and right respectively)	66
Figure 63. Internal discharge PRPD pattern for HFCT and UHFS in different positions	67

9.4. List of tables

Table 1. Characteristic of each PD detection method.	8
Table 2. Saturation current and Charge for different pulses	22
Table 3. Error for different CT's and pulse durations	26
Table 4. Measured charges using a 5 turns CT	28
Table 5. Measured charges using a 3 turns CT	28
Table 6. Reflected impedance for a 3 and 5 turns HFCT for 1 and 10 MHz	30
Table 7. HFCT characteristics summary	30
Table 8. Speed calculation for wave propagation in the GIS	34
Table 9. Calculation of Z0 with measurements	34
Table 10. Time delay and impedance comparison between measurements and Simulink	35
Table 11. Summary of the characteristics of thee GIS	36
Table 12. Results of current ratio for different CT's and different frequencies	39

Table 13. Measured and calculated current percentage for different bridge distances with a 5 turns HFCT	42
Table 14. Measured and calculated current percentage for different bridge distances with a 3 turns HFCT	42
Table 15. Current distribution for a top and bottom discharge for 7 cm and 202 cm distance from the source to the sensor.	44
Table 16. Different reflection factors applied in the charge calculations.	47
Table 17. Calculated charge compared with a calibrator with a 5turns CT	47
Table 18. Calculated charge compared with a calibrator with a 3turns CT	48
Table 19. Sensitivity comparison between the UHFS and the HFCT.....	51
Table 20. Attenuation comparison in 2 spacers and 2.5m distance.....	52
Table 21. Attenuation comparison in 2 spacers, 1 T division and a bushing at 4.4m distance.....	52
Table 22. Attenuation comparison in 2 spacers, 1 T division, 1 L section at 4.3m distance.....	53
Table 23. Attenuation comparison in 2 spacers, 1 switch at 2.2 m distance.....	53
Table 24. measured PD's in the IEC 60270 detection	58
Table 25. Measured charge for an PD in each 3 turns HFCT.....	60
Table 26. Measured charge for an PD in each 5 turns HFCT.....	60
Table 27. SNR for positive and negative corona	61
Table 28. measured moving particle PD's in the IEC 60270 detection	63
Table 29. Measured charge for an PD in each 3 turn HFCT for MPD.....	64
Table 30. Measured charge for an PD in each 5 turn HFCT for MPD.....	65
Table 31. SNR for MPD	65
Table 32. measured internal PD's in the IEC 60270 detection	66
Table 33. Measured charge for an PD in each 3 turn HFCT for internal discharge.....	67
Table 34. Measured charge for an PD in each 5 turn HFCT for internal discharge.....	67
Table 35. SNR for MPD	68

Bibliography

- [1] J. Han, *Breaksown Voltage of Compressed Sulfur Hexafluoride (SF6)*, Arizona, 2010.
- [2] IEEE Power Engineering Society, IEEE Std. C37.122-1993 Standard for Gas-Insulated Substations, New York: IEEE, 1994.
- [3] ASDReports, "The Gas Insulated Substation Market Forecast 2018-1028," ASDReportes, Amsterdam, 2018.
- [4] Foundation Offshore Wind Energy, "Foundation Offshore Wind Energy," [Online]. Available: <https://www.offshore-stiftung.de/en/PROMOTioN>. [Accessed 06 June 2018].
- [5] D. Dangdang, W. Xianpei, Z. Yu, Z. Ying and Z. Jun, "GIS Insulation Fault Diagnosis based on Detection of SF6 decomposition Products," in *9th International Conference on Measuring Technology and Mechatronics Automation*, Changsha, 2017.
- [6] V. Aaradhi y K. Gaidhani, «Partial discharge in Gas Insulated Substations (GIS): A Development and Enginnering Perspective,» de *Environment and Electrical Engineering (EEEIC), 2013 12th International Conference on*, Wroclaw, 2013.
- [7] S. Meijer, *Partial Discharge Diagnosis of High-Voltage Gas-Insulated Systems*, Delft, 2001.
- [8] F. Kreuger, *Industrual High Voltage*, Delft: Delft University Press, 1992.
- [9] R. Piccin, A. Rodrigo, M. Peter, J. Smit y A. Girodet, «Partial discharge analysis of gas insulated systems at high voltage AC and DC,» *IEEE Transactions on Dielectrics and Electrical Insulation*, vol. 22, nº 1, pp. 218-228, 2015.
- [10] J. Calvert, "University of Denver," 2001 July 2001. [Online]. Available: <https://mysite.du.edu/~etuttle/electron/elect6.htm>. [Accessed 10 November 2017].
- [11] C. Zachariades and S. Roger, "Optimization of a High Frequency Current Transformer sensor for Partial Discharge Detection using Finite Element Analysis," *IEEE Sensors Journal*, vol. 16, no. 20, pp. 7526-7533, 2016.
- [12] Epcos, "Ferrites and Accessories," 2013. [Online]. Available: <https://en.tdk.eu/tdken/529420/products/product-catalog/ferrites-and-accessories/epcos-ferrites-and-accessories/e-elp-cores-and-accessories>. [Accessed 20 October 2017].
- [13] A. Rodrigo, M. Peter and J. Smit, "Comparison of Charge Estimation Methos in Partial Discharge Cable Measurements," *IEEE Transactions on Dielectrics and Electrical Insulation*, vol. 22, no. 2, pp. 657-664, 2015.
- [14] Ghandakly, C. Adel y Richard, «A model to predict current distributions in heavy current parallel conductor configurations,» de *Industry Applications Society Annual Meeting, 1991*, Dearborn, 1991.
- [15] S.-Y. Lee, "A Cable Configuration Technique for the Balance of Current Distribution in Parallel cables," *Journal of Marine Science and Technology*, vol. 18, no. 2, pp. 290-297, 2010.
- [16] L. Sluis, *Transients in Power Systems*, West Sussex: John Wiley & Sons Ltd, 2001.
- [17] GUJARAT ENERGY TRANSMISSION Corporation LTD, Technical Specification for Gas Insulated Switchgear, Gujarat: GETCO, 13.
- [18] IEEE, *IEEE Recommended Practice for Powering and Grounding Electronic Equipment*, New York: IEEE, 2005.
- [19] H. Imagawa, K. Emoto y H. Murase, «PD Signal Propagation Characteristics in GIS and Its Location System by Frequency Components Comparison,» *IEEE TRANSACTIONS ON POWER DELIVERY*, vol. 16, nº 4, pp. 564-570, 2001.
- [20] A. Rodrigo, L. C. Castro, D. A. Harmsen and F. Muños, "A new design of a test platform for testing multiple partial discharge sources," *International Journal of Electrical Power & Energy Systems*, pp. 374-384, 2017.
- [21] J. Grainger and W. Severson, *Power System Analysis*, Mc Graw Hill, 1994.
- [22] W. Hayt, J. Kemmerly and S. Durbin, *Análisis de circuitos en ingeniería*, Mexico: McGraw-Hill, 2003.
- [23] S. Orfanidis, *Electromagnetic Waves and Antennas*, New Jersey: Rutgers University, 2016.

